

# **Evaluation of Groundwater Depletion Scenario and its Impacts in NW India by Geodetic Techniques & Modelling Approaches**

(Thesis submitted to the Andhra University, Visakhapatnam in partial fulfilment of the requirement for the award of *Master of Technology in Remote Sensing and GIS*)



**Submitted By:**

**Hemanti Sharma**

**Supervised By:**

**Dr. R. S. Chatterjee, Scientist 'SF', GSGHD  
Mr. Suresh Kannaujiya, Scientist 'SC', GSGHD**



**Indian Institute of Remote Sensing, ISRO,  
Dept. of Space, Govt. of India Dehradun – 248001  
Uttarakhand, India**

**June, 2014**

# **Evaluation of Groundwater Depletion Scenario and its Impacts in NW India by Geodetic Techniques & Modelling Approaches**

(Thesis submitted to the Andhra University, Visakhapatnam in partial fulfilment of the requirement for the award of *Master of Technology in Remote Sensing and GIS*)



**Submitted By:**

**Hemanti Sharma**

**Supervised By:**

**Dr. R. S. Chatterjee, Scientist 'SF', GSGHD  
Mr. Suresh Kannaujiya, Scientist 'SC', GSGHD**



**Indian Institute of Remote Sensing, ISRO,  
Dept. of Space, Govt. of India Dehradun – 248001  
Uttarakhand, India**

**June, 201**

## **DISCLAIMER**

This work has been carried out in partial fulfilment of Masters in Technology program in Remote Sensing and Geographic Information System at Indian Institute of Remote Sensing, Dehradun, India. The author is solely responsible for the contents of the thesis.

## **CERTIFICATE**

This is to certify that the project entitled “**Evaluation of Groundwater Depletion Scenario and its Impacts in NW India by Geodetic Techniques & Modelling Approaches**” is a bona fide record of work carried out by **Hemanti Sharma** during 01 Aug 2013 to 14 Aug 2014. The report has been submitted in partial fulfillment of requirement for the award of Master of Technology in Remote Sensing and GIS in Natural Resource Management with specialization in Geosciences, conducted at Indian Institute of Remote Sensing (ISRO), Dehradun from 21 Aug 2012 to 14 Aug 2014. The work has been carried out under the supervision of **Dr. R. S. Chatterjee, Scientist / Engineer ‘SF’**, and **Mr. Suresh Kannaujiya, Scientist / Engineer ‘SC’** Geosciences and Geohazards Department.

No part of this report is to be published without the prior permission/intimation from/to the undersigned.

**Dr. R. S. Chatterjee**  
Scientist ‘SF’, GSGHD  
IIRS, Dehradun

**Mr. Suresh Kannaujiya**  
Scientist ‘SC’, GSHHD  
IIRS, Dehradun

**Dr. S.K. Saha**  
Dean (Academics)  
IIRS, Dehradun

**Dr. P. K. Champati ray**  
Head, GSGHD  
IIRS, Dehradun

**Dr. Y.V.N. Krishna Murthy**  
Director  
IIRS, Dehradun

*Dedicated to my Family*

## ACKNOWLEDGEMENTS

*This research would not be possible without the support of specific people that believed on me and filled me with the burning desire to achieve the goal of the study. I would like to express my gratitude to all those who helped me, directly or indirectly, to complete this thesis. I am heartily thankful to my supervisors, **Dr. R.S Chatterjee** and **Mr. S. Kannaujiya**, whose able guidance, stimulating suggestions and encouragement helped me during the time of research and writing of this thesis.*

*I wish to express deep gratitude to **Dr. P.K. Champati Ray** (Head, GSGHD) for offering me a challenging project like this, reposing confidence that this would be executable by me in the given time frame, and most importantly, backing it up with situational wisdom, professional advice, thoughtful suggestions and mature conduct.*

*My sincere thanks to **Dr. Y.V.N Krishna Murthy**, Director IIRS, for providing an excellent environment of innovation and research at IIRS. My thanks are also due to **Dr. S.K. Saha**, Dean Academics and **Dr. S.P.S. Kushwaha**, Group Director PPEG. A very special thanks to **Mrs. Shefali Agrawal**, Course Director, M.Tech and Head, PRSD for her continuous support, suggestions and thoughtful interventions at all stages of this project.*

*I mention my deep thankfulness to **Ms. Shailja Thapa**, **Mr. Ashish Dhiman**, **Ms. Sushma Bhandari** and **Shashi Gaurav** for the selfless interest shown and patient support during this research work.*

*I also wish to express my gratitude to the officials and other staff members of Indian Institute of Remote Sensing, who rendered their help during the period of my project work*

Hemanti Sharma

M.Tech 2012-14

Date:

## ABSTRACT

Many parts of the world are suffering from ground water depletion and the problems associated with it. The major problem being land subsidence. Land subsidence is caused due to the compaction of underlying aquifer system complex due to loss of pore pressure by over-pumping of groundwater. The serious problems of land subsidence have been reported in many prominent cities including Kolkata, Bangkok, Shanghai, Tokyo, Mexico City etc. In this study the regional picture of groundwater scenario was obtained by using RL05 land data product obtained from Gravity Recovery and Climate Experiment (GRACE) satellite. The data product was used for North West India covering the states of Rajasthan, Punjab, Haryana, Delhi and Uttar Pradesh over the area of 734646.98 km<sup>2</sup> for the time period from January, 2003 to December, 2012. . To extract the ground water component, the simulated total soil moisture up to 2 m depth, derived from LSM (GLDAS) was subtracted from TWS (equivalent water thickness) revealing volumetric groundwater loss of 104.65 km<sup>3</sup> over 10 years. The maximum ground water loss rate was observed in Haryana & Delhi i.e., 2.29±0.72 cm/year followed by Uttar Pradesh having depletion rate of 1.641±0.77 cm/year. Considering the current scenario, Delhi NCT was selected for the detailed study of the major impact of groundwater depletion i.e. land subsidence, by using Differential Interferometric SAR (DInSAR) technique. For the study ALOS PALSAR (L-Band, FBS Mode, Level 1.1, ascending) and RADARSAT-2 (C-Band, ascending) datasets were used. The temporal baseline of the interferometric pairs ranged from 48 days to 414 days. SRTM (Shuttle Radar Topographic Mission) DEM having 90 m spatial resolution was used to prepare the simulated interferogram. The LOS displacement was calculated using the absolute phase component and time-weighted and coherence weighted LOS displacement rates were calculated for each fringe location. The results came out to be very prominent showing the deformation fringes in same areas for both ALOS PALSAR and RADARSAT-2 datasets extending from December, 2009 to March, 2014. The area in which fringes were observed was in highly developing locality of Dwarka (South-West Delhi) showing the displacement rate of 3.95 cm/year to 8.5 cm/year for 2009-2011 and 3.76 cm/year to 9.25 cm/year for 2013-2014 and the other one was found in Udyog Vihar locality of Gurgaon-Delhi border showing the displacement rate of 3.76 cm/year to 9.25 cm/year for 2009-2011 and 3.44 cm/year to 7.09cm/year for 2013-2014. The study would include higher accuracy if coupled with the ground based measurements of aquifer layer compaction.

Keywords: GRACE, GLDAS, LSM, DInSAR, ALOS PALSAR, RADARSAT-2, SRTM

# TABLE OF CONTENTS

<b>List of Figures .....</b>	<b>V</b>
<b>List of Tables.....</b>	<b>VII</b>
<b>1. Introduction.....</b>	<b>1</b>
1.1. BACKGROUND .....	1
1.2. MOTIVATION & PROBLEM STATEMENT .....	2
1.3. AIMS & OBJECTIVES .....	3
1.4. RESEARCH QUESTIONS .....	4
1.5. THESIS STRUCTURE.....	4
<b>2. Literature Review.....</b>	<b>5</b>
2.1. GRACE.....	5
2.1.1. Terrestrial Water Storage .....	7
2.1.2. Ground Water Storage Change Estimation From Grace Tws.....	8
2.2. DINSAR FOR LAND SUBSIDENCE.....	8
2.2.1. Dinsar Concept.....	9
2.2.2. Basics Of Sar Interferometry .....	10
2.2.3. Interferometric Sar Data Structure .....	14
2.2.4. Interferometric Processing .....	15
2.3. AQUIFER COMPLEX LAYER COMPRESSION AND LAND SUBSIDENCE.....	18
2.3.1. Measurement Of Land Subsidence .....	18
2.3.2. Aquifer System Deformation .....	19
<b>3. Study Area .....</b>	<b>26</b>
3.1. STUDY AREA FOR REGIONAL SURVEY .....	26
3.2. STUDY AREA FOR DETAILED SURVEY.....	28
3.2.1. Demography.....	28
3.2.2. Hydrometeorology .....	28
3.2.3. Physiography.....	28
3.2.4. Geology.....	30
3.2.5. Alluvial Aquifers .....	30
3.2.6. Soil Type.....	30
3.3. GROUND WATER SCENERAIO IN DELHI NCT .....	33
3.3.1. Potential Aquifers .....	33

3.3.2. Major Ground Water Related Problems.....	34
<b>4. Data Used And Methodology.....</b>	<b>35</b>
4.1. OVERVIEW.....	35
4.2. DATA USED .....	35
4.2.1. The Satellite Data Used For Ground Water Storage Change Estimation Are Listed Below .....	35
4.2.2. Data Specifications Used For Dinsar Processing.....	36
4.2.3. Ancillary Data.....	37
4.3. METHODOLGY .....	38
4.3.1. Methodology For Ground Water Storage Change Estimation Using Grace Data .....	38
4.3.2. Methodology To Study Land Subsidence In Delhi Nct Using Differential Interferometric Sar Technque .....	42
<b>5. Results &amp; Discussions.....</b>	<b>49</b>
5.1. GROUND WATER STORAGE CHANGE ESTIMATION FOR NW INDIA USING GRACE DATA.....	49
5.2. LAND SUBSIDENCE STUDY IN DELHI NCT USING DIFFERENTIAL INTERFEROMETRIC SAR TECHNIQUE .....	59
<b>6. Conclusion and Recommendation.....</b>	<b>71</b>
6.1. CONCLUSIONS .....	71
6.1.1. How Far Groundwater Depletion Scenario Is Correlated With Space-Borne Gravity Anomalies? .....	71
6.1.2. What Is The Extent Of Impact Of Groundwater Depletion To Land Subsidence In Delhi Nct?.....	71
6.2. RECOMMENDATIONS .....	72
<b>References .....</b>	<b>73</b>

## LIST OF FIGURES:

<b>Figure 2.1.</b> GRACE twin satellites. Image courtesy of GFZ, Potsdam.....	6
<b>Figure 2.2.</b> Spatial coverage of GRACE ground tracks .....	6
<b>Figure 2.3.</b> GRACE Gravity Model 01 based on 111 days of GRACE data .....	7
<b>Figure 2.4.</b> Geometry of satellite InSAR System.....	10
<b>Figure 2.5.</b> Types of Interferometry Viz., single pass. Single track and repeat pass .....	11
<b>Figure 2.6.</b> Ways to produce a differential Interferogram.....	11
<b>Figure 2.7.</b> Different parameterizations of the InSAR baseline geometry.....	13
<b>Figure 2.8.</b> Interferometric SAR data structure.....	15
<b>Figure 2.9.</b> Image processing steps using DInSAR Technique.....	17
<b>Figure 2.10.</b> Benchmark and extensometer.....	19
<b>Figure 2.11.</b> Before drawdown (left), after drawdown (centre) and after recovery (right)..	19
<b>Figure 2.12.</b> Compaction in a horizontal layer.....	22
<b>Figure 2.13.</b> Idealized stress-strain relation for fine-grained sediments. ....	25
<b>Figure 3.1.</b> Map showing location of study area.....	26
<b>Figure 3.2:</b> Geological map of North-West India.....	27
<b>Figure 3.3:</b> (a) Delhi quartzite; (b) older alluvium of aeolian deposits; (c) younger alluvium of Yamuna flood plain.....	31
<b>Figure 3.4:</b> Land use / land cover map of Delhi NCT.....	32
<b>Figure 3.5:</b> Geological map of Delhi NCT.....	33
<b>Figure 4.1.</b> Flow chart showing the brief methodology for the project. ....	38
<b>Figure 5.1.</b> Terrestrial water storage change rate for the decade 2003-12 for NW India....	49
<b>Figure 5.2.</b> Soil moisture change rate for the decade 2003-12 for NW India. ....	50
<b>Figure 5.3.</b> GWSC rate for the decade 2003-12 for NW India. ....	50
<b>Figure 5.4.</b> GWSC mean for the decade 2003-12 for NW India.....	51
<b>Figure 5.5.</b> Pre-Monsoon decadal GW fluctuation map for 2003-12 for NW India. ....	51
<b>Figure 5.6.</b> Post-Monsoon decadal GW fluctuation map for 2003-12 for NW India.....	52

<b>Figure 5.7.</b> Monsoon decadal GW fluctuation map for 2003-12 for NW India.....	52
<b>Figure 5.8.</b> Pre-Monsoon GW change from decadal (2003-12) mean for NW India.....	53
<b>Figure 5.9.</b> Post-Monsoon GW change from decadal (2003-12) mean for NW India.....	53
<b>Figure 5.10.</b> Decadal time series analysis for Rajasthan.....	54
<b>Figure 5.11.</b> Decadal time series analysis for Uttar Pradesh.....	54
<b>Figure 5.12.</b> Decadal time series analysis for Punjab. ....	55
<b>Figure 5.13.</b> Decadal time series analysis for Haryana and Delhi. ....	55
<b>Figure 5.14.</b> Decadal time series analysis for Delhi pixel.....	56
<b>Figure 5.15.</b> Decadal time series analysis for NW India.....	56
<b>Figure 5.16.</b> Correlation of Pre-Monsoon GW fluctuation derived from GRACE results and Groundwater level data for Delhi pixel for 2003-12.....	57
<b>Figure 5.17.</b> Correlation of Post-Monsoon groundwater fluctuation derived from GRACE results and Groundwater level data for Delhi pixel for 2003-12. ....	57
<b>Figure 5.18.</b> GRACE derived volumetric water loss rate .....	58
<b>Figure 5.19.</b> Interferogram showing land subsidence in Dwarka and Gurgaon area. ....	59
<b>Figure 5.20.</b> Interferogram showing land subsidence in Dwarka and Gurgaon area. Temporal baseline 92 days (2/12/2009 – 03/04/2010) and having average coherence of 0.32.....	60
<b>Figure 5.21.</b> Interferogram showing land subsidence in Dwarka and Gurgaon area. Temporal baseline 414 days (2/12/2009 - 20-01-2011) and having average coherence of 0.22; coherence of 0.35 and 0.36 for fringe areas. ....	61
<b>Figure 5.22.</b> Interferogram showing land subsidence in Dwarka and Gurgaon area. Temporal baseline 368 days (17-01-2010 - 20-01-2011) and having average coherence of 0.66. ....	62
<b>Figure 5.23.</b> Interferogram showing land subsidence in Dwarka and Gurgaon area. Temporal baseline 322 days (4/3/2010 - 20-01-2011) and having average coherence of 0.23; coherence of 0.40 and 0.34 for fringe areas. ....	63
<b>Figure 5.24.</b> Interferogram showing land subsidence in Dwarka and Gurgaon area. Temporal baseline 48 days (03-12-2013 - 20-01-2014) and having average coherence of 0.26; coherence of 0.49 and 0.36 for fringe areas. ....	64
<b>Figure 5.25.</b> Interferogram showing land subsidence in Dwarka and Gurgaon area. Temporal baseline 96 days (03-12-2013 - 09-03-2014) and having average coherence of 0.25; coherence of 0.34 and 0.32 for fringe areas. ....	65

## LIST OF TABLES:

<b>Table 2.1.</b> Microwave bands utilized in Radar with their wavelength.....	10
<b>Table 4.1.</b> Sensor Specifications for SAR Data.....	36
<b>Table 4.2.</b> ALOS PALSAR (L-Band) Data Specifications.....	36
<b>Table 4.3.</b> RADARSAT-2 (C-Band) Data Specifications.....	36
<b>Table 4.4.</b> Specifications of SRTM DEM Version 4.1.....	37
<b>Table 4.5.</b> Specifications of data pairs generated from ALOS PALSAR data.....	42
<b>Table 4.6.</b> Specifications of data pairs generated from ALOS PALSAR data.....	43
<b>Table 5.1.</b> Volumetric Ground Water Loss in NW India for 2003-12.....	58
<b>Table 5.2.</b> LOS Deformation rate for ALOS PALSAR data sets for Delhi from December, 2009 to January, 2011.....	65
<b>Table 5.3.</b> LOS Deformation rate for RADARSAT-2 data sets for Delhi December, 2013 to March, 2014.....	66
<b>Table 5.4.</b> LOS Deformation rate using phase component for ALOS PALSAR data sets for Delhi from December, 2009 to January, 2011.....	69
<b>Table 5.5.</b> LOS Deformation rate using phase component for RADARSAT-2 data sets for Delhi from December, 2013 to March, 2014.....	70

# 1. INTRODUCTION

## 1.1. BACKGROUND:

A major portion of Earth's freshwater is stored in the form of groundwater. In India it plays the role of major source of water for agriculture, industrial as well as domestic purposes. It accounts for nearly 60% of the total irrigation potential in the country (NRSA, 2008). The demand for ground water is increasing due to rapid growth in population, industrial development, urbanization and increase in agricultural activities. As per the Central Ground Water Board, 2008-09 report the Annual Replenishable Ground Water Resource for the entire country is 431 billion cubic meter (bcm), Net Annual Ground Water availability is 396 billion cubic meter whereas the annual ground water draft for irrigation, domestic and Industrial is 243 billion cubic meter and the stage of Ground water Development for the country as a whole is 61% ("Ground Water Resources -WRIS", 2014).

The occurrence and distribution of ground water in the country varies significantly depending on geology, rainfall and geomorphology. In regions like North West India ground water resources are depleting whereas the eastern parts of the country have plenty of ground water resources which remained unexploited. The distribution of rainfall also varies widely both in time and space. Most of rainfall (about 76%) occurs during the Monsoon months resulting into eight comparatively dry months. Similarly, the Meteorological subdivisions like North east India, coastal Karnataka and Goa receives more than 250 cm of rainfall annually while West Rajasthan gets only about 30 cm (IMD 2013).

It is difficult to determine directly the Terrestrial Water Storage on regional scales. Research (Ramillien et al., 2008; Rodell et al., 2007; Schmidt et al., 2006; Werth et al., 2009; Widiastuti, 2009) has shown that GRACE satellite gravimetry offers a very interesting alternative remote sensing technique to measure changes in total water storage (ice, snow, surface waters, soil moisture, groundwater) over continental areas, representing a new source of information for hydrologists and global hydrological modellers. The regional picture ground water level scenario can be optimally observed using the regional scale space borne gravity anomalies obtained by Gravity Recovery and Climate Experiment (GRACE) mission. The GRACE satellite mission, launched by NASA and the German Aerospace Centre (DLR) in 2002, measures temporal variations in the gravity field, which can be used to estimate changes in terrestrial water storage (TWS) (Rodell et al., 2009). Although its spatial resolution (160,000 Km<sup>2</sup>) and temporal resolution (monthly) are low in comparison with other satellites, its major advantage is that it senses water stored in all forms, including groundwater. Groundwater storage changes can be extracted from GRACE data by using auxiliary information regarding the other components of TWS, which may be either in situ observations or land-surface models. Another advantage being its non-limitation to measurement of atmospheric and near-surface phenomena like radars and radiometers (Landerer and Swenson 2012). For the period of August 2002 to October 2008 using terrestrial water storage change observations from GRACE and simulated soil-water variations using a data integrating hydrological modelling approach, the mean ground water depletion rate was estimated as  $4 \pm 1.0$  cm yr<sup>-1</sup> equivalent height of water and  $17.7 \pm 4.5$  km<sup>3</sup> yr<sup>-1</sup> over the north-western Indian states of Rajasthan, Punjab and Haryana (including Delhi) (Rodell et al. 2009).

Unconsolidated sedimentary deposits form one of the most prolific type of aquifers. Many cities located over these aquifers have developed them for all or part of their urban water supply. In at least 17 of these cities, the development of local groundwater, has had an unanticipated impact, land subsidence or gradual lowering of the land surface caused by compaction of aquifer system (Galloway et al. 1998). In at least eight of these areas the economic cost of this type of subsidence has been significant. These cities include Bangkok (Thailand), Houston (USA), Mexico city (Mexico), Osaka (Japan), San Jose (USA), Shanghai (China), Tokyo (Japan) and Venice (Italy) (Holzer and Johnson, 1985). The main problem associated with land subsidence in urban areas is where the compaction that causes subsidence is at shallow depth and where buildings are founded on form materials beneath compacting layers. This may cause ground failure or rupture, consisting of tension cracks in buildings, commonly associated with land subsidence (Kaya et al, 2005).

Amongst various geodetic techniques to measure land subsidence, Differential Interferometry Synthetic Aperture Radar (DInSAR) has been a very important remote sensing tool used for estimation of temporal and spatial surface motions due to subsidence (Berardino et al. 2002). DInSAR has several important advantages over classical methods used to measure subsidence deformation. One of the main advantages of DInSAR is its high spatial coverage in urban areas. If we compare DInSAR with other common techniques, such as Differential Global Positioning System (DGPS) and instrumental methods, the latter can only measure ground deformations at a few discrete points, not over a wide and continuous area. In the case of levelling methods, they can cover a whole territory but the average distance between benchmarks is much higher than DInSAR resolution. It is not economically feasible to repeat complete levelling surveys frequently as the cost of carrying out the measurements of a levelling network comes out to be very high (Tomás et al., 2005).

The land subsidence caused by aquifer layer compression caused due to ground water withdrawal has been observed using DInSAR technique in many parts of the world including Kolkata city, India (Chatterjee et al., 2006), Segura River, SE Spain (Tomás et al., 2005), Antelope Valley, Mojave Desert, California (Galloway et al., 1998), Las Vegas, Nevada, USA (Amelung et al., 1999), New Jersey, USA (Sun, Grandstaff, and Shagam, 1999), Bandung City, Indonesia (Abidin et al., 2009).

## **1.2. MOTIVATION & PROBLEM STATEMENT:**

India is largest user of ground water and irrigates about 39 Million Ha of land through groundwater irrigation followed by China and USA. Rapid development in the water resources sector has been taking place in the country over the last few decades resulting in various undesirable environmental impacts. The sustainability of ground water resources are hampered due to various reasons, concerns about groundwater resources involve questions about depletion of ground water levels, reduction of resources, potential loss of groundwater dependent eco-systems, land subsidence and changes in groundwater quality (CGWB 2012).

Most of the aquifer systems in NW India comprises of alluvium sediments of river basins constituting the unconsolidated sediments. These are by far the most significant groundwater

reservoir for large scale and extensive development (CGWB 2013). Hence, these areas may be prone to land subsidence due to aquifer layer compaction.

Due to exponential increase in the population and hence the excessive stress on the usage of groundwater, this valuable resource is depleting at abnormal rates impacting the environment in multiple ways including water scarcity and hence land subsidence. As the population growth and eventually the water demand is increasing rapidly in North West India resulting in higher groundwater depletion rate coupled with high pressure exerted by the overburden (urban setup). It may lead to subsidence in highly populated urban areas leading to the problems of water logging and increased runoff leading to flooding in certain areas.

Delhi National Capital Territory occupying the area of 1483 sq.km, comes under the most vulnerable areas in NW India as far as ground water depletion is concerned. The population density of Delhi NCT has increased from 9340 persons/sq. Km in 2001 to 11,297 persons/sq. Km in 2011 (Census, 2011). Hence it is the union territory with highest population density. With the drastic increase in urban sprawl in Delhi, the water requirements have also increased exponentially leading to higher rates of ground water depletion in some parts. The major aquifers contributing to the groundwater are fine to medium sand of Older alluvium, medium to coarse sand of Newer alluvium along the Yamuna Flood Plain and the hard rock formations occupied by quartzite, inter-bedded with mica schist belonging to Delhi Super Group (Shekhar et al. 2009). The depth to water in the Delhi state varies greatly from 1.2 meter (in the Yamuna flood plain) to more than 64 meters (in the southern part of the Delhi Ridge) below ground level. The groundwater is declining in majority of the areas of Delhi on account of overexploitation of the resources. The rate of decline is as high as 1.7 to 2 meters/year in some areas (South & South west Dist.). Thus seven out of nine districts of Delhi are categorized as overexploited with respect to dynamic groundwater resources. The groundwater quality shows horizontal and vertical variation in space. The deeper aquifers are mostly underlain by saline water in alluvial areas (R. Chatterjee et al. 2009). Hence the detailed study of land subsidence associated with withdrawal of ground water in Delhi NCT and surrounding areas is the need of the hour.

### **1.3. AIMS & OBJECTIVES:**

The prime focus of the study is to correlate groundwater depletion and resulting land subsidence on local scale by using geodetic techniques and modelling approaches.

1. To study groundwater depletion and recharge scenario using terrestrial water storage change observations from GRACE and simulated soil-water variations.
2. To study the impacts of groundwater depletion in the study area with emphasis on land subsidence in Delhi NCT using geodetic techniques like DInSAR and GPS.

#### **1.4. RESEARCH QUESTIONS:**

1. How far groundwater depletion scenario is correlated with space-borne gravity anomalies?
2. What is the extent of impact of groundwater depletion to land subsidence in Delhi NCT?

#### **1.5. THESIS STRUCTURE:**

The whole thesis is divided into six chapters. The first chapter provides general introduction about the research work including problem statement, research objectives and questions. The second chapter deals with literature review in which the related works with respect to the research work are presented. In the third chapter information about the chosen study area is given. The fourth chapter gives description about the methodology and the materials/data used. Fifth chapter presents the findings of this research work and a detailed discussion on the results obtained. In the sixth chapter a conclusion is drawn based on the results obtained along with some recommendations.

## 2. LITERATURE REVIEW

### 2.1. GRACE:

The data in this study is gathered from the Gravity Recovery and Climate Experiment (GRACE) twin satellites, launched in 2002 (“GRACE - Gravity Recovery and Climate Experiment”, 2013). The satellites are the first of their kind, although after realizing their success and wide array of applications, more missions have been planned. The satellites track the gravity pull from any given point on the Earth surface very accurately by measuring the distance between them as they pass areas with greater or lesser gravitational pull by using various high-precision instruments. This change in separation distance can be used to calculate the gravitational pull of that area. They orbit the earth at about 450-500 km with an inclination of 89.5°. This segment of space is called the low orbit (Schmidt et al., 2008). By lowering the orbit, it is possible to increase the resolution of the measurements. Closer to the atmosphere, there is; however, more particles creating drag forces and wear on the satellites (Hernquist and Weinberg, 1989). The GRACE mission planned lifetime was originally planned through 2007 (Wiese et al., 2009). This has been extended, and the mission is now expected to provide data until the successor GRACE Follow-On (FO) is scheduled for launch in 2016. Figure 2.1 on page 5 shows an illustration of the twin satellites. The distance between them is about 220 km.

Although primarily aimed at accurately mapping time variations in Earth’s gravity field at 30 day intervals, GRACE has shown remarkable prospects for inferring water mass changes over the globe (Tapley et al., 2004). Based on satellite observations of Earth’s time variable gravity field from the Gravity Recovery and Climate Experiment (GRACE), it is possible to derive variations in terrestrial water storage (Syed et al. 2008).

The GRACE mission uses the concept of satellite-to-satellite tracking in the low-low mode to measure any variations in intensity of the earth’s gravity field by two geometrically identical orbiting satellites spaced about 200 kilometres apart and equipped to measure their relative velocity. The basic idea is to trace the spatio-temporal gravity field with an increased sensitivity by means of micrometer-precise inter-satellite range and range-rate observations of two co-planar orbiting satellites. As the two satellites move along their orbit, separated by a mean inter-satellite distance of approximately 220 km, the relative motion of the spacecraft, visible as continuous variations in the measured range and range-rate, respectively, is proportional to the integrated differences of the gravity accelerations felt by each satellite at its individual position (Schmidt et al., 2008).

Some basic characteristics are given below:

- The mission was launched on 17 March 2002 and it has recently been agreed to extend the experiment to the end of its on-orbit life, which is expected in 2015 (“Grace - Earth Missions - NASA Jet Propulsion Laboratory - NASA Jet Propulsion Laboratory”, 2013).
- The system’s initial altitude was 500 km (the orbit altitude is not kept fixed and decreases due to air drag with an average rate of about 2.7 km/year). This low

altitude was selected to allow for a detection of the gravity signals in the inter-satellite data well above the micron level (Wolff 1969).

- To yield a global coverage, an almost polar inclination has been selected of  $89.5^\circ$ .
- Absolute positioning of the two spacecraft and the inter-satellite observations, is provided by a space-proved multi-channel, two-frequency GPS receiver onboard each GRACE satellite, known as GPS-SST (satellite to satellite).
- K-band range and range-rate satellite-to-satellite tracking between the two GRACE satellites, known as KBR-SST (satellite to satellite).

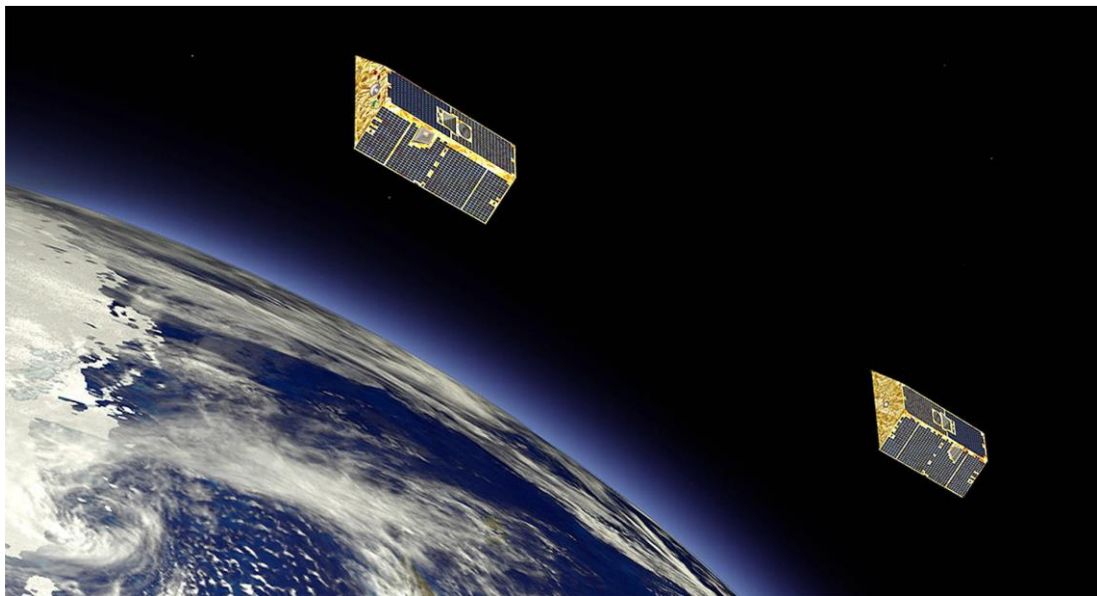


**Figure 2.1.** GRACE twin satellites. Image courtesy of GFZ, Potsdam

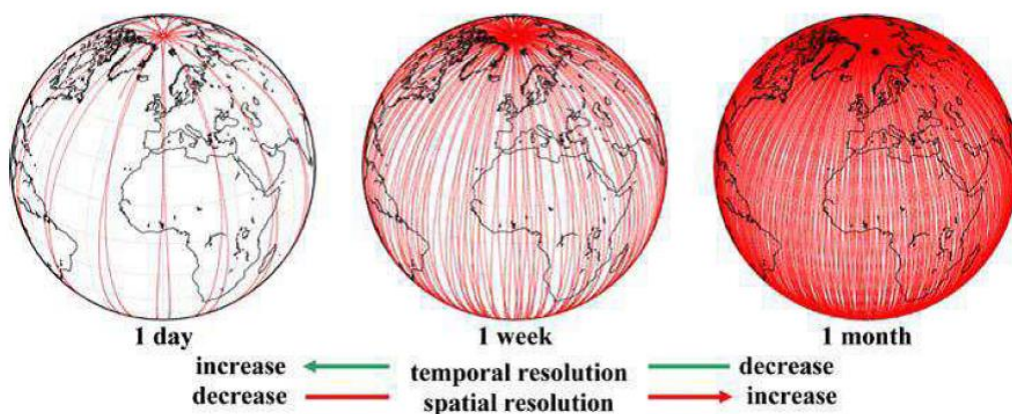


**Figure 2.2.** Spatial coverage of GRACE ground tracks, indicating the trade-off between spatial and temporal resolution (Schmidt et al., 2008)

Monthly gravity field estimates made by the twin Gravity Recovery and Climate Experiment (GRACE) satellites have a geoid height accuracy of 2-3 millimeters at a spatial resolution as small as 400 kilometers. The trade-off between spatial and temporal resolutions illustrated in Figure 2.2.

Observations of seasonal variations in Earth's gravity field place important constraints on models of global mass variability and temporal exchange among the land, ocean, and atmosphere. This is particularly important for subsystems that might otherwise be extremely difficult to detect and monitor. Terrestrial water variations are the largest omitted phenomena and are thus the dominant unmodeled signal that should be evident in the monthly gravity estimates (Tapley et al., 2004).

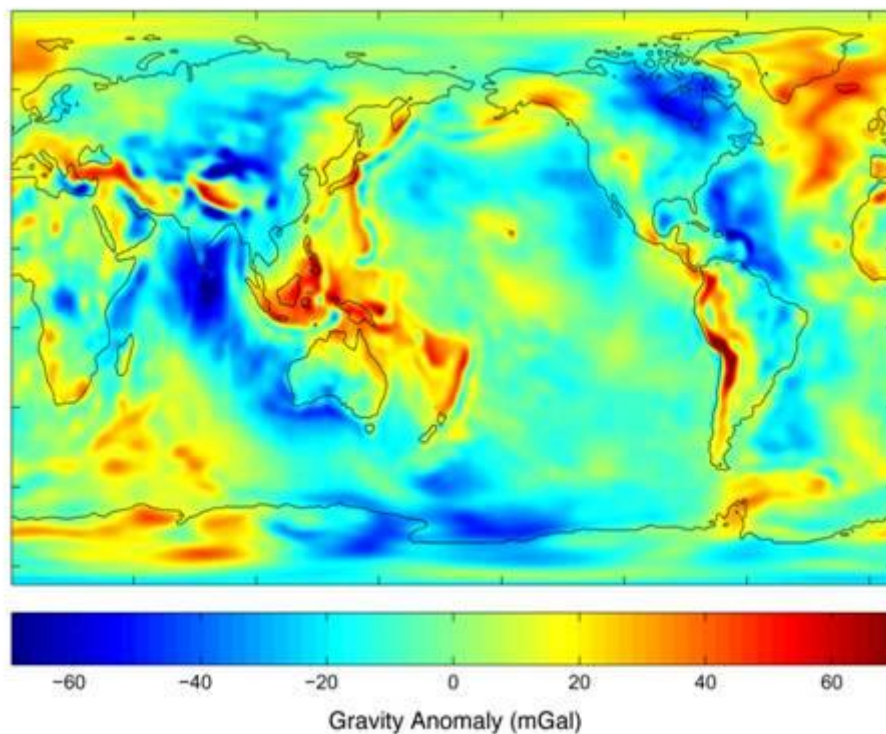


**Figure 2.3.** *GRACE Gravity Model 01 based on 111 days of GRACE data*

### **2.1.1. TERRESTRIAL WATER STORAGE:**

Terrestrial water storage (TWS) can be defined as all forms of water stored above and underneath the surface of the Earth (Syed et al., 2008), which can include water in vegetation surfaces, snow, ice, soil water, groundwater, surface water in rivers, lakes, wetlands and man-made reservoirs.

For a hydrologist there are two major problems to deal with; firstly to quantify the amount of water in the different hydrological cycle phases and seasonally to evaluate the rate of transfer of water between the cycle phases (Syed et al., 2008). Individual soil moisture or groundwater measurements provide only local estimates of water storage. Thus temporal and spatial variations of water storage are presently not known with sufficient accuracy for large areas (Schmidt et al., 2006).

Small variations of gravity anomalies from monthly into a decade time scales are mainly due to redistributions of water masses inside the surface fluid envelopes of our planet (Ramillien et al., 2008). This allows us to derive even tiny variations in TWS (Terrestrial Water Storage) from the satellite observations of the gravity field.

### **2.1.2. GROUND WATER STORAGE CHANGE ESTIMATION FROM GRACE TWS:**

As discussed above, the terrestrial water storage anomaly extracted from GRACE provides us the information about the total amount of water column thickness in and above the Earth's crust. It includes surface water, soil moisture (water in soil upto 2 m depth), groundwater, snow. To extract groundwater anomalies from GRACE derived TWS anomalies, we need to reduce the other quantities from TWS (Faunt et al., 2009).

In our study, we have used level 3 GRACE TWS anomalies which are expressed as thickness of water column in centimetres. The spatial resolution of this data is  $1^0 \times 1^0$ . The data is then rescaled and checked for leakage and measurement errors. As the study area does not have any snow content and due to lack of accurate information about surface water, for our study we have not used these two quantities in the below equation.

Soil moisture is taken from Global Land Data Assimilation System (GLDAS) with same spatial resolution as of GRACE TWS. It is divided into 4 separate layers Viz., 0-10 cm, 10-40 cm, 40-100 cm, 100-200 cm. All the 4 layers are accounted and the soil moisture anomaly is calculated. It is then removed from the TWS and ground water change is obtained.

Groundwater storage change is estimated by using following equation,

$$GW_{\alpha} = TWS_{\alpha, GRACE} - (SW_{\alpha} + SM_{\alpha} + SP_{\alpha}) \quad (2.1)$$

Where:

$GW_{\alpha}$  = groundwater storage anomaly  
 $TWS_{\alpha}$  = total water storage anomaly  
 $SW_{\alpha}$  = surface water storage anomaly  
 $SM_{\alpha}$  = soil moisture storage anomaly  
 $SP_{\alpha}$  = snowpack storage anomaly

### **2.2. DINSAR FOR LAND SUBSIDENCE:**

Various varieties of geophysical investigations directed toward studying subsurface processes use observations made on or very near to the Earth's surface. One of the directly observable quantities containing information on subsurface processes is the displacement of the Earth's surface i.e., land subsidence. Accurate dense spatial and temporal sampling to enable meaningful conclusions regarding the processes of interest at depth has been extremely difficult with the available geodetic techniques i.e., global positioning systems, ground levelling, etc.

This has changed dramatically with the development of Differential Interferometry Synthetic aperture Radar. Where applicable, DInSAR techniques allow the measurement of one component of the surface displacement field at spatial resolutions on the order of meters or tens of meters with a precision on the order of millimeters to centimeters over large areas of up to thousands of square kilometers (Gabriel et al., 1989). The basic principles and the limitations of synthetic aperture radar (SAR) interferometry are presented in this chapter.

### **2.2.1. DINSAR CONCEPT:**

Synthetic Aperture Radar Interferometry (InSAR) is a tool for measuring topography of the terrain, surface change and surface deformation from the interference of two or more SAR acquisitions over the same area, with slightly different look angles. Differential-InSAR is an application of InSAR used to measure the slight change in the relative position of the point scatterer in time interval between two SAR observations (ex. Land subsidence, earthquake, landslide, etc.). ‘Differential interferometry’ is the commonly used term for the production of interferograms from which the topographic contribution has been removed. The geometry of satellite InSAR system is shown in fig. 2.4.

SAR data pairs with good coherence are required for informative interferogram generation. DInSAR can be implemented in order to map deformation and its displacement rate in less vegetated area. InSAR generated displacement map can be interpreted with the help of aerial photographs and high resolution optical satellite imagery. Theoretically, two interferogram made from four images are sufficient to map a velocity field by differential processing. Interferogram spanning different periods help to detect temporal variability (Gehlot and Hanssen, 2008).

Due to side looking geometry of radar, three or more SAR images are sufficient to generate differential interferogram or any of the interferogram can be simulated via registering a DEM (e.g. SRTM DEM) with respect to the to the geometry of the SAR image pair. Hence, quality of DEM influences the result (Massonnet et al., 1993).

The major steps in DInSAR data processing are as follows:

1. Input of master and slave images,
2. Subtraction of the flat-Earth effect and phase unwrapping.

In general, according to the number of images used in DInSAR data processing, there are three methods for subtracting topography-dependent phases. The first method is to obtain deformation phases directly from the image pair with a zero baseline. Second is to simulate topographic phases with an external digital elevation model (DEM) and then subtracts it from the interferogram.

The above mentioned methods use only two In-SAR images but it is usually difficult to find a zero-baseline image pair and a good external DEM. The third method obtains topographic phases from a pair of In-SAR images with a long spatial but short temporal baseline. Then it measures the deformation from another interferogram by subtracting the unwrapped topographic phases. In contrast to above mentioned methods, this method requires three or

four interferogram but phase unwrapping has to be carried out in every method. The DInSAR technique shows great potential for the monitoring of ground deformation (Ding et al. 2004).

All of the imaging radar data used for this dissertation was acquired by the ALOS PALSAR (L-Band) and RADARSAT-2 (C-Band) satellites.

**Table 2.1.** Microwave bands utilized in Radar with their wavelength.

Band	Ka	K	Ku	X	C	L	P
Wavelength in centimetre	0.75-1.10	1.10-1.67	1.67-2.40	2.40-3.75	3.75-7.50	7.50-15.0	15-30

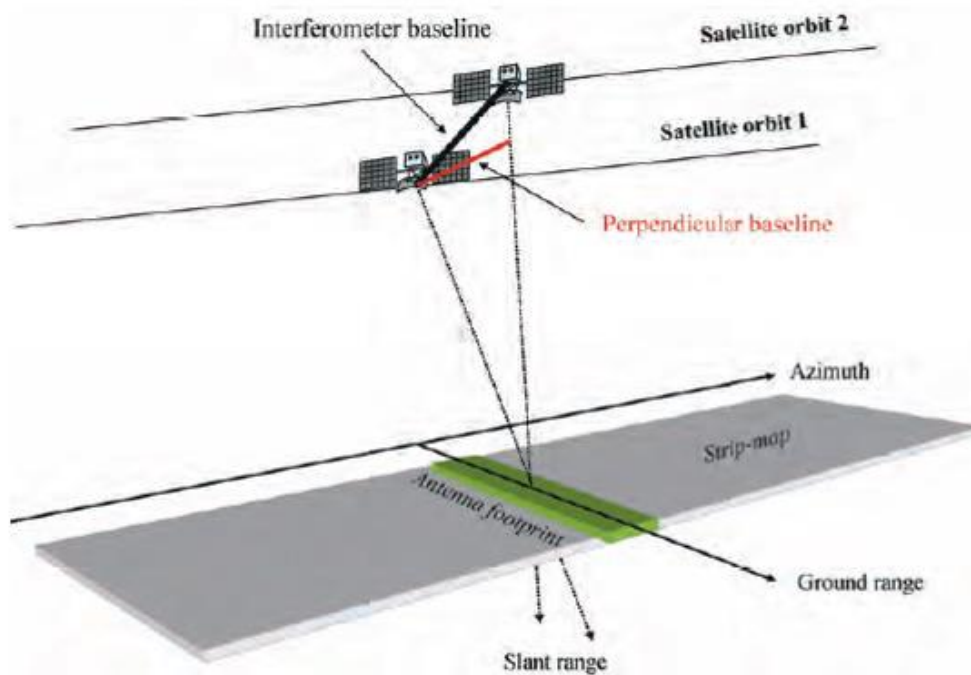


**Figure 2.4.** Geometry of satellite InSAR System. The orbit separation is called interferometric baseline, and its projection perpendicular to slant range direction is one of the key parameters of SAR interferometry.

## 2.2.2. BASICS OF SAR INTERFEROMETRY:

The basic property of imaging radar acquisitions enabling interferometric measurements is the control and measurement of the phase of the complex-valued radar signal. The scattered radar signal returned to the radar antenna from every resolution element in a SAR image is the coherent sum of the echoes from all scattering interactions in the resolution element. The exact way in which the contributions from the different scatterers are added up in the observed signal is not predictable. In this sense the signal phase in a SAR image is effectively random.

If two separate radar acquisitions are acquired realizing the same, or almost the same, viewing geometry over the same area, however, the summing of the contributions from individual scatterers is largely the same so that the phase difference between the two image acquisitions is not random. This can either be realized by using two physically separate antennas mounted on the same platform (single-pass interferometry) or two passes of the same antenna (repeat-pass interferometry), which is illustrated in fig 2.5.

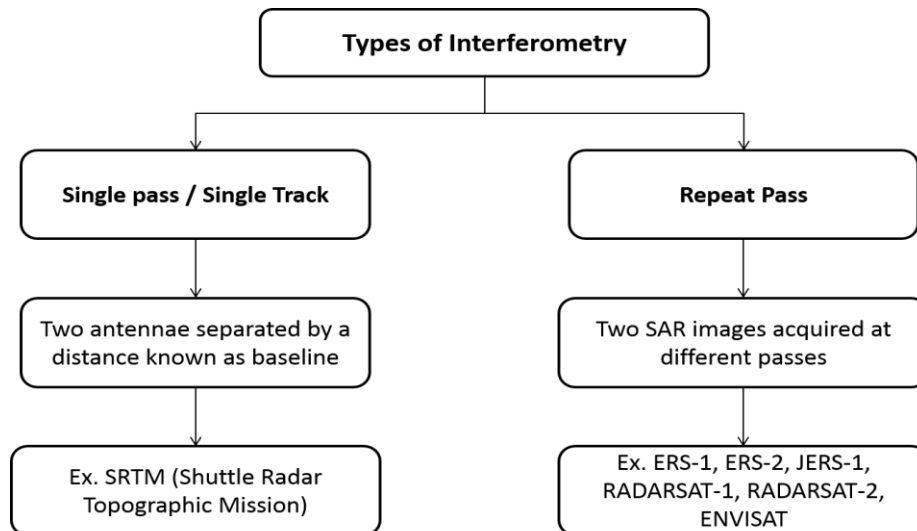


**Figure 2.5.** *Types of Interferometry Viz., single pass. Single track and repeat pass*

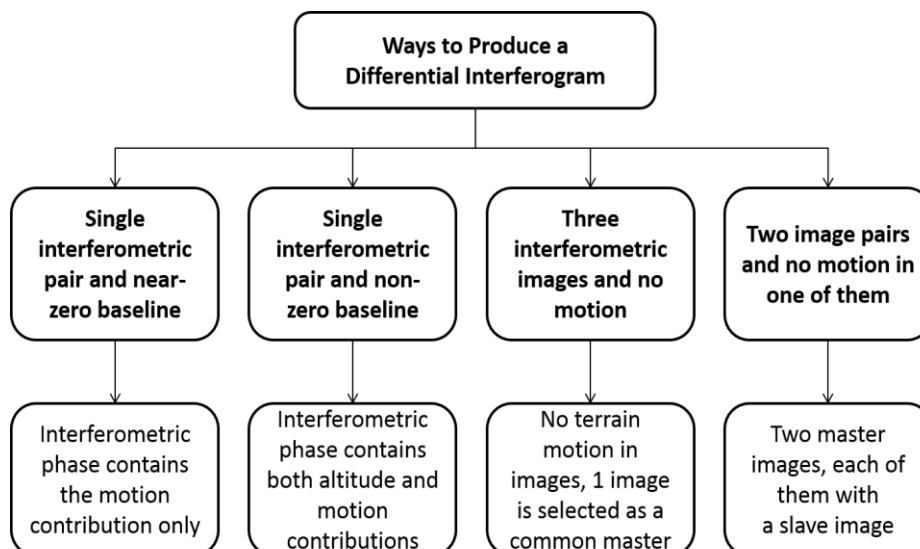


**Figure 2.6.** *Ways to produce a differential Interferogram*

An interferogram is formed from the two (complex) image signals,  $I_1$  and  $I_2$ , as

$$I = I_1 I_2^* = A_1 e^{i\phi_1} \cdot A_2 e^{-i\phi_2} = A_1 A_2 \cdot e^{i(\phi_1 - \phi_2)} = A \cdot e^{i\phi} \quad (2.2)$$

where  $*$  denotes the complex conjugate.  $A = A_1 A_2$  is the interferogram amplitude and  $\Phi = \phi_1 - \phi_2$  is the interferogram phase, which is the principal measurement in InSAR. For an identical imaging geometry and imaged surface, the two acquisitions would be identical apart from system noise, hence,  $I_1 = I_2$ , and the interferometric phase would be exactly zero everywhere. However, this is never observed in practice. The measured phase can be written as the sum of contributions from different processes (Zebker et al., 1994; Ferretti, Prati, and Rocca, 2000):

$$\Phi = \Phi_{topo} + \Phi_{def} + \Phi_{atm} + \Phi_n \quad (2.3)$$

Here,  $\Phi_{topo}$  is a phase contribution due to viewing the *topography* from two (slightly) different angles,  $\Phi_{def}$  is a phase contribution due to a possible movement of the imaged surface in the line-of-sight (LOS) direction,  $\Phi_{atm}$  is a phase contribution due to a difference in the optical path-lengths due to changes in the refractivity along the signal path, and  $\Phi_n$  is phase noise. Depending on the application, all of the first three terms on the right hand side of the above equation may be considered “signal” or “noise”.

If the viewing geometry remains exactly the same for the two SAR acquisitions,  $\Phi_{topo}$  is equal to zero. However, if the two antenna positions are separated by some distance  $B$  in the plane perpendicular to the antenna motion, called the interferometric baseline (fig. 2-9), different points on the surface will be at slightly different relative positions from the antennas. The interferometric phase contribution due to surface topography can be written as (Zebker et al., 1994; Hanssen, 2001):

$$\Phi_{topo} = -\frac{4\pi B_{\perp}}{\lambda r \sin\theta} dz + \phi_{flat\_earth} \quad (2.4)$$

where  $\lambda$  is the radar wavelength,  $r$  is the range (the distance between the radar and a point on the ground),  $\theta$  is the look angle (fig. 2.4), and  $dz$  is the surface elevation above a reference elevation. The term  $\Phi_{flat\_earth}$  is a deterministic phase contribution due to the reference surface, which for satellite systems is typically the reference ellipsoid. According to equation 2.4 the topographic phase signal after removal of the reference surface is directly proportional to the surface elevation and the perpendicular baseline. This equation is used to develop topographic maps from interferometry. In the study of surface displacements equation 2.4 is used to remove the topographic phase contribution from the signal. To do this the imaged topography must be known either from a digital elevation (or terrain) model (DEM or DTM), or be estimated from a separate “topographic” interferogram.

DInSAR phase  $\Delta\Phi$ DInSAR can be computed as:

$$\begin{aligned} \Delta \Phi_{DInSAR} &= \Delta \Phi - \Phi_{topo\_simulated} \\ &= \Phi_{Displ} + \Phi_{Atmos} + \Phi_{noise} + \Phi_{Res\_topo} \quad (2.5) \end{aligned}$$

where,

$\Phi_{\text{topo\_simu}}$  = simulated topographic phase using DEM

$\Phi_{\text{Res\_topo}}$  = the residual component due to errors in the simulation of  $\Phi_{\text{Topo}}$

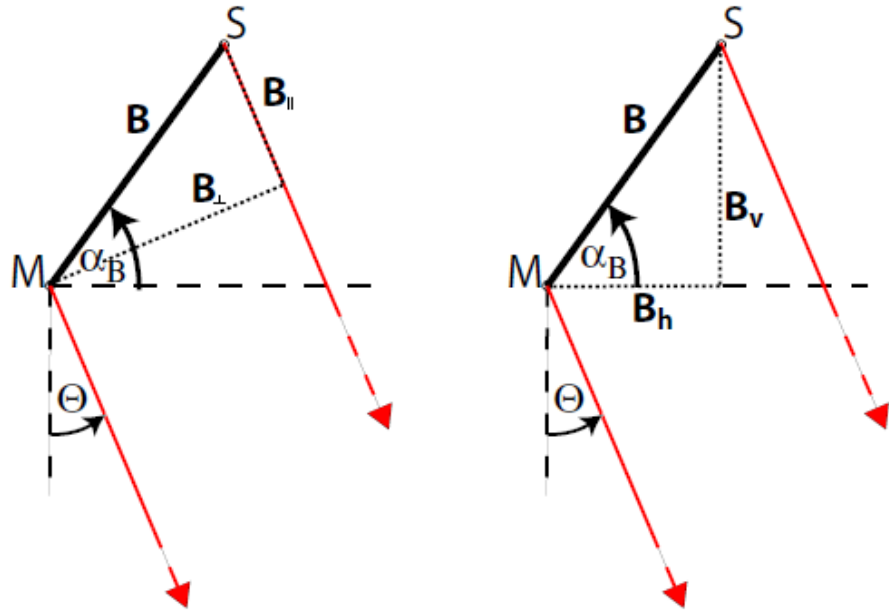


**Figure 2.7.** Different parameterizations of the InSAR baseline geometry.  $M$  and  $S$  are the two antenna positions in the plane perpendicular to the antenna flight path,  $B$  is the interferometric baseline,  $B_{\perp}$ ,  $B_{\parallel}$ ,  $B_h$  and  $B_v$  are the perpendicular, parallel, horizontal and vertical baselines, respectively.

If some process alters the position of the land surface between the two images acquisitions used to form the interferogram, the distance from the antenna to the scattering centers on the ground changes. If an area on the ground is displaced by  $\Delta r$  in the LOS direction of the radar, the path difference between the two acquisitions,  $2\Delta r$ , introduces an excess phase of,

$$\Phi_{def} = \frac{4\pi}{\lambda} \cdot \Delta r \quad (2.6)$$

Absolute displacements of the entire area imaged in a radar scene are only detectable to the precision to which the orbits are known. However, the power of the interferometric technique for deformation observations lies in the measurement of relative displacements between areas within the radar image. An ERS radar scene covers an area of about 100 km by 100 km, which is larger than the size of the surface expressions of many geophysical processes such as volcano inflations or deflations, most earthquakes, flowing glaciers, and compacting aquifer

systems. Thus, significant areas in the image can often be assumed to be stable between the two image acquisitions.

Observations say that phase spectrum of an image is more characteristic to the image than its magnitude spectrum (Berardino et al. 2002).

Phase consists of:

- i. Two way travel path (100s of kms divided by radar wavelength), corresponding to millions of cycles.
- ii. Interaction between incident EM waves and scatterers within SAR ground resolution cell.
- iii. Phase shift induced by processing system used to focus the image.

Note: Therefore a single SAR image is of no practical use.

If two SAR images for the same area, from slightly different viewing angles are considered (for interference), their phase difference can be exploited efficiently to generate an interferogram having a number of interference fringes. Interferogram is generated by cross-multiplying pixel by pixel, the first SAR with the complex conjugate of the second. Each interference fringe corresponds to a phase difference of  $2\pi$  between 2 component SAR images. Each fringe represents a complete cycle of a colour sequence (VIBGYOR) which equals to half of the wavelength.

$$\text{Amplitude of Interferogram} = A (\text{master}) * A (\text{slave}) \quad (2.7)$$

$$\text{Phase of Interferogram} = \Phi (\text{master}) - \Phi (\text{slave}) \quad (2.8)$$

This yields a displacement measurement in the LOS direction that is only limited by the ability to measure the interferometric phase. Under favourable conditions this measurement can be made to millimeter precision.

### 2.2.3. INTERFEROMETRIC SAR DATA STRUCTURE:

Interferometric datasets are supplied in complex formats i.e., single look complex (SLC) format which contains the information on phase as well as amplitude the scanned area. Each pixel in SLC format can be mathematically represented as  $a+ib$ . The expressions for amplitude and phase are as follows,

$$\text{Amplitude} = (a^2+b^2)^{1/2}; \text{ phase} = \tan^{-1} (b/a) \quad (2.9)$$

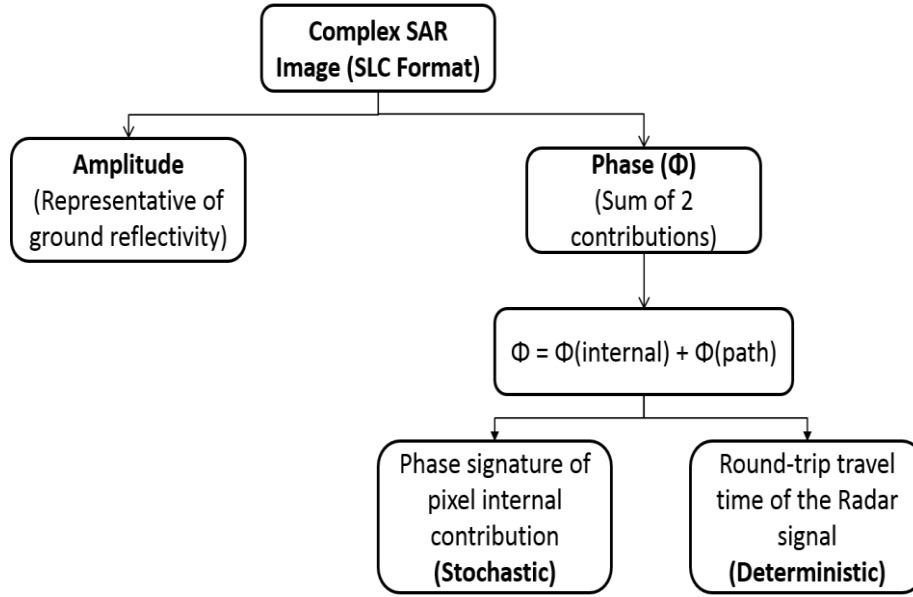


**Figure 2.8.** Interferometric SAR data structure

#### 2.2.4. INTERFEROMETRIC PROCESSING:

For generation of an interferogram, two SLC images are to be registered very accurately in both amplitude and phase (Rao and Rao, 1999). Subsequent to image registration, the phases of two SLC images are subtracted from one another and interferogram is generated. This is done by multiplying one input image with complex conjugate of the other input image.

Following parameters are estimated from the image pairs to check the suitability of the SAR images for interferometric processing,

- (i) Height of ambiguity:

$$AH = \frac{\lambda R \sin \theta}{4\pi B_n} \quad (2.10)$$

- (ii) Critical Baseline:

$$B_n (\text{critical}) = \frac{\lambda R \tan \theta}{2RR} \quad (2.11)$$

- (iii) Sensitivity:

$$AD = \frac{\lambda}{2} \quad (2.12)$$

Where,

$\lambda$  = wavelength of Radar signal;  $R$  = slant range distance of radar antennae;  $\theta$  = look angle of the radar;  $B_n$  = perpendicular baseline; and  $RR$  is range resolution.

Figure 2.9 shows the image processing steps performed to derive the surface displacement maps in this dissertation from radar interferograms. After SAR image formation, the two images are co registered with high accuracy before the interferogram is formed (eq. 2.2). The topographic phase contribution (eq. 2.4) is removed, using a DEM or tandem interferogram (an interferogram using two SAR acquisitions separated by only one day in time, thereby likely excluding any significant contribution due to deformation). Because the phase values are measured in the interval  $[0, 2\pi]$  (or in  $[-\pi, \pi]$ ), they need to be integrated to determine the absolute phase differences between locations in the image. This integration is called phase unwrapping. Different algorithms for phase unwrapping exist. The majority of the interferograms used in this dissertation were unwrapped using a minimum-cost network-flow (MCF) algorithm (Costantini, 1998). For the successful and accurate unwrapping of the interferogram it is often necessary to reduce the phase noise in the interferogram prior to unwrapping. This can be done by a variety of filtering operations, such as moving-average (mean or median) filters. Finally, to remove geometric distortions due to the radar imaging geometry the image can be rectified and geocoded. Because topography in the groundwater basins studied here was insignificant, this step was not critical. However, the geocoding of the resulting images helps in analysing the observations in their spatial relation to additional data (e.g., roads, buildings, benchmarks, well locations, etc.) from other sources.

To interpret surface displacements measured with InSAR techniques quantitatively it is important to understand and quantify the errors affecting the measurement. Until the mid-1990s most work related to InSAR focused on the applicability of the new technique to a variety of geophysical phenomena, generally overlooking or neglecting the issue of measurement reliability. Recent work has tried to further the understanding of errors and biases contained in interferometric phase measurements (Jonsson, 2002). A very good and comprehensive treatment of errors in radar interferometry has been presented by (Hanssen, 2001).

Most of the error contributions to deformation measurements with InSAR are not due to an inaccurate measurement of the interferometric phase. Rather, they derive from errors in relating the interferometric phase to the various signal contributions from surface topography, deformation, atmospheric delay, and changes in the refractive properties of the land surface.

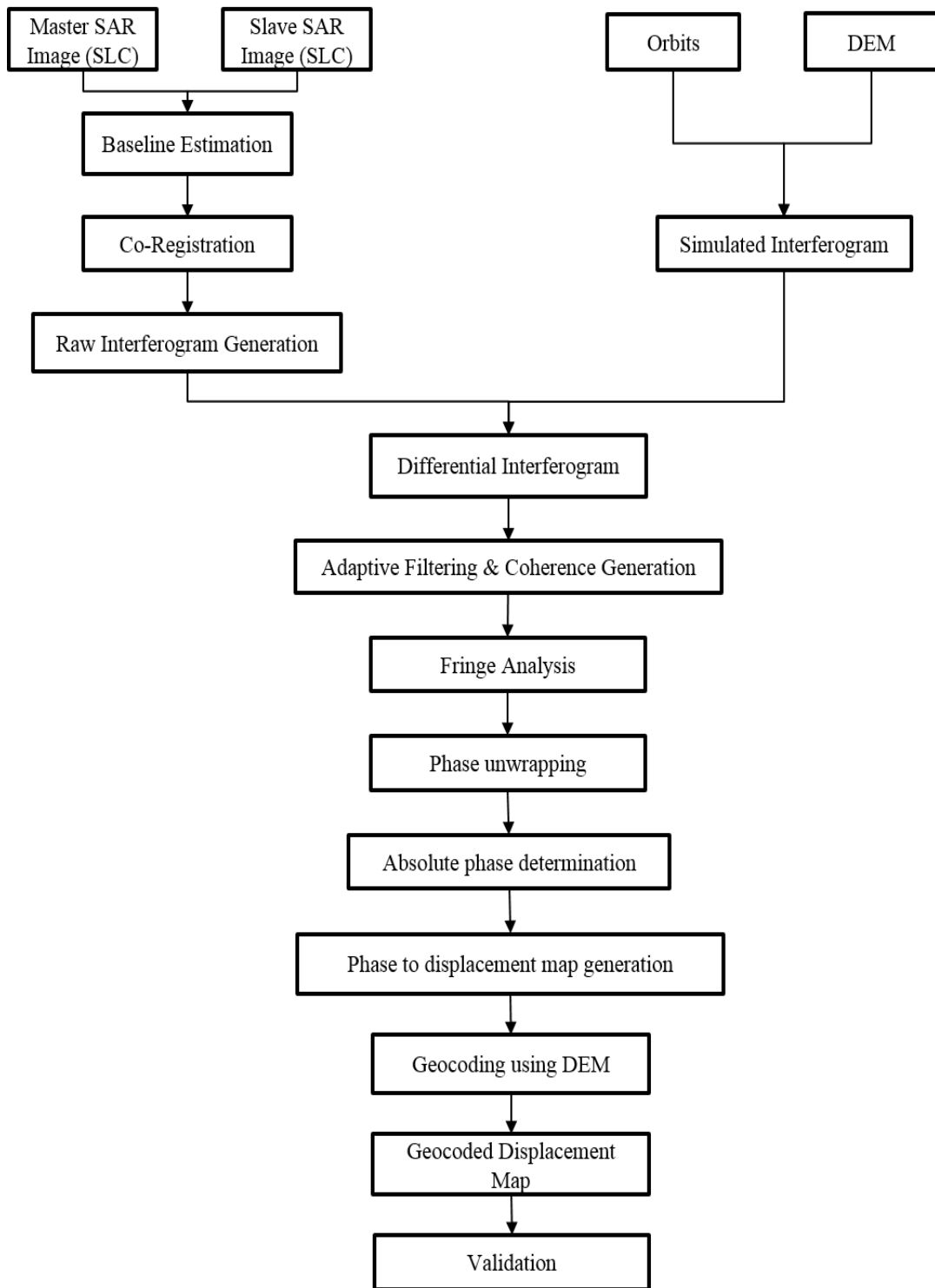


**Figure 2.1.** Image processing steps performed to obtain surface displacement maps from radar acquisitions. Steps in dashed boxes were not performed for all images.

## **2.3. AQUIFER COMPLEX LAYER COMPRESSION AND LAND SUBSIDENCE:**

Economic development and population growth has led to an increase in groundwater withdrawals from many aquifer systems. This development has often created a pronounced imbalance between water withdrawals and natural recharge, sometimes termed groundwater overdraft. Where groundwater withdrawals exceed recharge water is temporarily or permanently removed from storage in the system. Particularly in confined aquifer systems a large part of the storage can be due to the compressibility of the aquifer system materials. When water is produced from a compacting aquifer system or returned into storage causing expansion of the grain matrix the storage due to deformation of the aquifer system is an important part of the water budget.

Widespread aquifer system overdraft in the Kolkata city during much of the 20th century has resulted in large and often rapid declines in groundwater levels. It was recognized that the drawdowns of the groundwater levels were accompanied by subsidence of the overlying land surface (Chatterjee et al., 2006) as the removal of water from storage in compressible materials caused compaction of the aquifer system. A large number of case studies (Galloway et al., 1998; Sun et al., 1999; Amelung et al., 1999) have documented the global occurrence of this phenomenon. In some cases adverse effects of the subsiding land surface, such as increasing susceptibility to flooding or damage to drainage systems, wells or buildings, have made subsidence a primary constraint on groundwater development.

### **2.3.1. MEASUREMENT OF LAND SUBSIDENCE:**

Historically, land subsidence has been measured and monitored by repeatedly surveying geodetic benchmarks (fig. 2.10 a) and contouring the elevation changes (Ikehara and Phillips, 1994). Recent investigations have also included elevation changes measured in GPS surveys. In some cases borehole extensometers (fig. 2.10 b) have been installed to monitor aquifer system compaction continuously and with great accuracy. Recognizing the promise of using InSAR to measure land subsidence over compacting aquifer systems, (Galloway et al., 1998) were the first to use an interferogram spanning two years from 1993 to 1995 to characterize the subsidence field in Antelope Valley, California. (Amelung et al., 1999) presented subsidence maps for Las Vegas Valley, Nevada and noticed fluctuations in the subsidence rates during summer and winter seasons.

(Abidin et al., 2009) used InSAR-derived displacement maps to estimate inelastic storage coefficients and compaction time constants in a regional groundwater-flow and subsidence model for Bandung Basin in Indonesia.

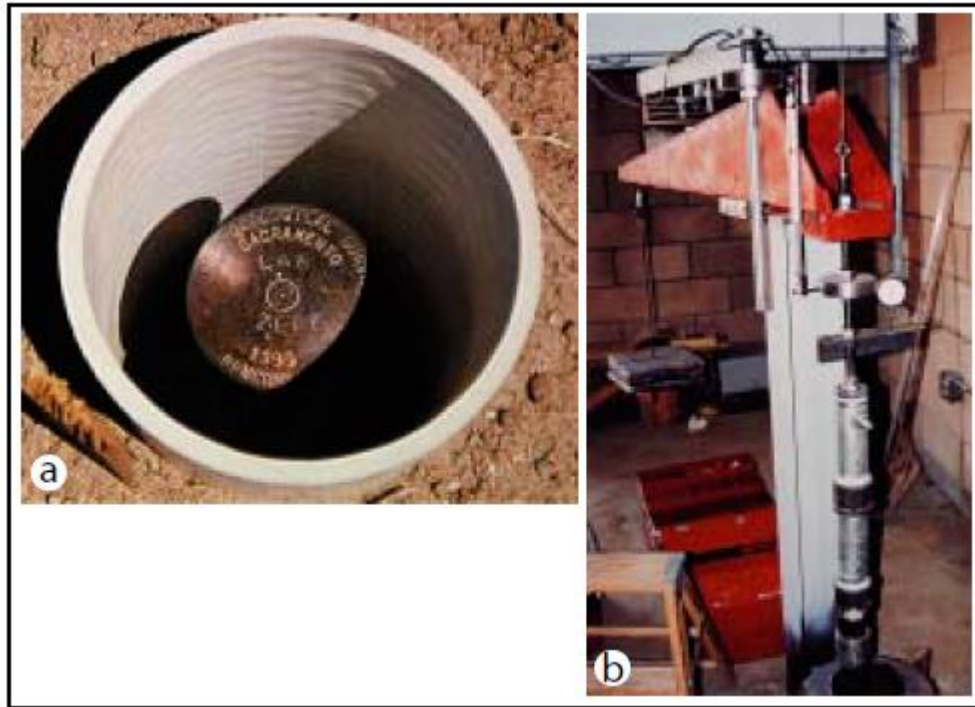


**Figure 2.10.** Benchmark (a) and extensometer (b) installed to monitor subsidence near Lancaster, Antelope Valley, California (Hoffmann 2003).

### 2.3.2. AQUIFER SYSTEM DEFORMATION:

The physical relationship between the displacements of the land surface measured by the various techniques and changes of the pore pressures in the aquifer system induced by groundwater pumping is presented in this section. I have focussed here on land subsidence due to compaction in sedimentary aquifer systems as aquifer system studied for this project belong to this category.

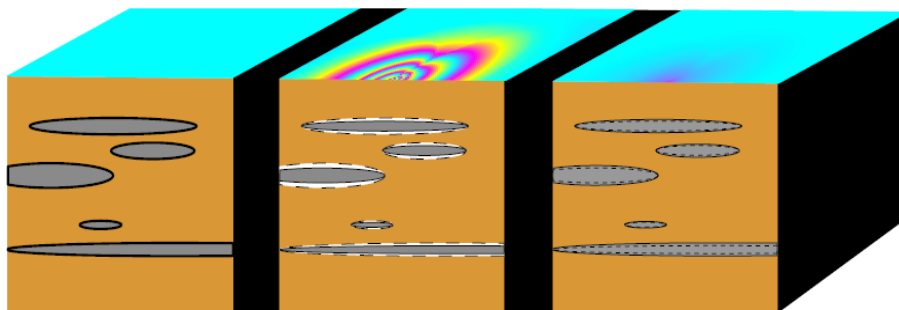


**Figure 2.11.** Before drawdown (left), after drawdown (centre) and after recovery (right)

An unconsolidated sedimentary aquifer system typically constitutes a series of relatively flat lying aquifers inter-bedded with aquitards that confine fluid pressures in the underlying aquifers. Land subsidence caused by the compaction of over-pumped aquifer systems occurs as a result of consolidation of aquitards (compressible silt and clay deposits) within the aquifer system. The aquifers usually consist of less compressible materials (sands, gravel), which do not yield as readily to stress changes and deform primarily elastically. This is shown schematically in fig. 2.10.

Aquifer system materials deform under changes in effective stress (Terzaghi, 1925),

$$\sigma'_{ij} = \sigma_{ij} - \delta_{ij}p, \quad (2.13)$$

where  $\sigma_{ij}$  are the components of the total stress tensor due to overburden and tectonic stresses,  $p$  is the pore pressure and  $\delta_{ij}$  is the Kronecker delta function. (Nur and Byerlee, 1971) presented a modified version of equation (2.13),

$$\sigma'_{ij} = \sigma_{ij} - \tilde{a}\delta_{ij}p, \text{ with } \tilde{a} = 1 - \frac{B}{B_s}, \quad (2.14)$$

where  $B$  and  $B_s$  are the bulk elastic moduli of the material matrix and the grains, respectively. Equation 2.14 would be identical to 2.13 if the bulk modulus of the grains is very large, i.e., the grains are incompressible. For typical aquifer system material, the coefficient  $\tilde{a}$  is very close to unity and equation 2.13 would be applied.

The Terzaghi principle of effective stress (eq. 2.13) states that for a constant total stress a change in pore pressure causes a change in effective stress of equal magnitude and opposite sign. The theory of poroelasticity, coupling the three-dimensional deformation field with pore pressure, was first developed by (Biot, 1941) and later extended to include anisotropic material properties (Biot, 1955; Carroll, 1979). Assuming isotropic material properties, the validity of Darcy's Law and Hooke's Law the pressure and strain fields in a saturated medium are described by the following system of coupled partial differential equations:

$$\frac{K}{\rho g} \nabla^2 p = \frac{\partial \varepsilon}{\partial t} + n\beta \frac{\partial p}{\partial t} \quad (2.15)$$

$$(\lambda + 2\mu)\nabla^2 \varepsilon = \nabla^2 p \quad (2.16)$$

Here  $K$  is the hydraulic conductivity,  $\rho$  is the density of the pore fluid,  $g$  is the gravitational constant,  $\varepsilon$  is the incremental volume strain,  $n$  is the porosity,  $\beta$  is the compressibility of the fluid,  $\lambda$  and  $\mu$  are Lamé's constants and  $t$  is time. A nice derivation of these equations can be found in (Todd, 1980). Equation (2.16) can be integrated to,

$$(\lambda + 2\mu)\varepsilon = p + f(\vec{x}, p), \text{ with } \nabla^2 f = 0 \quad (2.17)$$

In one dimension this becomes,

$$(\lambda + 2\mu)\varepsilon = p \quad (2.18)$$

Inserting eq. (2.6) into eq. (2.3) leads to the one-dimensional diffusion equation,

$$\frac{K_v}{\rho g} \cdot \frac{\partial^2 p}{\partial z^2} = \frac{(\alpha + n\beta)\partial p}{\partial t} \quad (2.19)$$

where  $K_v$  is the vertical hydraulic conductivity,  $z$  is the vertical coordinate, and  $\alpha$  is the compressibility of the material matrix. Equation (2.19) was derived prior to the (Biot, 1941) developments by (Terzaghi, 1925).

### **Horizontal deformation:**

In the study of aquifer system compaction, equation (2.19) has been used extensively, neglecting any horizontal deformation. Although it has been criticized that horizontal displacements can be important near a pumping well in an aquifer system (Helm 1994), most authors have ignored them (Riley, 1969; Galloway et al., 1998; Hoffmann, 2003).

The justification for neglecting horizontal deformation over extensive aquifer systems are often geometrical considerations. The compacting material is mostly contained in sub-horizontal layers that extend much farther laterally than vertically. Furthermore, the most compressive parts of the aquifer system are often clay and silt layers (either in confining units or interbedded), which have extremely low vertical hydraulic conductivities.

The pressure gradient within these layers is therefore almost exactly vertical, suggesting the one-dimensional simplification. Also, the compacting layers cannot move freely in the horizontal direction. Treating the problem in one-dimension corresponds to assuming a Poisson ratio of zero. Opening of fissures over deforming aquifer systems in Las Vegas Valley (Bell and Price, 1991), Antelope Valley (Blodgett and Williams, 1992) and elsewhere (Holzer and Johnson, 1985) evidence the existence of horizontal displacement, although they have not been clearly related to displacements in the confined part of the aquifer systems.

### **Hydraulic head**

In hydrogeology pore pressures in the water-bearing formations are commonly discussed in terms of hydraulic head is defined as follows,

$$h = h_z + \frac{p}{\rho g} = h_z + \frac{p}{\gamma_w} \quad (2.20)$$

The first term on the right hand sides,  $h_z$  is called the elevation head, the distance to an arbitrary reference surface. The quantity  $\gamma_w = \rho g$  is the specific weight (specific gravity) of water. When discussing changes in pore pressure or hydraulic head, the elevation head drops out and the hydraulic head changes are directly proportional to the changes in pore pressure. The advantage of using hydraulic head instead of pressure is that it is very easily related to the observable quantity, the level to which water rises in a well tapping the formation of interest.

### **Deformation and storage**

Two other important quantities in discussing compaction of aquifer systems are the specific storage,  $S_s$ , and the storage coefficient,  $S$ . The specific storage is a material property defined as the volume of water expelled from a unit volume of the aquifer system due to a unit decline

in hydraulic head (Todd, 1980). In a confined aquifer system water is derived both from reduction of pore space (resulting in compaction of the system) and expansion of the pore water as the pore pressure declines:

$$S_s = \alpha\gamma_w + n\beta\gamma_w = S_{sk} + S_w \quad (2.21)$$

The first term on the right hand side,  $S_{sk}$  is called the skeletal specific storage. For the more compressible fine-grained sediments in the aquifer systems,  $S_{sk} \gg S_w$  so that  $S_s \approx S_{sk}$  (Poland et al., 1975). The storage coefficient,  $S$ , is defined as the volume of water expelled per unit area from a layer of thickness  $b$  due to a unit decline in hydraulic head. Thus, it is given as,

$$S = bS_s \quad (2.22)$$

Similarly in eq. (2.9) the storage coefficient can be separated into the storage due to compaction of the layer, called the skeletal storage coefficient,  $S_s = bS_{sk}$ , and the storage derived from expansion of the water. Note that the definitions for  $S_s$  and  $S$  in equations (2.21) and (2.22) refer to the case of one-dimensional deformation.

Using the definitions in equations 2.20 and 2.21, the diffusion equation 2.19 can be written as,

$$\frac{\partial^2 h}{\partial z^2} = \frac{S_s}{K_v} \cdot \frac{\partial h}{\partial t} \quad (2.23)$$

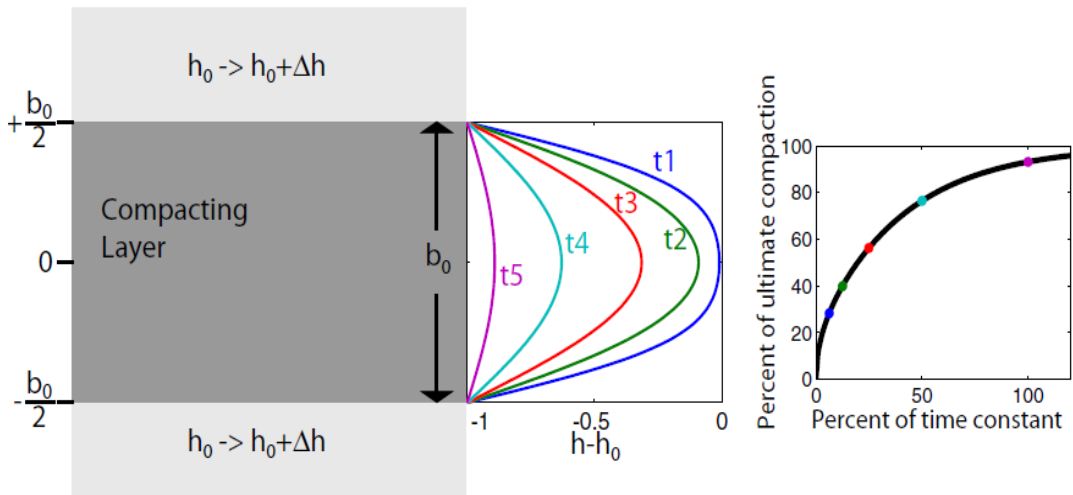


**Figure 2.12.** Compaction in a horizontal layer of thickness  $b_0$  due to a unit step decline  $\Delta h = -1$  of hydraulic head in the surrounding material. Head profiles across the layer are shown for several times,  $t_1$ -5 (center), indicated by coloured dots in the graph of subsidence over time on the right.

For this simple one-dimensional form with constant parameters, the analytical solution for the head in a horizontal layer of thickness  $b_0$  as a function of vertical position,  $-b_0/2 < z < b_0/2$ , and time  $t$  following a step decrease of hydraulic head at both layer boundaries at  $\pm b_0/2$  at time  $t = 0$  is given by the infinite series (Todd, 1980),

$$h(z, t) - h_0 = \Delta h - \frac{4\Delta h}{\pi} \sum_{k=0}^{\infty} \frac{(-1)^k}{2k+1} e^{-\frac{\pi}{4} \cdot \frac{t}{T_k}} \cdot \cos\left(\frac{(2k+1)\pi z}{b_0}\right)$$

where,  $T_k = \frac{\left(\frac{b_0}{2}\right)^2 S_S}{(2k+1)^2 k_v}$  (2.24)

Here  $h_0$  is the initial head throughout the layer and  $\Delta h$  is the instantaneous step change of head (fig. 2.24). A very good approximation to the exact expression in equation (2.24) is achieved with very few terms of the series. The value,

$$T = T_0 \frac{\left(\frac{b_0}{2}\right)^2 S_S}{k_v} \quad (2.25)$$

is called the compaction time constant. It is the time after which about 93% of the water that will drain from the layer in infinite time due to the step decline has drained from the layer. Thus, it is also the time after which 93% of the ultimate compaction due to the head change has been realized (Riley 1969).

If a system of  $N$  layers with identical  $K_v$  and  $S_S$  but different thicknesses  $b_n$  compacts due to the same,

$$b_{equiv} = \sqrt{\frac{1}{N} \sum_{n=1}^N b_n^2} \quad (2.26)$$

which results in the correct time constant if used in equation (2.25) (i.e., the time after which about 93% of the cumulative compaction in all bedding layers has occurred). Equation (2.26) enables much more efficient compaction computations for a system of interbeds. It is important to keep in mind though, that  $b_{equiv}$  as defined in equation (2.26) cannot be used in equation (2.22) to compute the total storage coefficient for all  $N$  number of layers, because  $b_{equiv}$  is generally smaller than the cumulative thickness of all interbeds for  $N > 1$ .

The deformation of geologic materials under applied stresses is described by their constitutive relations. The details of these relations are typically quite complex for geologic material and are rarely described accurately by analytical functions. Often the constitutive relations need to be idealized in order to incorporate them in physical or numerical models. For many unconsolidated fine-grained sediments, which constitute large portions of the aquifer systems under study, two dramatically different domains of deformation behaviour have been observed. If the stress exceeds any stress previously experienced by the material, the grain matrix is rearranged and compacts as it yields to the increasing stress. This compaction is permanent. The often large displacements resulting from these deformations are not recovered when the stress is released. Compaction occurring in this domain is termed “inelastic” or “virgin” compaction. If the stress changes without exceeding the maximum pre-existing stress, called the preconsolidation stress, the deformations are much smaller and mostly elastic.

This deformation behaviour is often described by assigning two different skeletal specific storages:

$$S_{sk} = \begin{cases} S_{skv}, & \sigma' > \sigma'_{max} \\ S_{ske}, & \sigma' \leq \sigma'_{max} \end{cases} \quad (2.28)$$

If the total stress due to the overburden and tectonic processes is assumed to remain constant, the preconsolidation stress,  $\sigma_{max}$ , can be expressed by the preconsolidation head,  $h_{pc}$ , the lowest hydraulic head experienced by the material.

Fig. 2.13 shows an idealized relation between effective stress change and compaction. In many cases the elastic deformations for coarse and fine-grained sediments can be approximated by the linear relation,

$$\Delta b = S_{ske} b_0 \Delta h = S_{ke} \Delta h, \text{ for } h > h_{pc} \quad (2.29)$$

Or,

$$S_{ke} = \frac{\Delta b}{\Delta h} \quad (2.30)$$

Inelastic compaction of coarse-grained sediments that typically constitute the aquifers within these aquifer systems is negligible. For many fine-grained sediments the relationship between compaction and effective stress change has been observed to be approximately logarithmic (Jorgensen, 1980).

$$\Delta b = \frac{b_0 C_c \Delta \log_{10} \sigma'}{1 + e_0}$$

Or,

$$S_{skv} = \frac{C_c \gamma_w}{\ln 10 \cdot \sigma' \sigma_0 (1 + e_0)} \quad (2.31)$$

Here  $C_c$  is the compression index and  $e_0$  is the void ratio. Equation (2.31) can be integrated to express the relation between the change in effective stress and thickness as,

$$b = b_0 \left( \frac{\sigma'_0}{\sigma'} \right)^a; \quad \text{Where, } a = \frac{C_c}{\ln 10 (1 + e_0)} = \frac{S_{skv} \sigma'_0}{\gamma_w} \quad (2.32)$$

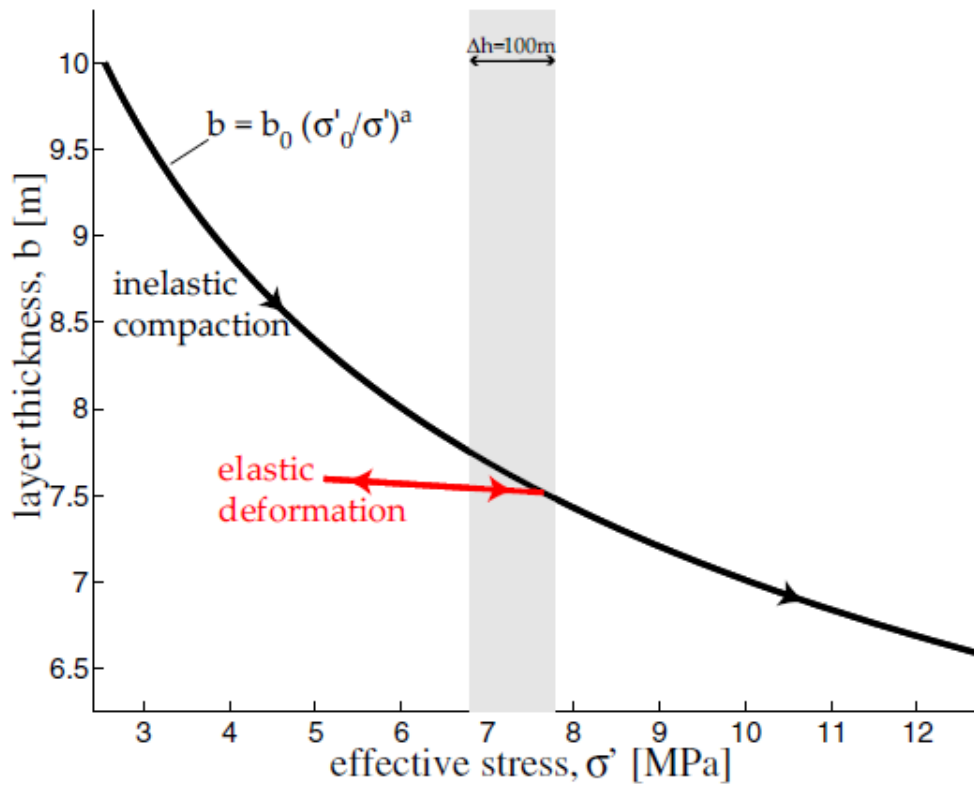


**Figure 2.13.** Idealized stress-strain relation for fine-grained sediments. The relationship is often approximately logarithmic for inelastic compaction (black) and approximately linear in the elastic range (red) of stresses. The width of the shaded area corresponds to a 100 m change in hydraulic head.

Compaction and expansion in multiple layered units typically contribute to the observed surface displacements over unconsolidated alluvial aquifer systems. Depending on the stresses in the aquifer system with respect to the preconsolidation stress the observed surface displacements have to be interpreted in terms of elastic deformation or non-recoverable inelastic compaction. Large-magnitude land subsidence observed over many aquifer systems is generally due to inelastic compaction of thick, highly compressible interbeds and confining units, consisting of compressible silt and clay deposits. The aquifer portions of an aquifer system are usually constituted of less compressible materials (sands, gravel) that deform mostly elastically, even when the preconsolidation stress is exceeded.

### 3. STUDY AREA

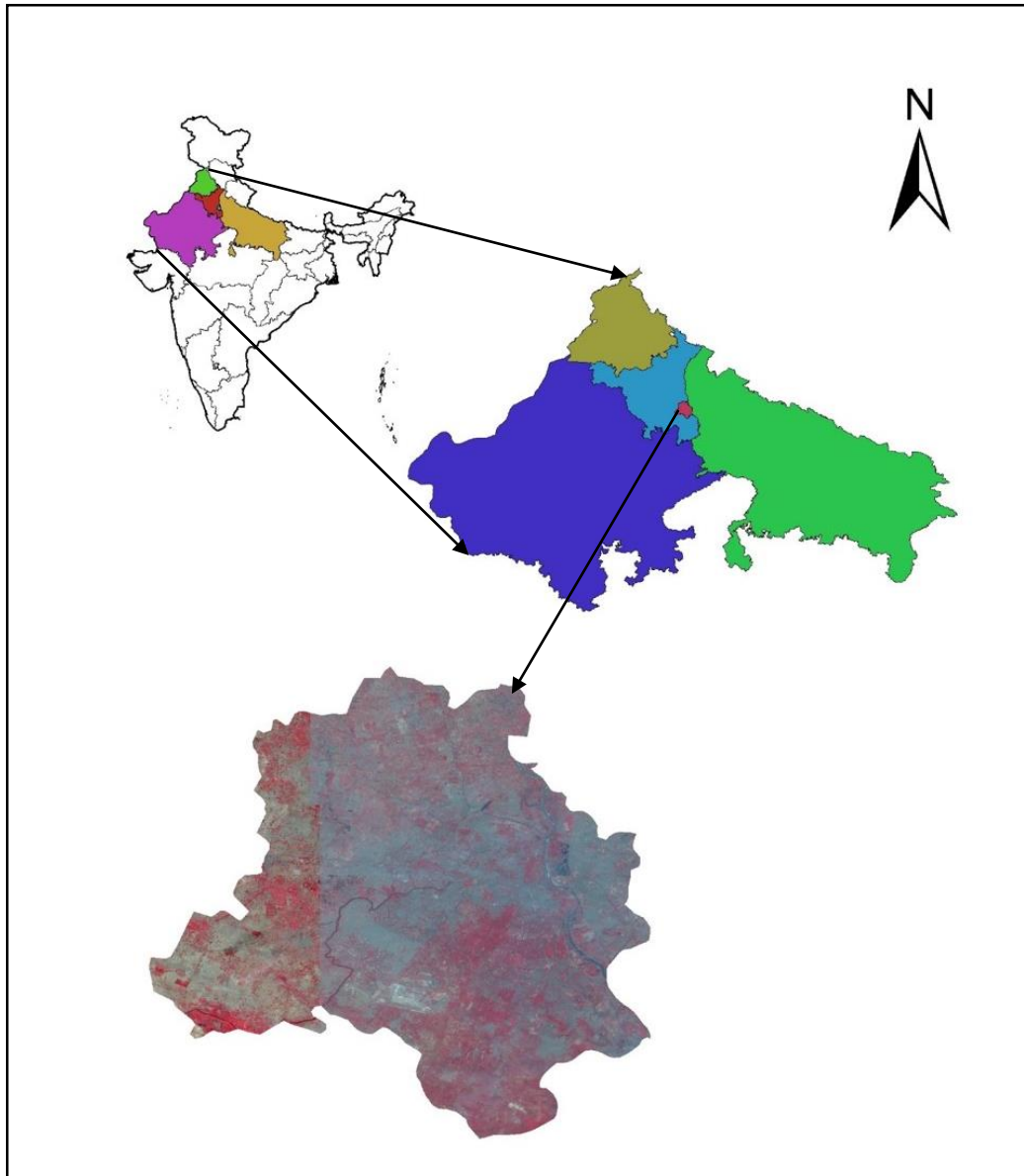


**Figure 3.1.** Map showing location of study area

#### **3.1. STUDY AREA FOR REGIONAL SURVEY:**

As depicted in earlier researches, North-West India is suffering from high rates of groundwater depletion since last decade (Rodell et al., 2009; Tiwari et al., 2009; CGWB, 2009). The area chosen for conducting regional scale study of groundwater storage change using GRACE level 3 product is North-West India including the states of Punjab, Haryana, Rajasthan, Utter Pradesh and Delhi. The area is bounded by  $68^{\circ}56'0.6''\text{E}$  and  $84^{\circ}55'16''\text{E}$  longitudes and  $22^{\circ}56'40''\text{N}$  and  $32^{\circ}58'28''\text{N}$  longitudes covering an area of 734647 sq. km.

The main physiographical sub-divisions are Indo-Gangetic alluvial plain in North India and aeolian plain and desert regions Western India. The area covers some of the most important cities of Delhi, Gurgaon, Chandigarh, Lucknow, Varanasi, Ballia, Hisar, Jaipur, etc.

The area is mainly covered by the quaternary sediments of the river basins of Ganga, Yamuna, Barmer, Churu, Ghaghar, Beas and Sutlej. The Ganga plain in Uttar Pradesh dominates the landscape and nearly covers three fourth of the geographical area of the State, lies between the rocky Himalayan belt in the north and the southern hilly tract comprised of mainly Pre-Cambrian rocks (“Directorate of Geology & Mining, Uttar Pradesh”, 2014). North-western parts of the Rajasthan are covered by vast blanket of young unconsolidated deposits including the blown sand of the Thar Desert. These include continuous Geological sequence of rocks from the oldest Archaean, Metamorphites, represented by Bhilwara Super Group (more than 2,500 million years old). The area in Rajasthan exposes wide variety of hard rocks, which include various types of metamorphic schists, quartzites, marbles and gneisses of Pre-Cambrian age with associated acid, and basic intrusive rocks. The sedimentaries include the rocks of Aravalli Super group, Delhi Super group, upper Precambrian Vindhyan Super group and of Cambrian to Jurassic, Cretaceous and Tertiary ages. The south-eastern extremity of the study area is occupied by a pile of basaltic flows of Deccan Traps of Cretaceous age (“Rajasthan - Geology”, 2013). The geological set-up of Haryana and Punjab comprises the sub-Himalayan system of rocks, mostly belonging to Siwalik Group which are exposed in the northeastern extremity and adjoining parts. The different geomorphic units recognised include 1) High structural hills, 2) Moderate structural cum denudational hills, 3) Low structural-cum-denudational hills, 4) Older and younger piedmont zones, 5) Flood plain, 6) Older Alluvial surface, 7) Aeolian zone, 8) Transitional zone & 9) Upland tract (Chopra , 1990).

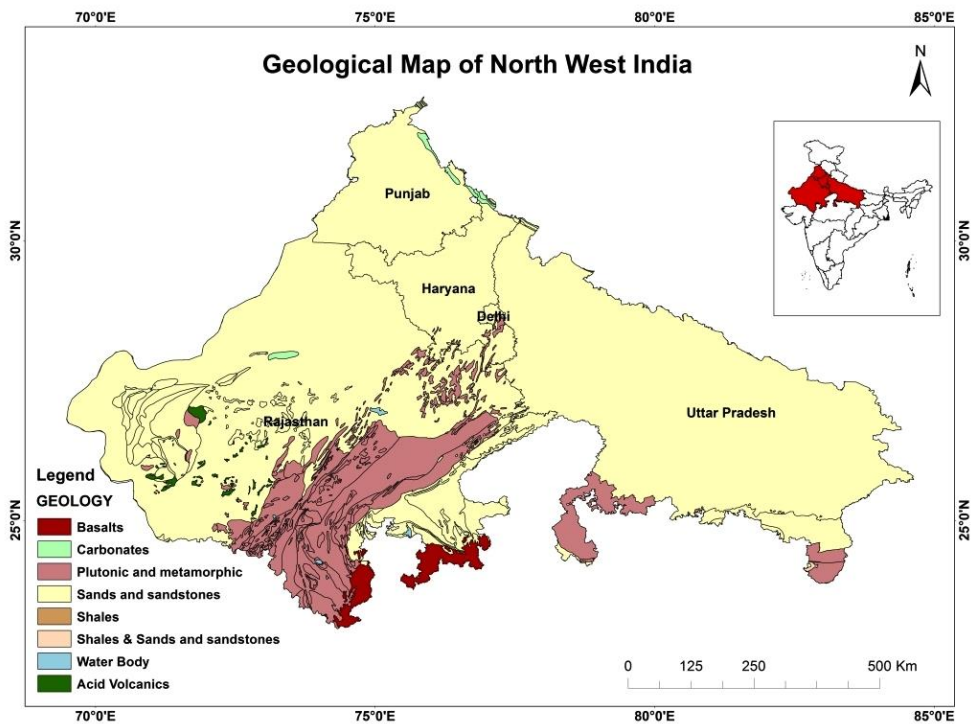


**Figure 3.2:** Geological map of North-West India covering the states of Rajasthan, Uttar Pradesh, Punjab, Haryana and Delhi.

### **3.2.STUDY AREA FOR DETAILED SURVEY:**

The National Capital Territory of Delhi being the largest metropolitan city in NW India holds foremost importance to conduct the extensive study to evaluate groundwater depletion scenario, aquifer layer compaction and resulting land subsidence.

National Capital Territory of Delhi lies between 28°24'30"N, 76°50'24"E and 28°53'00"N, 77°20'30"E and occupies an area of 1483 sq. Km. Area is covered under Survey of India Toposheet Nos. 53D and 53H. For administrative purposes, NCT Delhi is divided into 9 districts and 27 Tehsils/Subdivisions. NCT, Delhi has three Statutory Towns, 59 Census Towns and 165 Villages as per the census of 2011. The groundwater conditions in Delhi are controlled by the hydrogeological conditions characterized by the occurrence of different geological formations i.e., Delhi Quartzite (Delhi Ridge), older and younger alluvium and Yamuna flood plain.

#### **3.2.1. DEMOGRAPHY:**

The Decennial population census conducted during 2001, revealed that the population of NCT Delhi, as on March 1, 2011, worked out to be 16.8 million as against 13.9 million as on March 1991, and this figure is alarming as it beats the density of any other state by a huge margin. The decennial growth recorded during 2001-2011 comes out to be 21.21% which slightly exceeds the national growth rate of about 17%. The total population of Delhi accounts for 1.39% of All India population whereas in area, it is only 0.05% of total area of the country. The population density is 11320 persons/Sq. km area. South West Delhi shows highest population growth rate of 30.65%. The projected population of Delhi in 2011 comes out to be 18.45 million and in 2021 to be 24.48 million (Census, 2011).

#### **3.2.2. HYDROMETEOROLOGY:**

The normal annual rainfall in the NCT Delhi is 611.8 mm. The rainfall increases from the southwest to the northwest. However slight increase in rainfall is observed towards Yamuna River. About 81% of the annual rainfall is received during the monsoon months July, August and September. The rest of the annual rainfall is received as winter rain and as thunderstorm rain in the pre and post monsoon months. January is the coldest month with the mean daily maximum temperature at 21.3°C and the mean daily minimum at 7.3°C. May and June are the hottest months. While day temperature is higher in May the nights are warmer in June. From April the hot wind known locally as 'loo' blows and the weather is unpleasant. In May and June maximum temperature sometimes reach upto 46 - 47 °C. Humidity is high in the monsoon months. April and May are the driest months with relative humidity of about 30% in the morning and less than 20% in the afternoons (IMD, 2013).

#### **3.2.3. PHYSIOGRAPHY:**

The union territory of Delhi has four distinct physiographic units; these are as follows:

1. Delhi (Quartzitic) Ridge
2. Older alluvium on both side of the Delhi Ridge
3. Younger Alluvium –All along Yamuna Flood Plain

#### 4. Alluvium Deposits of Chattarpur Enclosed basin

The quartzitic ridge enters the area from the South-Eastern part and passes through the Eastern part extending up to the western bank of river Yamuna near Wazirabad. The rocky ridge has a length of about 35km and trends in a NNE-SSW direction. Isolated exposures of the quartzite are also found in the Western part of the area. The elevation of the crest of the ridge varies from 213 to 314 m above mean sea level with an average elevation of 40 m from the surrounding plain. The land surface on the Eastern side of ridge slopes towards the river Yamuna with a general gradient of 3.3 m/km. On the West side of the ridge the ground slopes towards the Najafgarh *Jheel* in the South-West. The alluvial plain in the area is almost flat and is interrupted by cluster of sand dunes and quartzite ridges. The sand dunes which are more prominent in the western part of the area are of varying dimensions and have North-East to South-West trend. The crests of these dunes generally lie between 3 to 10 meters above the surrounding plains. The dunes in the area are more area less fixed with vegetation on them. The dunes are mostly longitudinal in nature. The nearly closed alluvial basin of Chattarpur (28°25'30" to 28°32'30" N and 77°07'30" to 77°13'00" E) in South Delhi occupies an area of about 78 km<sup>2</sup>. This is a closed inland basin, the boundary of which is marked by the quartzite ridges. The general slope of the land is towards the center of the basin from the surrounding ridges. The slope in the southern part of the basin is towards south. The maximum land altitude in the basin is about 259 m MSL whereas the land at the ridges is about 274 m MSL. Younger alluvium (Flood Plain) deposits are confined all along the river Yamuna, which are presently demarcated by embankment on both sides of the river. Virtually, this is an active flood plain domain covering an area of nearly 97 sq. km, characterized by granular deposits with shallow depth to water level. Presently, the entire flood plain area is protected by constructing embankment running all through Dahia Border to Badarpur border on Western bank and Loni border to Mayur Vihar border on the Eastern bank of Yamuna River within National Capital Territory. The depth to water level varies from 3 to 6 mbgl in active flood plain (CGWB, 2013).

The river Yamuna is the only perennial river flowing in the Southerly direction. Either side of the river Yamuna is marked by the extensive alluvial flood plain. The aerial extent of the active flood plain in NCT Delhi is 97 sq. km. The flood plains towards the North falls in Narela and Civil-lines tehsils of North District, the Central parts fall in North-East district and Daryaganj tehsil of Central district and the Southern most part falls in Saidabad and Kalkaji tehsil of South district. In general, the alluvial flood plain slope is towards South. The average slope of the Yamuna River bed from North to South is 0.4 m/km. Eastern and Western Yamuna Canal and Agra Canal are the three major canals originating from the river with Bawana, Rajpur and Lampur distributaries. A dense network of lined canals system exists in the North-Western part of the state.

A number of micro watersheds originate from the quartzite ridge. The drainage on the East of the ridge enters river Yamuna, whereas on the West, it enters natural depressions located in Najafgarh Tehsil of South-West district. The geographical area of NCT Delhi, is broadly divided into seven drainage basins, ultimately discharging into the Yamuna – (I) The Najafgarh Drain is about 39 Km long, flows North-Easterly and joins Yamuna River at Wazirabad in North Delhi. (ii) Supplementary drain, (iii) Barapullah drain. (iv) Wild life sanctuary area, (v) Drainage of Shahadra area, (vi) Bawana drain basin, (vii) Other drains

directly out falling into river Yamuna on right bank. Swamp areas are common along the flood plains of Yamuna.

#### **3.2.4. GEOLOGY:**

NCT Delhi is occupied by Quartzite inter-bedded with Mica-Schist belonging to Delhi Super Group. Unconsolidated sediments of Quaternary to Recent age unconformably overlie these. The quartzite is grey to brownish grey, massive to thinly bedded and structurally form a coaxially refolded regional Anti-form plunging towards South-West. The major planar structure strikes NE-SW with steep South-Easterly dips. Quartzite occurs in the Central and Southern part of the area while the Quaternary sediments comprising older and newer alluvium cover the rest of the area. The older Alluvium comprises silt and clay mixed with kankar in varying proportions. The Newer Alluvium mainly consists of un-oxidized sands, silt and clay occurring in the Yamuna flood plain. The thickness of alluvium on eastern and western side of the ridge is variable but west of the ridge it is generally thicker (>300 m). The area is dissected by number of faults, fractures and shears; the trend of these varies from NNE-SSW to ENE-WSW. The important faults west of the ridge area are Rajendra Nagar fault, MES Depot, East Patel Nagar fault, Anand Parbat, West Patel Nagar fault and Inderpuri fault. The notable faults east of the ridge are Kishangarh fault, a WNW-ESE trending fault between Qutab Minar and Mehrauli and Lado Sarai fault.

#### **3.2.5. ALLUVIAL AQUIFERS:**

In Delhi state alluvial areas, characterized by occurrence of number of sand zones constituting the aquifers, it may not be essential to install piezometers for each sand zone. Based on inter-relationship and behaviour, these aquifers are grouped into major aquifer systems and piezometers have been installed accordingly. In National Capital Territory of Delhi and adjoining, the hydrogeological mapping and ground water exploration indicates the presence of three distinct potential aquifer groups within the depth of 450 m below ground level. Each of these aquifer groups comprises of number of individual sandy horizons. The grouping of aquifers was done as follows:

1. Aquifer Group I - Down to 65 m. below ground level (Un-confined)
2. Aquifer Group II- Between 65 to 200 m. below ground level (Confined/ Semi-Confined)
3. Aquifer Group III- Between 200 to >300 m. below ground Level (Confined)

#### **3.2.6. SOIL TYPE:**

The soils in a greater part of Delhi are light textured, while medium texture soils are found in a small part of the area. Light textured soils are represented by sandy, loamy, sand and sandy loam type of soils. The medium textures soils are represented by loam and silty loam.

(a)



(b)



(c)



**Figure 3.3:** (a) Delhi quartzite; (b) older alluvium of aeolian deposits; (c) younger alluvium of Yamuna flood plain.

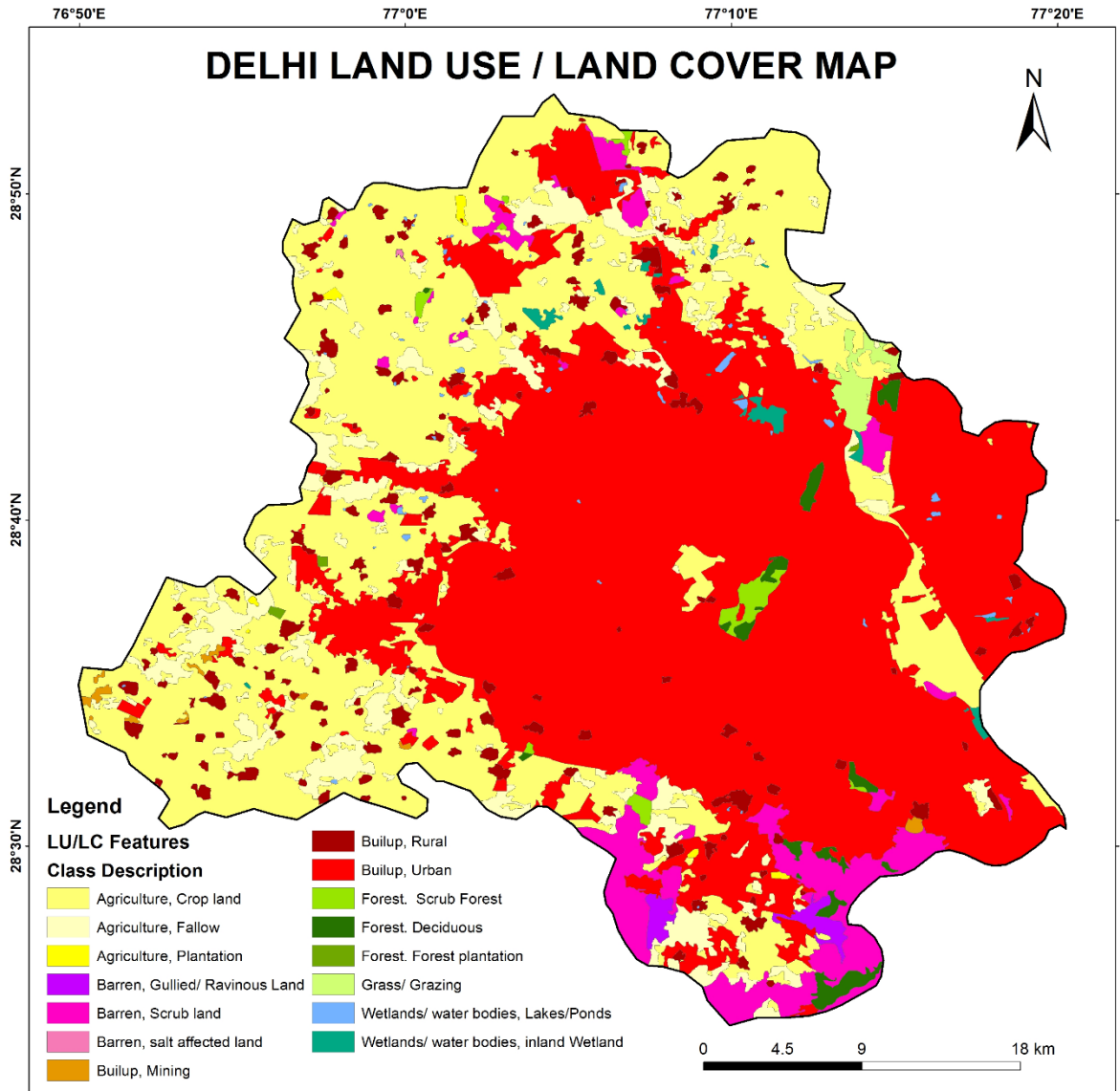


**Figure 3.4:** Land use / land cover map of Delhi NCT

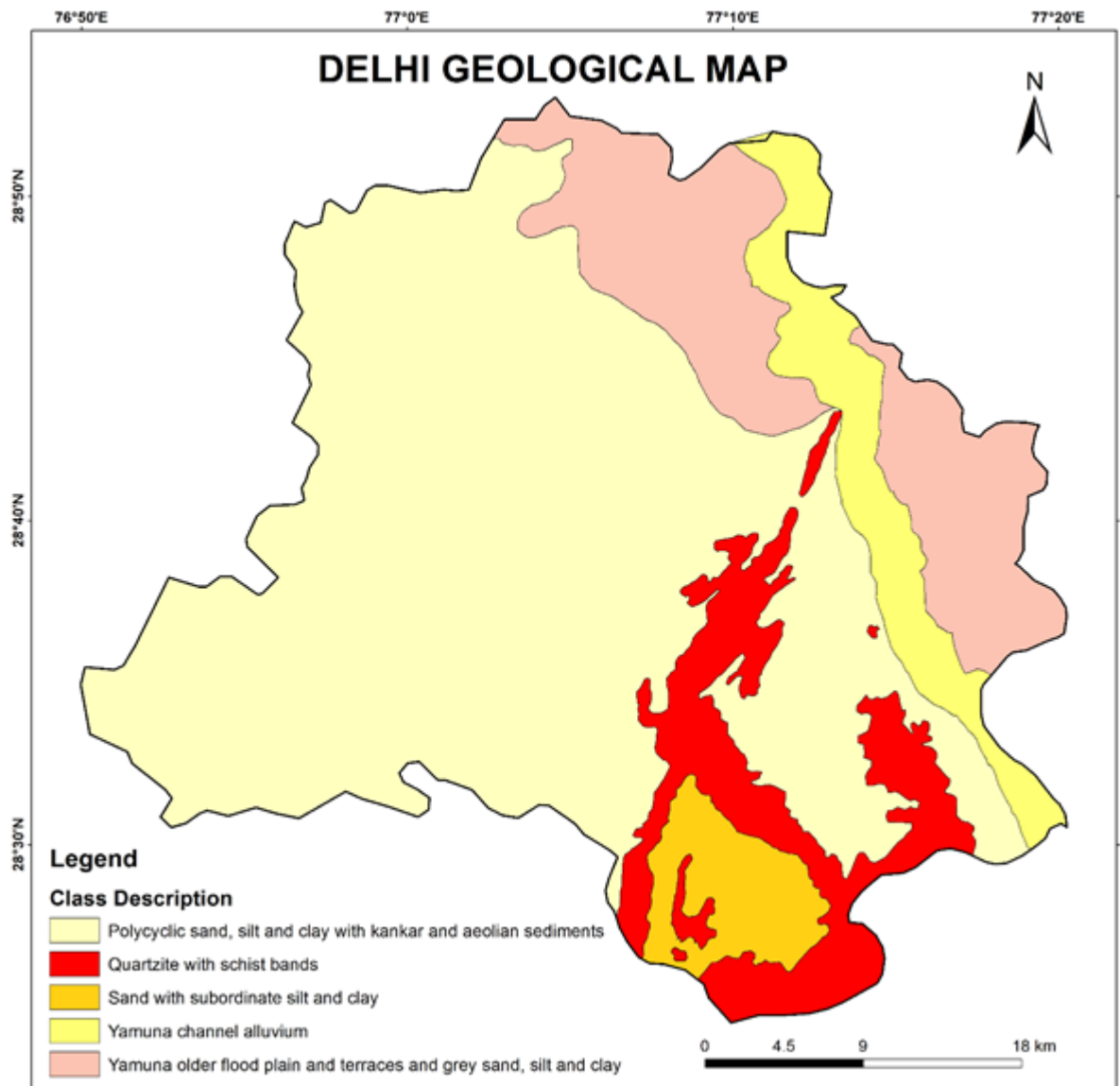


**Figure 3.5:** Geological map of Delhi NCT

### 3.3. GROUND WATER SCENERAIO IN DELHI NCT:

#### 3.3.1. POTENTIAL AQUIFERS:

Ground water exploration carried out in the depth range of 50 to 150 m in Delhi in Quartzite recorded a discharge of in the range of 2 to 18 cubic metre/ hour with a drawdown of 8 to 30 m. The transmissivity of the formation is 5 to 135 sq.m/ day. The Quaternary deposits in the form of Aeolian and alluvial deposits constitute the major repository of ground water in the area. The thickness of unconsolidated sediments towards east of the ridge gradually increase away from the ridges, with the maximum reported thickness being 170 m. In the south-western, western and northern parts of the area, the thickness of sediments is more than 300 m except at Dhansa where the bedrock has been encountered at 297 m below land surface. In

Chattarpur basin, the maximum thickness of sediments is 116 m. The Aeolian deposits are mainly loam, silty loam and sandy loam. The bedrock is overlain by these deposits. Older alluvial deposits consists mostly of interbedded, lenticular and inter fingering deposits of clay, silt, and sand along with kankar. Tubewells in this formation are explored upto the depth of more than 300m. However, fresh water zones are encountered upto the depth of 90 m only. The yield of the wells are generally in the range of 8 to 35 cubic metre/ hour with drawdown of 6 to 24 m (Rao et al. 2011).

The transmissivity of the formation ranges between 130 and 400 sq.m./day. These deposits overlay the Aeolian deposits and are in turn overlain by the newer alluvium, which occurs mostly in the flood plains of river Yamuna. The tubewells upto the depth of 50 m generally yield 100 to 210 cubic metre / hour with drawdown of 5 to 11 meter. The transmissivity of the formation ranges between 1300 to 2000 sq.m/day. The tubewells drilled in the Chattarpur basin have recorded yield of 7 to 14 cubic meter/ hour with drawdown of 12 to 20 m (Rao et al., 2011).

### **3.3.2. MAJOR GROUND WATER RELATED PROBLEMS:**

Qualitatively, NCT Delhi has three major problems – salinity, fluoride and nitrate. There is a large variation in saline fresh water interface in the horizontal and vertical direction. In NCT Delhi, the fresh saline interface varies from 22m (North West district, excluding the area of Yamuna Flood Plain) to > 100m (South district) (Shekhar et al., 2009).

The existence of saline water at shallow depth inhibits the development of fresh ground water. Fluoride concentrations in ground water is more than 1.5mg/l in more than 30 percent of the area. The fluoride affected areas are spread mainly in the South-western and Western part of the city comprising Southwest, West and Northwest districts. Nitrate concentration is significant particularly in the parts of West, Southwest and some pockets in Northwest districts. Concentration is more at shallow levels but decreases at deeper levels. Near Okhla – Kalindi Kunj Barrage, high nitrate in ground water is observed on the western bank of the river Yamuna (CGWB, 2013).

## **4. DATA USED AND METHODOLOGY**

### **4.1. OVERVIEW:**

The ground water depletion scenario in North West India was studied at a regional scale for 2003-12, using coarse resolution JPL RL05 product of GRACE mission i.e., monthly  $1^0 \times 1^0$  grid terrestrial water storage data (equivalent water column thickness in cm) and soil moisture and precipitation data from GLDAS-2.0 NOAA Model  $1^0 \times 1^0$ . The data being at same resolution was used to estimate the change in groundwater storage. The results were plotted and compared with the trend of precipitation over same time period. The maps were prepared for decadal terrestrial water storage change, groundwater storage change for pre-monsoon and post-monsoon. As the area covered in this part of study was very huge, so the results were validated for Delhi pixel.

The next step of the study involved the extensive study to detect land subsidence in Delhi National Capital Territory using Differential Interferometric Synthetic aperture Radar (DInSAR) technique. The data used were ALOS PALSAR (Dec-2009 to Jan-2011) and RADARSAT-2 (Dec-2013 to March-2014) interferometric pairs. The temporal baseline of the interferometric pairs ranges from 48 days to 414 days. SRTM DEM (90 m resolution) was used for interferogram generation. The interferograms were then filtered and further processed and geocoded to obtain the deformation maps and deformation rate for fringes was calculated and validated. IRS-P6 LISS-III image was used for map composition.

The data specifications and detailed methodology is discussed in the latter part of the chapter.

### **4.2. DATA USED:**

#### **4.2.1. THE SATELLITE DATA USED FOR GROUND WATER STORAGE CHANGE ESTIMATION ARE LISTED BELOW:**

1. Terrestrial Water Storage (equivalent water thickness in cm)

Product specifications: JPL RL05 Land Data product (time mean removed 2004-2009)

Source: Gravity Recovery and Climate Experiment (GRACE)

Spatial Resolution:  $1^0 \times 1^0$  (111 km x 111 km approximately)

Time period: Jan-2003 to Dec-2012

Online directory: (“GRACE Tellus: GRACE MONTHLY MASS GRIDS - LAND”, 2013)

2. Soil Moisture layers 1, 2, 3, 4 (expressed in  $\text{Kg/m}^2$ )

Product specifications: GLDAS-2.0 NOAA Model

Source: Global Land Data Assimilation System (GLDAS)

Spatial Resolution:  $1^0 \times 1^0$  (111 km x 111 km approximately)

Time period: Jan-2003 to Dec-2012

Online directory: (“Giovanni - Global Land Data Assimilation System (GLDAS)”, 2013)

3. Precipitation (expressed in cm)

Product specifications: GLDAS-1 CLM Model

Source: Global Land Data Assimilation System (GLDAS)

Spatial Resolution:  $1^0 \times 1^0$  (111 km x 111 km approximately)

Time period: Jan-2003 to Dec-2012

Online directory: (“Giovanni - Global Land Data Assimilation System (GLDAS)”, 2013)

**4.2.2. DATA SPECIFICATIONS USED FOR DINSAR PROCESSING:**

The data used for DInSAR processing involves ALOS PALSAR and RADARSAT-2 images for Delhi area. The sensor specifications are listed in table 4.1.

**Table 4.1.** *Sensor Specifications for SAR Data*

Sensor	Wavelength ( $\lambda$ )	Range x Azimuth	Resolution	Temporal Resolution
ALOS PALSAR	23.6 cm (L-Band)	4.6 m x 5.1 m	10 m	46 days
RADARSAT-2	5.6 cm (C-Band)	11.8 m x 5.1 m	13.5 m	24 days

A total of 4 ALOS PALSAR and 3 RADARSAT-2 scenes were acquired. The data specifications for ALOS PALSAR and RADARSAT-2 are illustrated in table 4.2 and 4.3 respectively.

**Table 4.2.** *ALOS PALSAR (L-Band) Data Specifications*

S. No.	Orbit	Acquisition Date	Mode	Polarization	Frame	Direction
1	20548	02/12/2009	FBS	HH	560	Ascending
2	21219	17/01/2010	FBS	HH	560	Ascending
3	21890	04/03/2010	FBS	HH	560	Ascending
4	26587	20/01/2011	FBS	HH	560	Ascending

**Table 4.3.** *RADARSAT-2 (C-Band) Data Specifications*

S. No.	Orbit	Acquisition Date	Polarization	Frame	Direction
1	455005	03/12/2013	HH	46350	Ascending
2	455006	20/01/2014	HH	46350	Ascending
3	455007	09/03/2014	HH	46350	Ascending

SRTM (Shuttle Radar Topography Mission) Digital Elevation model version 4.1 was used in the generation of interferograms. The specifications of SRTM DEM are listed in table 4.4.

**Table 4.4.** *Specifications of SRTM DEM Version 4.1*

Band	X-Band
Spatial Resolution	90 m
Raster size	1°x 1° Long & Lat
Datum (Horizontal & Vertical)	WGS84
Data format	16-Bit Signed Integer
Horizontal accuracy (absolute)	±20 m 90% circular error
Horizontal accuracy (relative)	± 15 m 90% circular error
Vertical accuracy (absolute)	±16 m 90% vertical error
Vertical accuracy (relative)	±6 m 90% vertical error

#### **4.2.3. ANCILLARY DATA:**

The ancillary data used for in the study are listed below,

1. Survey of India Toposheets No. 53D and 53H for Delhi Area.  
Source: Survey of India
2. Geological Map of Delhi  
Source: Central Ground Water Board
3. Land Use / Land Cover Map of Delhi  
Source: Bhuvan, NRSC
4. Geological, Geomorphological maps of North West India (1:1M Scale)  
Source: Geological Survey of India (GSI).
5. Ground water level data for Delhi NCT (2003-12)  
Source: Central Ground Water Board

### 4.3. METHODOLOGY:

The methodology adopted for the study is illustrated briefly in fig 4.1.

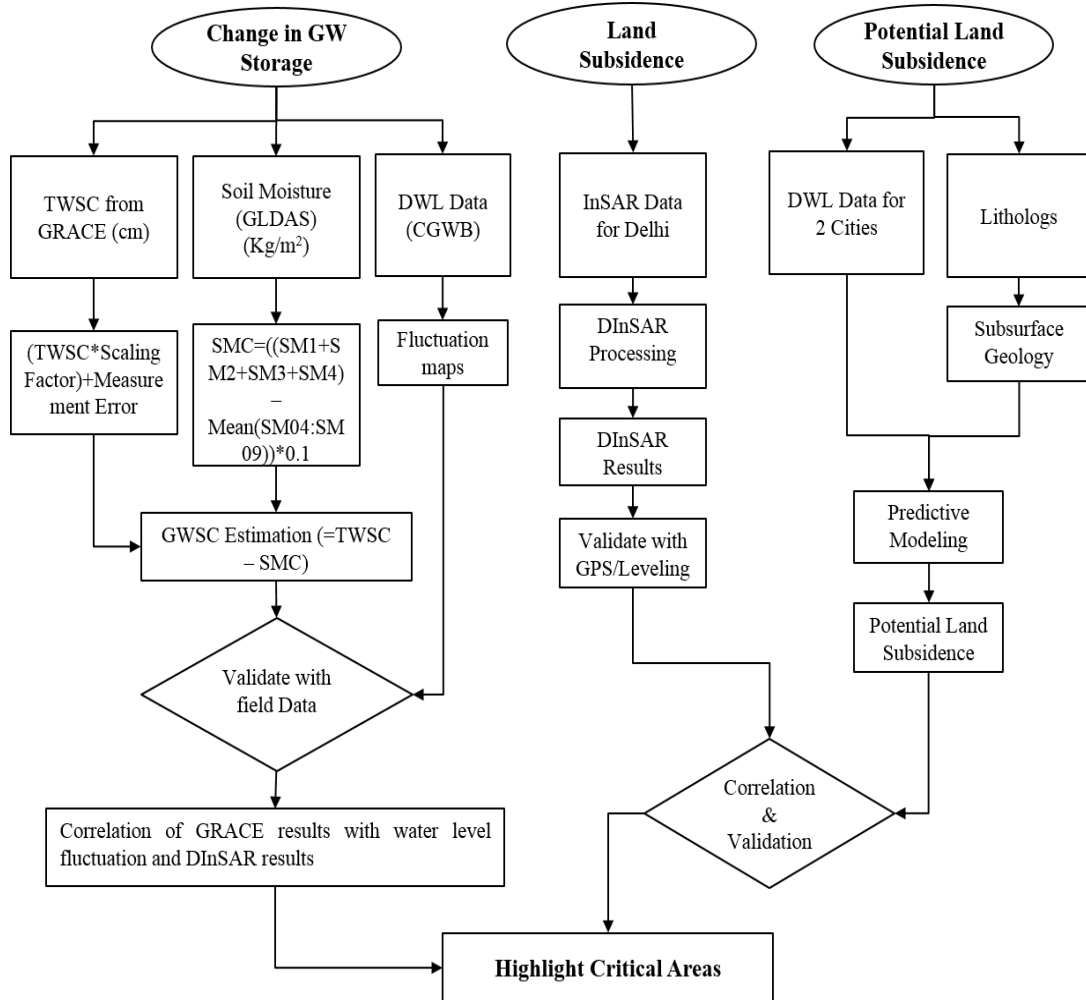


**Figure 4.1.** Flow chart showing the brief methodology for the project.

#### 4.3.1. METHODOLOGY FOR GROUND WATER STORAGE CHANGE ESTIMATION USING GRACE DATA:

Ground water storage change depends upon the terrestrial water storage and soil moisture. It is calculated by using following equation,

$$GW_{\alpha} = TWS_{\alpha, GRACE} - (SW_{\alpha} + SM_{\alpha} + SP_{\alpha}) \quad (4.1)$$

Where  $GW_{\alpha}$  = groundwater storage anomaly;  $TWS_{\alpha}$  = total water storage anomaly;  $SW_{\alpha}$  = surface water storage anomaly;  $SM_{\alpha}$  = soil moisture storage anomaly;  $SP_{\alpha}$  = snowpack storage anomaly.

Due to absence of snow cover in the study area and relevant data regarding surface water volume, I could not use these entities in the ground water storage change estimation. Also only small quantity of water is present in the form of surface water as compared to total water storage in earth's crust, we may get satisfactory results even by not using this entity in our calculation. The methodology for the same is illustrated in fig (4.2).

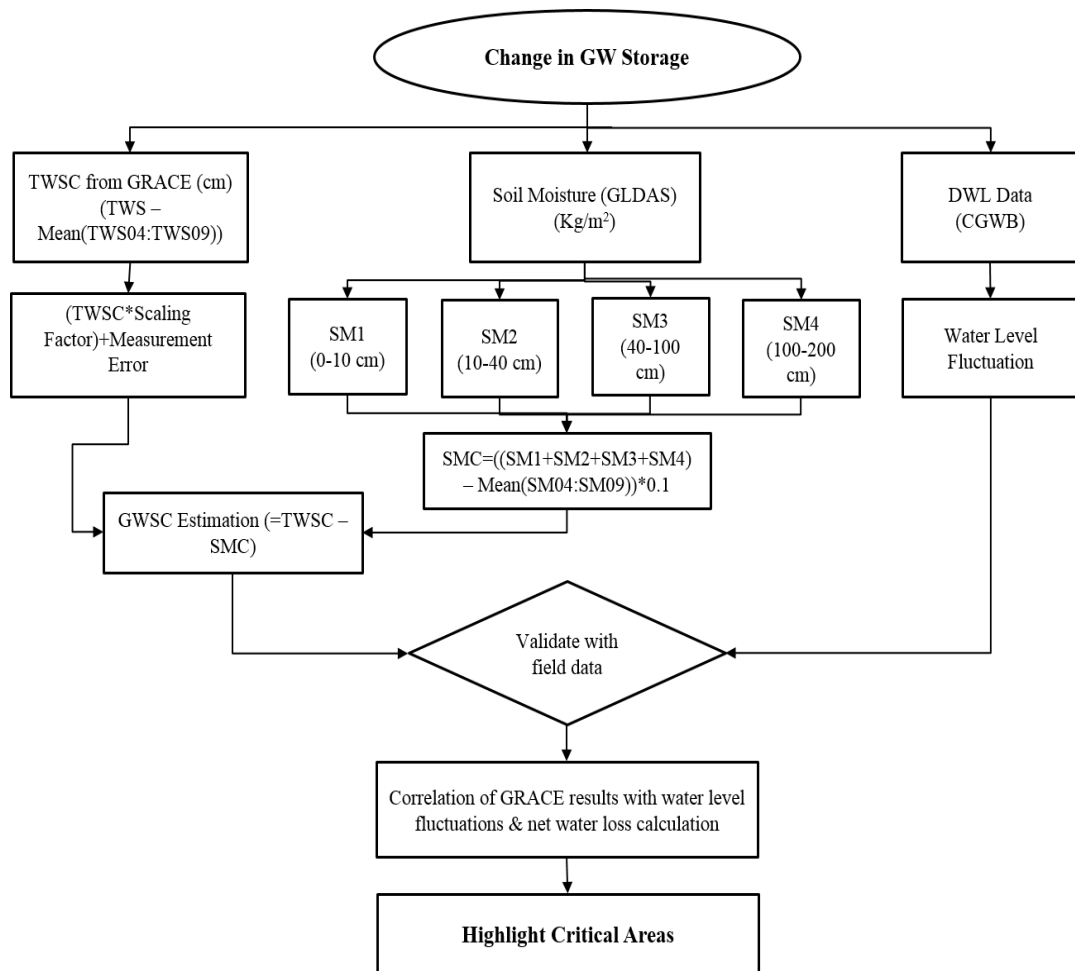


**Figure 4.2.** Flowchart showing Methodology for Ground Water Storage Change Estimation.

The RL05 land data product obtained from GRACE satellite are based on spherical harmonics from CSR, GFZ and JPL. The data product is filtered and processed for the geoid and is subtracted and is in the form of equivalent water thickness of terrestrial water storage (expressed in cm). The time mean of 2004-2009 has been removed. As the result of several samplings and post-processing of initial GRACE observations, the surface mass variations are attenuated. So, the first step is to apply the scaling coefficients to the GRACE Tellus land data to restore the energy attenuated by destripping, Gaussian and degree 60 filters.

The GRACE level 3 data is freely available on Jet Propulsion Laboratory, NASA website in ASCII as well as Netcdf format. The data for January, 2003 to December, 2012 was downloaded and the grids were extracted to TIFF format. The land grids were multiplied with

the scaling factor and leakage and measurement errors were taken into account. It was then masked for the study region i.e., the states of Rajasthan, Uttar Pradesh, Punjab, Haryana and Delhi. The ASCII files were imported to MS Excel and the database was created for monthly TWS change values for 10 years (2003-12). Each and every value was multiplied with the scaled factor. The monthly TWSC values were then interpolated in ArcGIS using Kernel smoothing and masked for the study region for 2003-2012.

The data for soil moisture was downloaded from GLDAS website. It is derived using GLDAS-2.0 NOAH Model. It is expressed in terms of  $\text{Kg/m}^2$ . Soil moisture is available in 4 layers. Each layer for different depth, i.e., first layer is for 0-10 cm, second layer for 10-40 cm, third layer for 40-100 cm and fourth layer for 100-200 cm. By summing up the soil moisture all the four layers, the volumetric soil moisture, the volumetric soil water content was obtained (as the density of water is known). The soil moisture data is in grid format and is freely available. The grids were downloaded and masked for the study region. Then all the grid files (monthly data) were stacked separately for all four layers of soil moisture. The spectral values for each pixel were imported to MS Excel and all four soil moisture quantities were added for every pixel, so that the volumetric soil moisture for every pixel was obtained. Then the time mean of 2004-2009 was removed from each value, similar to GRACE level 3 data. The total soil moisture (unit  $\text{Kg/m}^2$ ) was converted into centimeters so as to match the units with GRACE TWS, by using the fact that water is of unit density ( $1\text{g/cm}^3$ ). So the soil moisture values were multiplied by 0.1 to convert from  $\text{Kg/m}^2$  to cm (thickness of water column upto 2 m depth). The monthly final soil moisture values were then interpolated in ArcGIS using Gaussian function of Kernel smoothing and masked for the study region for 2003-2012 (fig. 4.3).

Monthly ground water storage change was calculated using Model Maker in ERDAS IMAGINE 13 by subtracting soil moisture layers from terrestrial water storage layers, shown in fig (4.4).

The maps for ground water storage change for pre-monsoon and post-monsoon for each year were prepared initially followed by the maps showing ground water storage change rate and mean over the decade 2003 to 2012.

Using the processed ASCII data for  $1^0 \times 1^0$  grid, initially the monthly time-series was plotted for Rajasthan, Uttar Pradesh, Punjab, Haryana and Delhi separately depicting the trend of total water storage, soil moisture, rainfall and groundwater storage change over a period of 10 years (2003 – 2012). The trend was observed very carefully and using the slope of ground water depletion trend and the area covered, the average volumetric ground water storage loss was calculated for separate states and then added for whole of the study region. An idea of decadal volumetric loss of ground water storage loss for the NW India was hence obtained.

The ground water storage change trend obtained by GRACE was compared with the ground water fluctuation trend by using depth to water level data (CGWB) for pre-monsoon and post monsoon for validation.

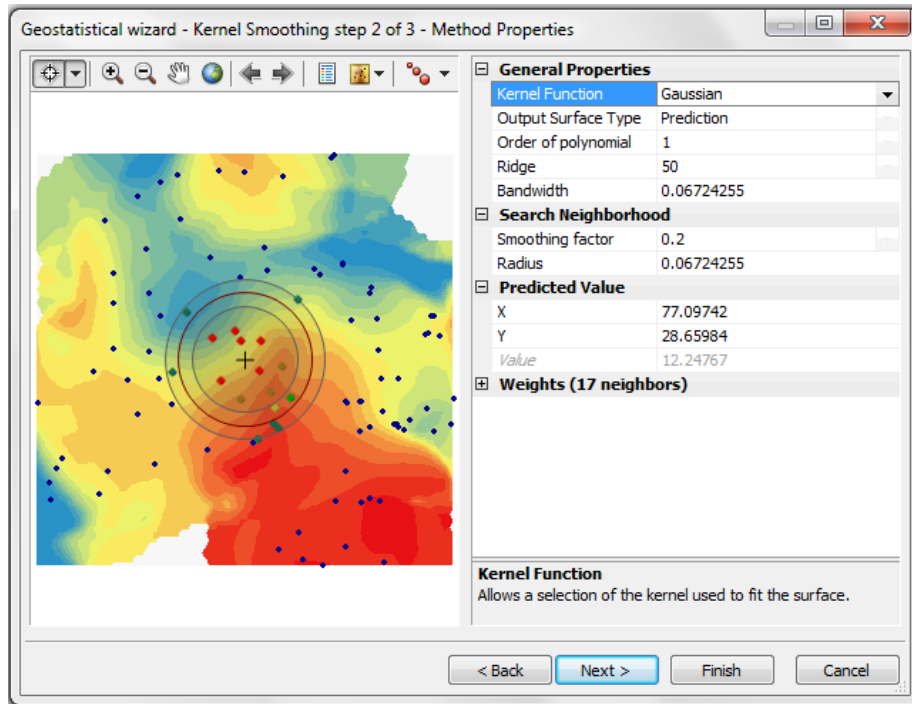


Figure 4.3. Interpolation using Gaussian function of Kernel smoothing in ArcGIS.

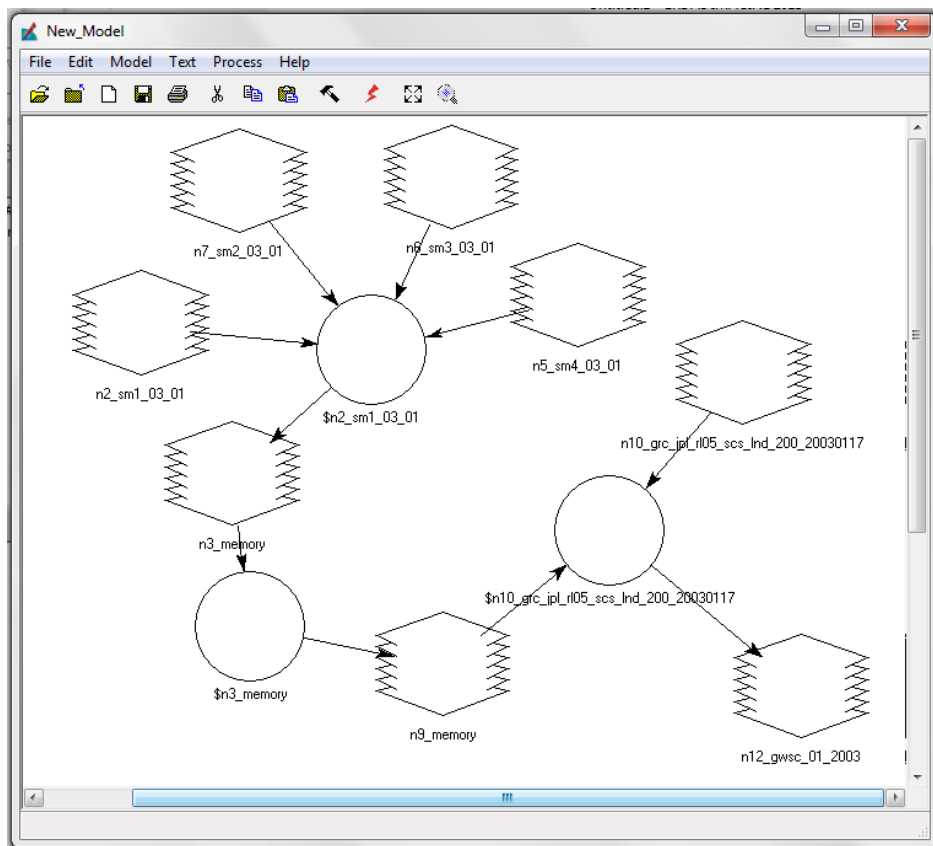


Figure 4.4. Model for ground water storage change calculation using soil moisture and twsc data for January, 2003.

#### 4.3.2. METHODOLOGY TO STUDY LAND SUBSIDENCE IN DELHI NCT USING DIFFERENTIAL INTERFEROMETRIC SAR TECHNIQUE:

Differential interferometry being the most effective space-borne geodetic technique has been widely used to study the phenomenon of surface deformation (i.e., land subsidence, tectonic movements, etc.) across the globe. The most prominent problem of land subsidence in plain area having little or very less tectonic activity is due to underground mining of natural resources, which may be coal, economic minerals or even ground water. In my study, the impact of ground water pumping leading to land subsidence, has been focussed.

The data used for DInSAR processing were from ALOS PALSAR (L-Band, FBS Mode, Level 1.1, ascending) and RADARSAT-2 (C-Band, ascending) for Delhi area. Both data were processed using SARSCAPE module of ENVI 5.0. SRTM DEM having 90 m spatial resolution was used to prepare the simulated interferogram. The processing steps for both the ALOS PALSAR and RADARSAT-2 data are same. The flowchart showing the steps involved in DInSAR processing is shown in fig (4.5).

The first step involved importing the datasets into SLC (Single Look Complex) format by using the parameters from leader file. Secondly, the imported SLC files were multilooked and the power image was generated, it is also known as amplitude image. Then the SRTM DEM Version 4 was extracted for the area covered by the reference frame by providing the SLC file. The DEM was used for flattening and removal of topographic error from the interferograms.

The interferometric pairs were made using the information on acquisition date. The image with older date being the master and recent would be the slave image. Baseline was estimated providing us the information on temporal, perpendicular and critical perpendicular baseline, Doppler centroid difference and critical centroid difference and height of ambiguity. The pairs for further processing were selected based on the baseline information. Pairs with higher perpendicular baseline were not considered for further processing because of increased scope of noise in the anticipated interferogram.

Four pairs were selected out of six for interferogram generation, from ALOS PALSAR data pairs for further processing. Similarly, based on same criteria, from RADARSAT-2 data pairs, two pairs out of four were considered.

**Table 4.5.** Specifications of data pairs generated from ALOS PALSAR data:

Data pair	Date 1	Date 2	Baseline(m)			Doppler		Ambiguity height (m)	Coherence
			Temporal (days)	Perpendicular	Critical	Centroid diff.	Critical		
20548-21219	02-12-2009	17-01-2010	46	361.596	13059	9.116	2159.827	177.194	0.44
20548-21890	02-12-2009	04-03-2010	92	755.926	13059	-15.61	2159.827	84.761	0.319

20548-26587	02-12-2009	20-01-2011	413.997	1831.372	13059	-10.569	2159.827	34.986	0.22
21219-21890	17-01-2010	04-03-2010	46	530.988	13055	-24.726	2159.827	120.648	0.458
21219-26587	17-01-2010	20-01-2011	367.997	1513.517	13055	-19.685	2159.827	42.327	0.659
21890-26587	04-03-2010	20-01-2011	321.997	1113.558	13057	5.04	2159.827	57.536	0.23

**Table 4.6.** Specifications of data pairs generated from ALOS PALSAR data:

Data pair	Date 1	Date 2	Baseline(m)			Doppler		Ambiguity height (m)	Coherence
			Temporal (days)	Perpendicular	Critical	Centroid diff.	Critical		
455005-455006	03-12-2013	20-01-2014	48	55.52	1151.5	-10.235	1362.14	6.63	0.26
455005-455007	03-12-2009	09-03-2014	96	282.23	1151.5	58.236	1362.14	8.19	0.25

The specifications of the data pairs for ALOS PALSAR and RADARSAT-2 data pairs have been presented in table (4.5) and (4.6).

The interferograms were generated using the multi-step interferometric workflow. The interferograms were then filtered using Boxcar filtering algorithm and coherence images was generated. The pairs having minimum coherence of 0.3 were considered, although in some cases the pairs having lower coherence were also considered in which fringes were observed, the coherence in fringe area came out to be satisfactory. The filtered interferograms were then geo-coded for further analysis.

The fringe analysis was performed over the geocoded filtered interferograms. A single colour cycle within a deformation fringe represents the displacement of  $\lambda/2$  in the vertical direction, where  $\lambda$  wavelength of microwave band. Since ALOS PALSAR utilises L-band of microwave having wavelength of 23.6 cm, therefore each colour cycle in the interferogram represents a Line of sight (LOS) displacement of 11.8 cm. And for RADARSAT-2 utilizing C-band having wavelength of 5.6 cm, each colour cycle represents a LOS displacement of 5.6 cm. The total displacement was calculated by using following relation,

$$\Delta\rho = \left(\frac{n}{N}\right) \cdot \frac{\lambda}{2} \quad (4.2)$$

Where,  $\Delta\rho$  represents the LOS displacement, n represents the number of colours present in the fringe, N represents total number of colour in a cycle (8 for ALOS PALSAR and 7 for RADARSAT-2). The analysis results are tabulated in Table (5.2) and (5.3).

#### **Extensive Processing for Delineated of the Area of Interest:**

The area covered by fringes was our new region of interest and hence the ALOS PALSAR and RADARSAT-2 scenes were subsetting according to the spatial extent of the area covered by each fringe. The interferometric processing (fig. 4.5) and filtering (fig. 4.6) were applied and coherence image was generated for each fringe in every relevant interferometric pair.

This was followed by the process of phase unwrapping by using minimum cost flow algorithm, the process is illustrated in fig. (4.6).

LOS deformation rate for the fringes were calculated using the absolute phase information, as shown in equation 4.4.

#### **Determination of LOS Displacement using Absolute Phase Component in D-InSAR Technique:**

Surface displacement was estimated in terms of phase difference ( $\Delta\phi$ ) after normalization of the phase value from the second interferogram with respect to the baseline of the first interferogram as,

$$\Delta\phi = \phi' - \frac{B'_{\parallel}}{B_{\parallel}} \cdot \phi \quad (4.3)$$

Where,  $\phi'$  and  $\phi$  are phase values of two interferograms, and  $B'_{\parallel}$  and  $B_{\parallel}$  are parallel components of the baselines (parallel to the line of sight) of the corresponding interferograms. The component of surface displacement along the line-of-sight ( $\Delta\rho$ ) can be calculated using the following mathematical relation as,

$$\Delta\phi = \frac{4\pi}{\lambda} \cdot \Delta\rho$$

Or, 
$$\Delta\rho = \frac{\Delta\phi \cdot \frac{\lambda}{2}}{2\pi} \quad (4.4)$$

The LOS displacement rate for fringes as well as background was calculated for all the fringes of ALOS PALSAR and RADARSAT-2 data pairs. The results are tabulated in table (5.4) and (5.5).

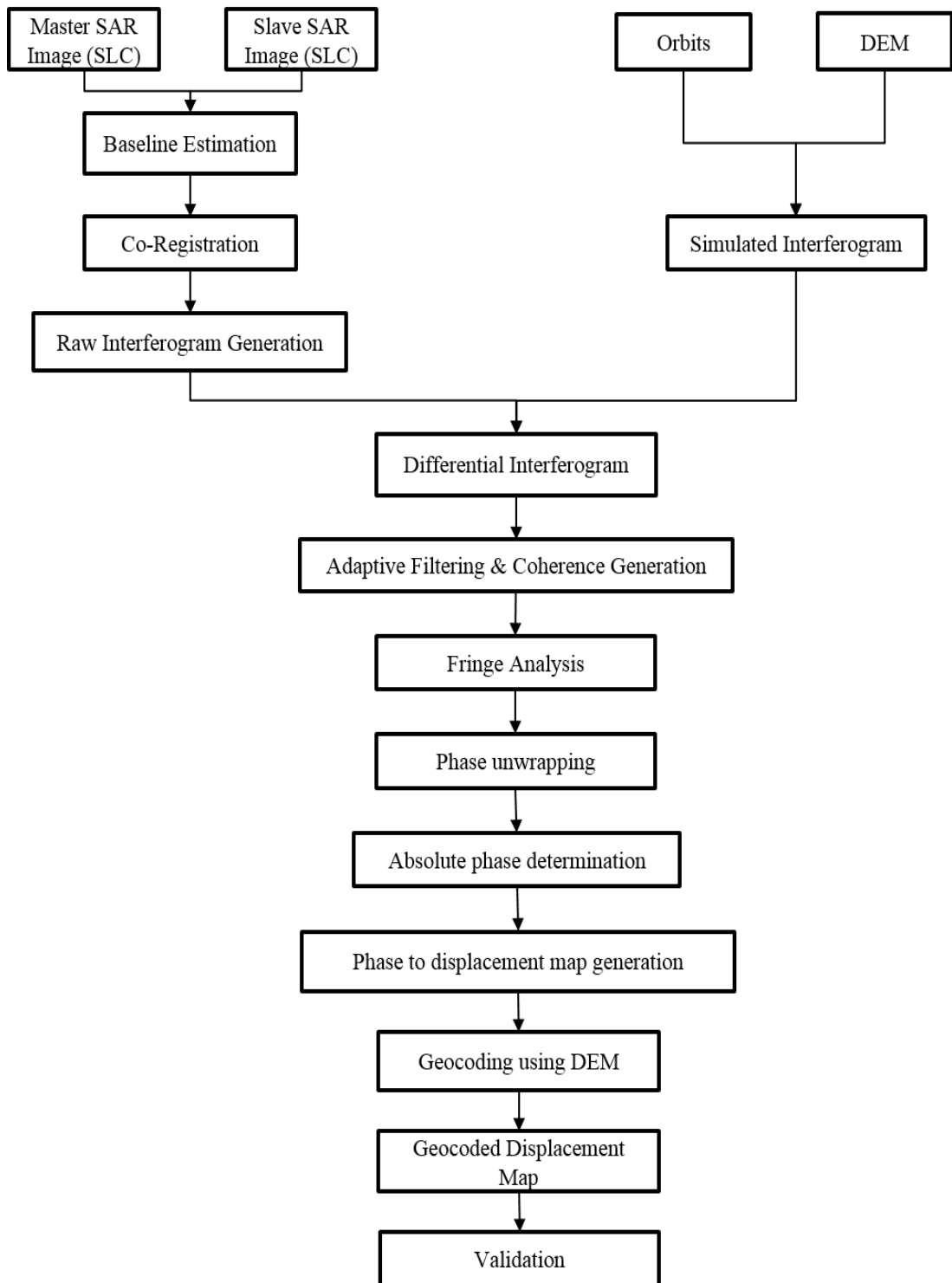


**Figure 4.5.** Flowchart showing Methodology to study land subsidence using Differential Interferometric SAR technique.

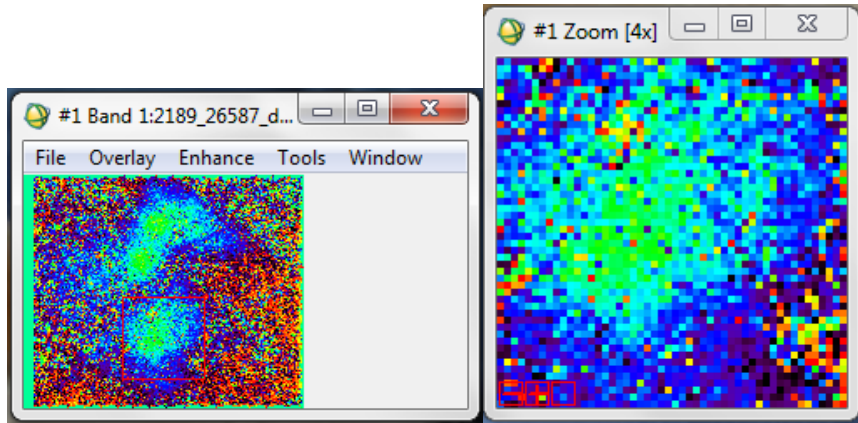


**Figure 4.6.** Differential interferogram of Dwarka area of Delhi NCT for temporal baseline of 322 days.

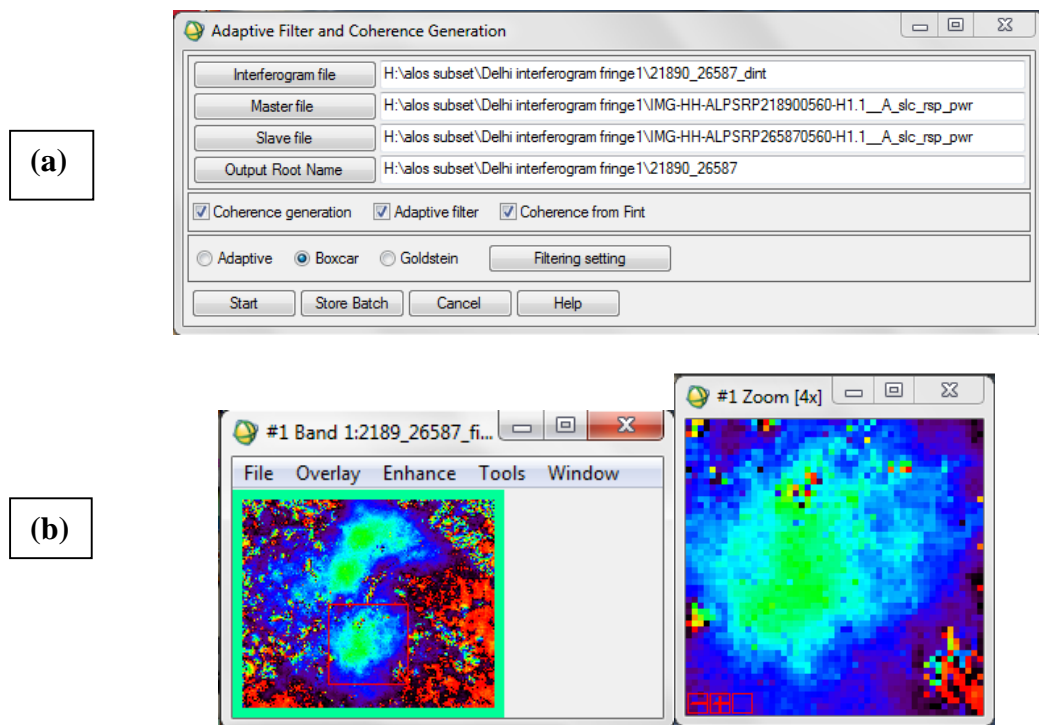


**Figure 4.7.** (a) Interferogram filtering using boxcar filtering in SARscape module of ENVI 5.0; (b) Filtered interferogram of Dwarka area of Delhi NCT, having coherence of 0.3.

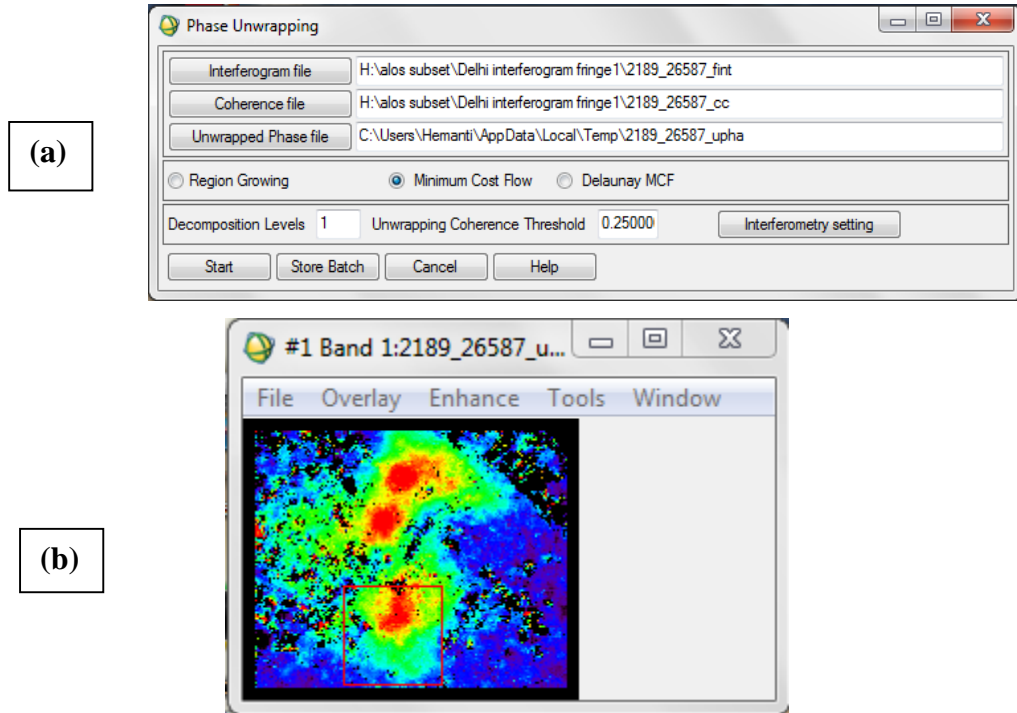


**Figure 4.8.** (a) Phase unwrapping using minimum cost flow algorithm in SARscape module of ENVI 5.0; (b) Unwrapped phase interferogram of Dwarka area of Delhi NCT.

This followed the three stages of estimating deformation rate Viz.,

- (i) Time-weighted subsidence rate
- (ii) Coherence weighted subsidence rate
- (iii) Linear regression

#### **Time-weighted subsidence rate:**

The time weighted subsidence rate involved the calculation of subsidence rate for every fringe with respect to the temporal baseline ( $\Delta T$ ). The time-weighted subsidence rate was calculated using the following equation for both the fringes for both ALOS PALSAR and RADARSAT-2 data pairs.

$$R_T = \frac{(R_1 \times \Delta T_1) + (R_2 \times \Delta T_2)}{\Delta T_1 + \Delta T_2} \quad (4.6)$$

Where,  $R_T$  is time weighted subsidence rate for two DInSAR fringes;  $R_1$  and  $R_2$  are the LOS displacement using absolute phase component for fringe 1 and 2 respectively; and  $T_1$  and  $T_2$  are temporal baselines for data pair 1 and 2 respectively.

**Coherence weighted subsidence rate:**

The time weighted subsidence rate involved the calculation of subsidence rate for every fringe with respect to the coherence for every data pair. It was calculated using the equation (4.7) for both ALOS PALSAR and RADARSAT-2 data pairs.

$$R_{C12} = \frac{(R_{12} \times C_{13}) + (R_{13} \times C_{12})}{C_{12} + C_{13}} \quad (4.6)$$

Where,  $R_{C12}$  is coherence weighted subsidence rate for two DInSAR fringes;  $R_{12}$  and  $R_{13}$  are the LOS displacement using absolute phase component for fringe 1 and 2 respectively; and  $C_{12}$  and  $C_{13}$  are temporal baselines for data pair 1 and 3 respectively.

## 5. RESULTS & DISCUSSIONS

### 5.1. GROUND WATER STORAGE CHANGE ESTIMATION FOR NW INDIA USING GRACE DATA:

The ground water storage change was estimated using the rescaled GRACE TWSC data and soil moisture data from GLDAS. The results so obtained have been shown below.

Various maps were prepared to visualize the status of ground water regime in NW India using the rescaled GRACE JPL level 3 ASCII data and GLDAS soil moisture both having spatial resolution of  $1^\circ \times 1^\circ$ .

The maps for terrestrial water storage change rate and ground water storage change rate map depicts that maximum depletion has been occurring in northern part of Uttar Pradesh, Delhi NCT, Haryana and parts of Rajasthan and Punjab. Maximum depletion can be observed in the state of Haryana and Delhi.

Decadal fluctuation for pre-monsoon, monsoon and post monsoon were also mapped and showed a negative trend across the eastern border of Uttar Pradesh with maximum depletion in north UP, Delhi, Haryana and Punjab.

The deviation of groundwater storage in pre-monsoon and post-monsoon with respect to decadal mean also show the same trend as above.

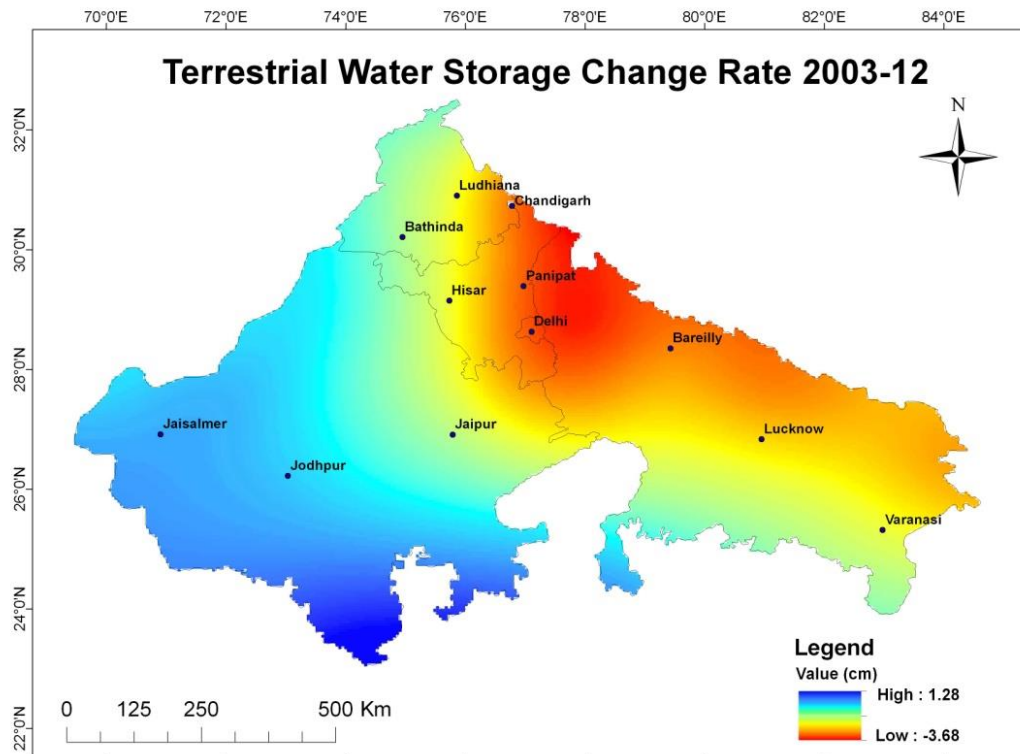


**Figure 5.1.** Terrestrial water storage change rate for the decade 2003-12 for NW India.

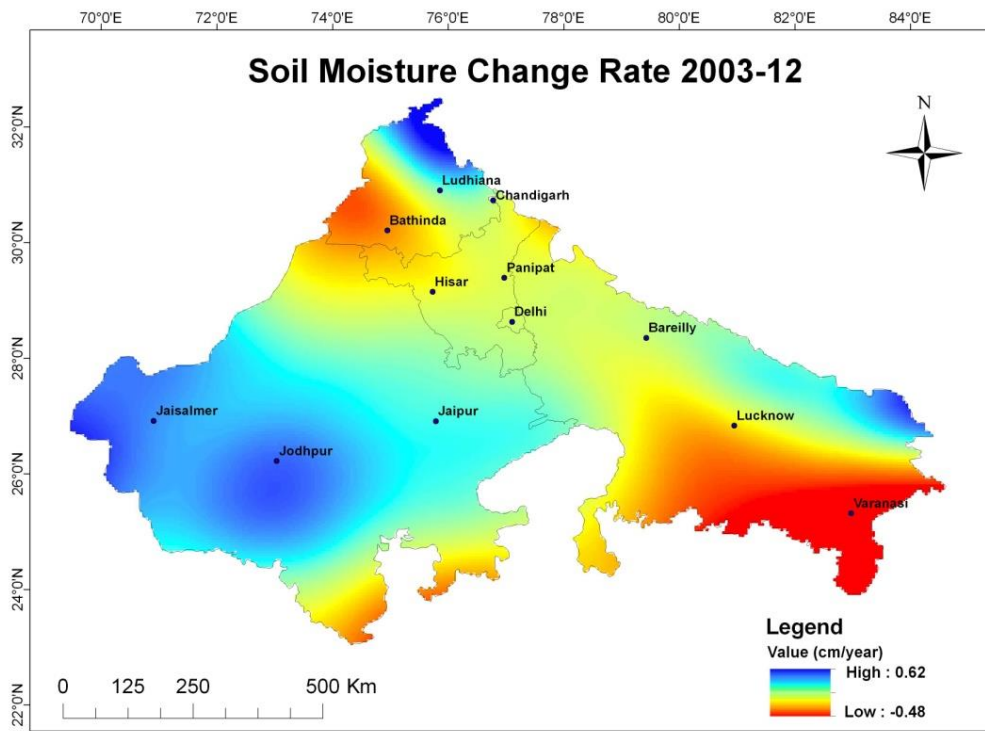


**Figure 5.2.** Soil moisture change rate for the decade 2003-12 for NW India.

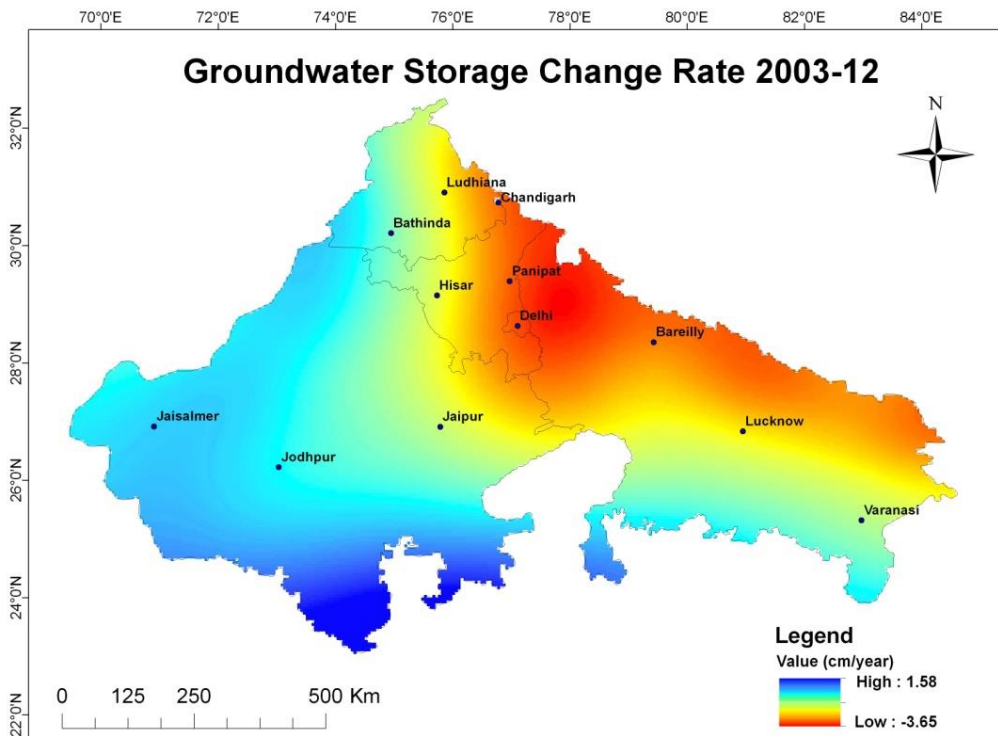


**Figure 5.3.** Ground water storage change rate estimated from TWSC and SMC for the decade 2003-12 for NW India.

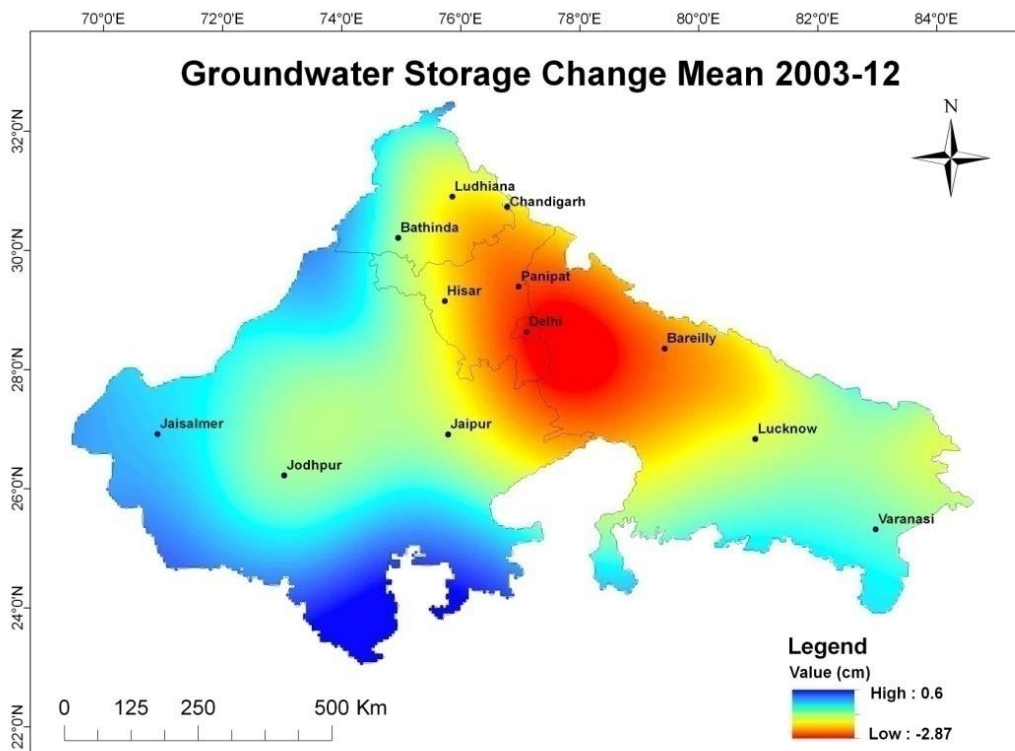


**Figure 5.4.** Ground water storage change mean for the decade 2003-12 for NW India.

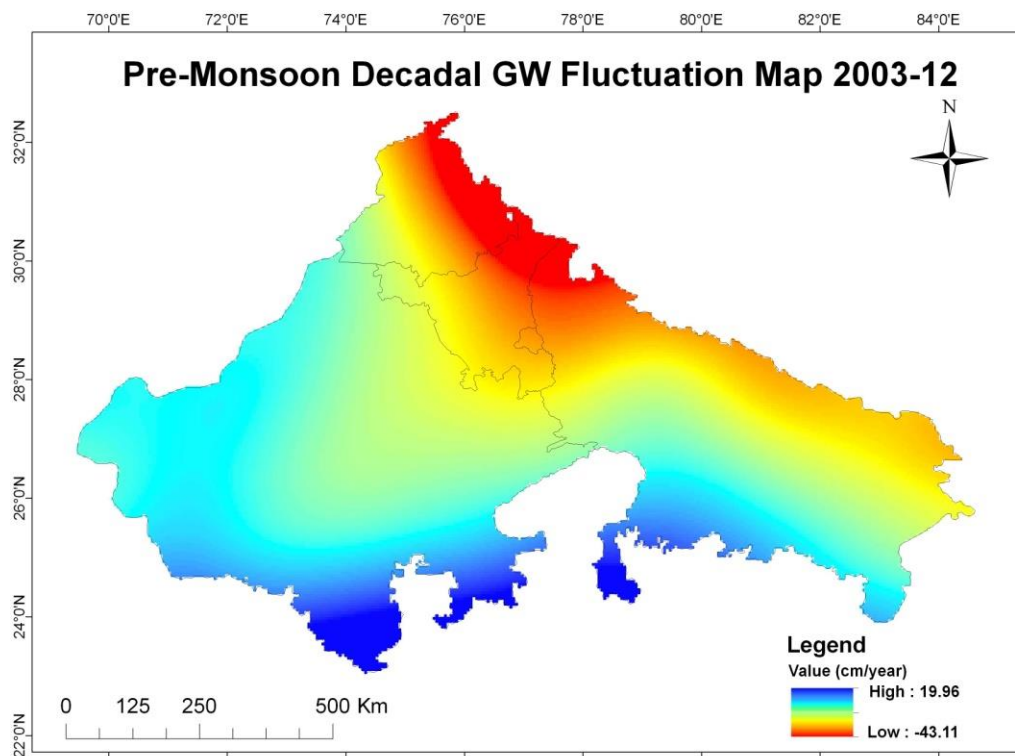


**Figure 5.5.** Pre-Monsoon decadal ground water fluctuation map for 2003-12 for NW India.

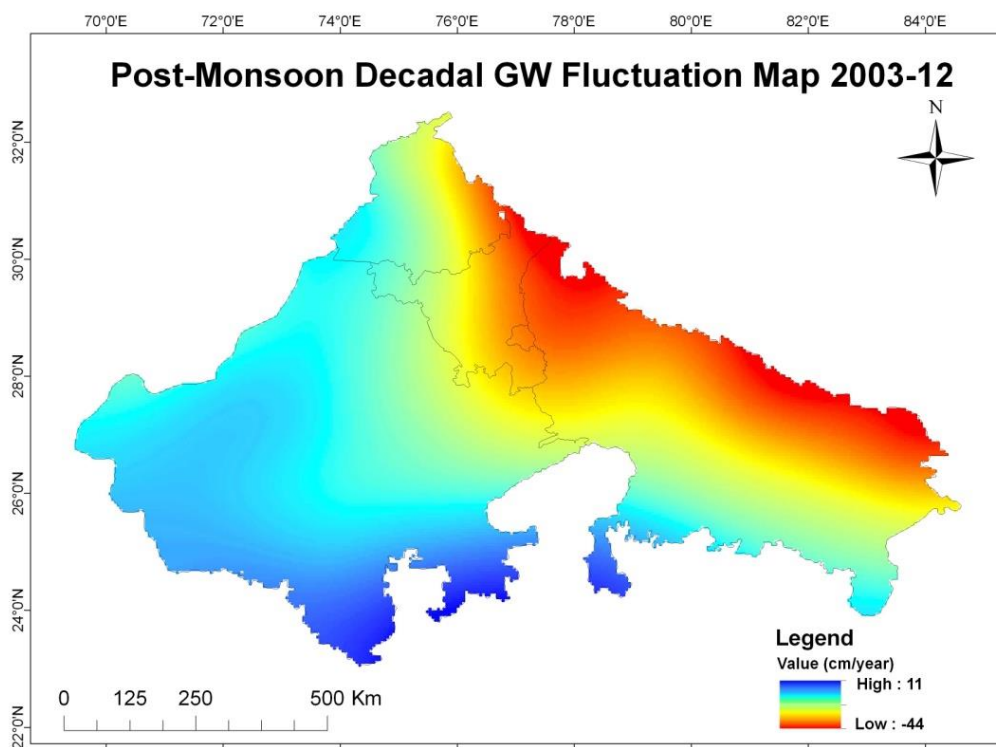


**Figure 5.6.** Post-Monsoon decadal ground water fluctuation map for 2003-12 for NW India.

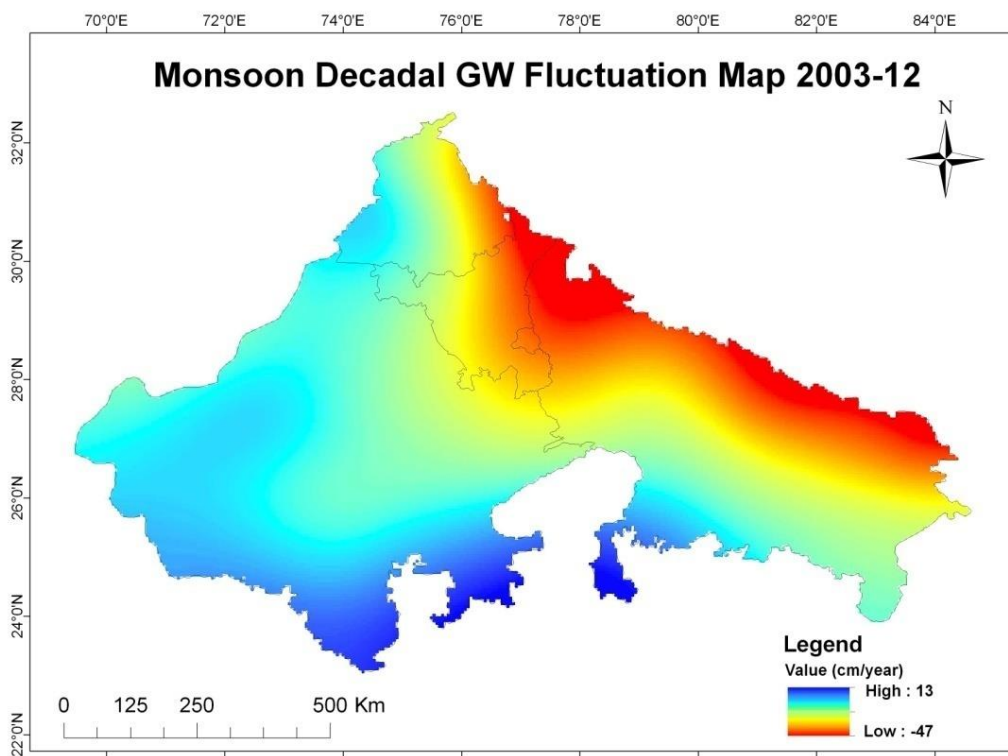


**Figure 5.7.** Monsoon decadal ground water fluctuation map for 2003-12 for NW India.

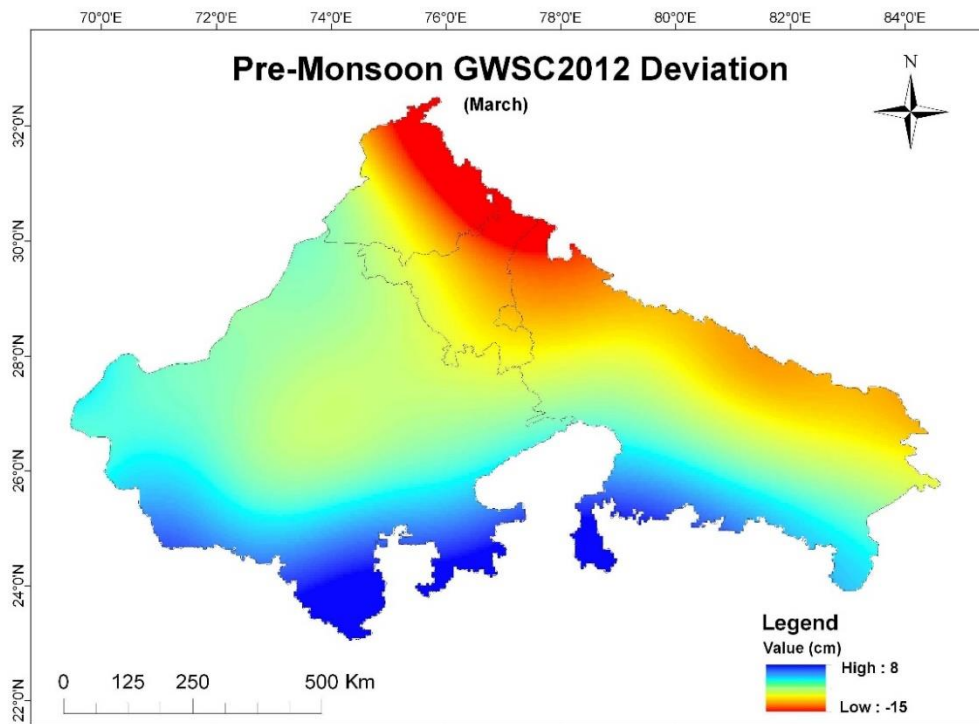


**Figure 5.8.** Map showing deviation Pre-Monsoon ground water change from decadal (2003-12) mean for NW India.

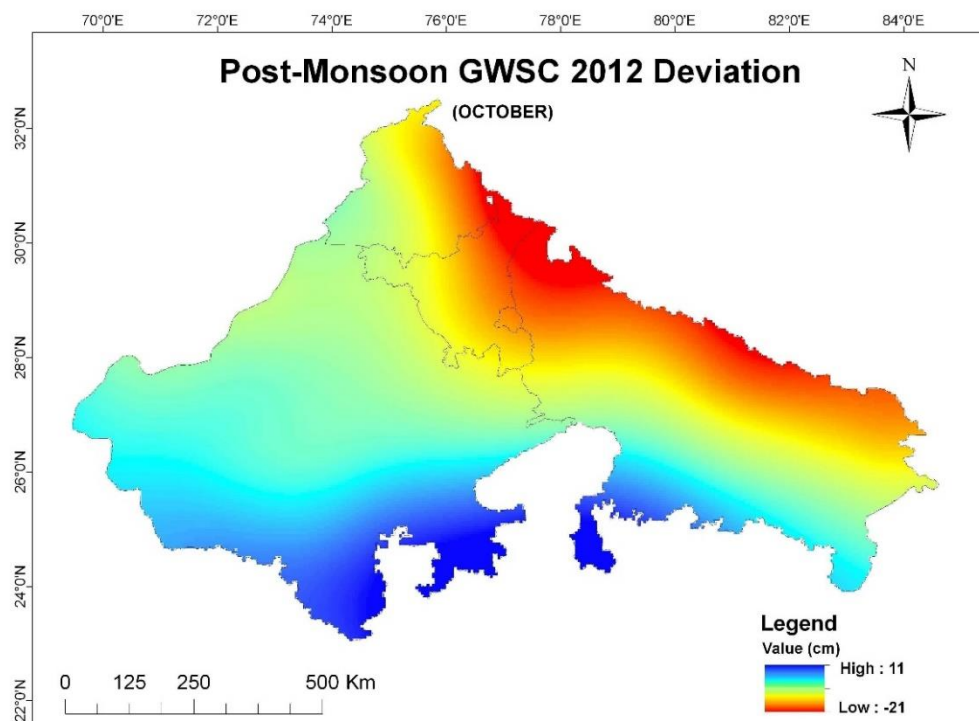


**Figure 5.9.** Map showing deviation Post-Monsoon ground water change from decadal (2003-12) mean for NW India.

The time-series showing the trend of terrestrial water storage change, soil moisture change, rainfall anomaly and ground water change over the decade of 2003-12 were prepared for North-West India including the states of Rajasthan, Uttar Pradesh, Punjab, Haryana and Delhi. These are shown below.

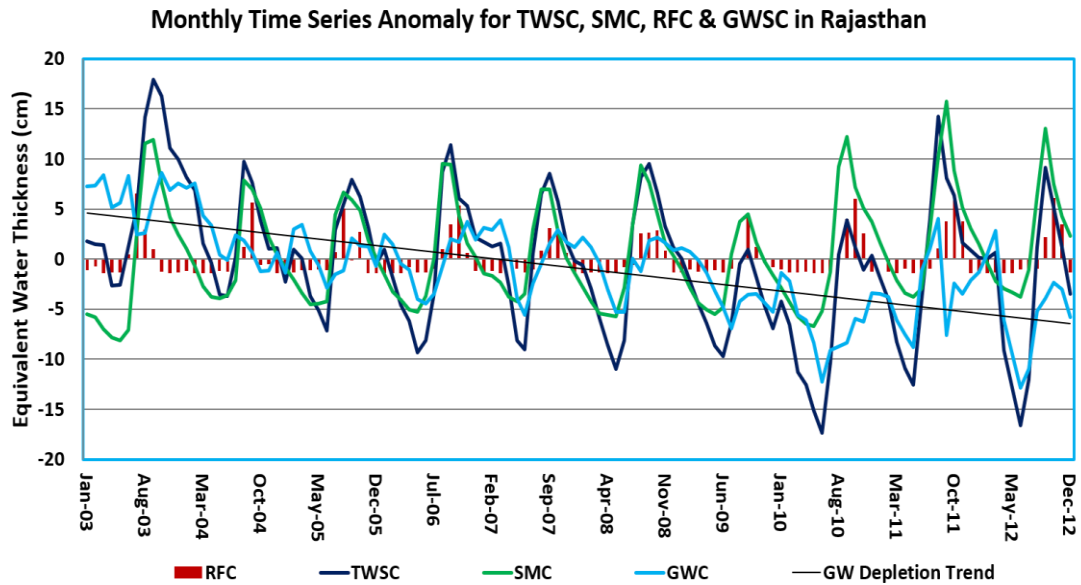


**Figure 5.10.** Time series analysis for four hydrological parameters (Terrestrial water storage change (TWSC), Ground water change (GWC), Rainfall change (RFC) and Soil Moisture change (SMC)) in Rajasthan from Jan 2003- Dec 2012.

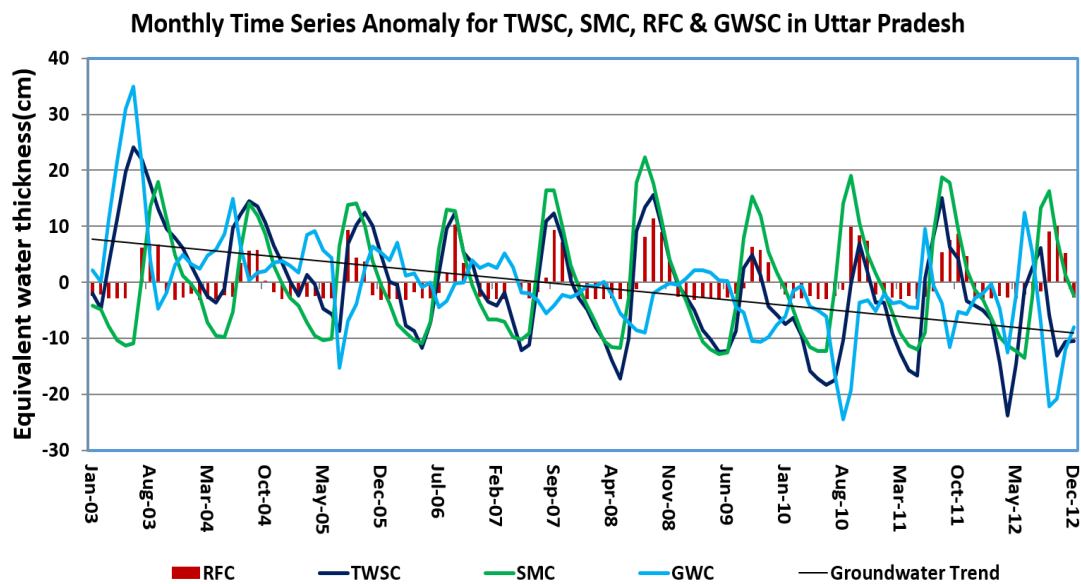


**Figure 5.11.** Time series analysis for four hydrological parameters (Terrestrial water storage change (TWSC), Ground water change (GWC), Rainfall change (RFC) and Soil Moisture change (SMC)) in Uttar Pradesh from Jan 2003- Dec 2012.

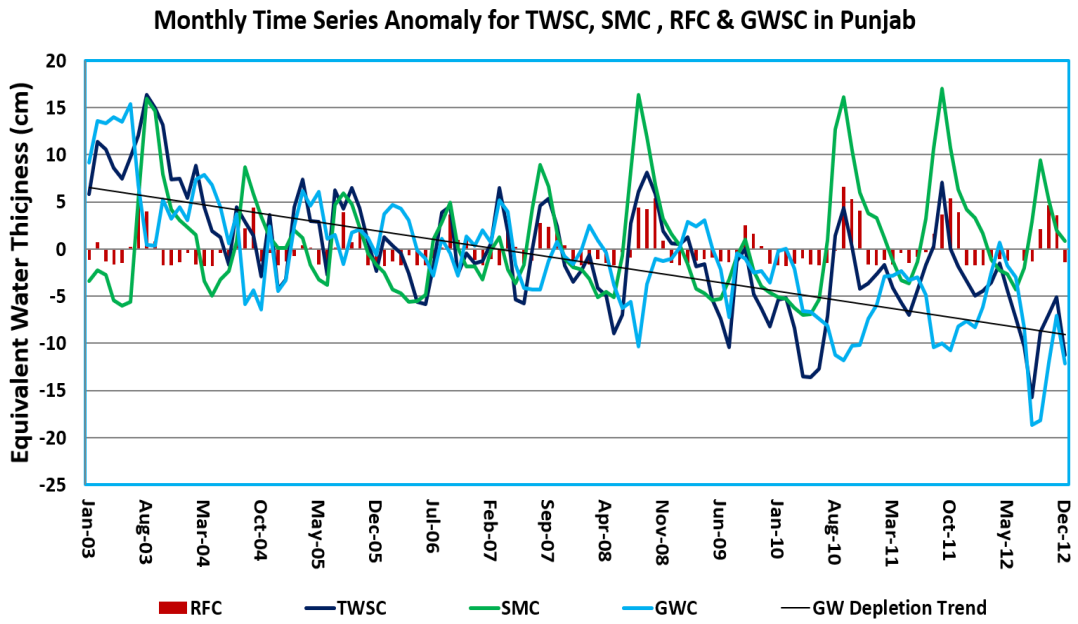


**Figure 5.12.** Time series analysis for four hydrological parameters (Terrestrial water storage change (TWSC), Ground water change (GWC), Rainfall change (RFC) and Soil Moisture change (SMC)) in Punjab from Jan 2003- Dec 2012.

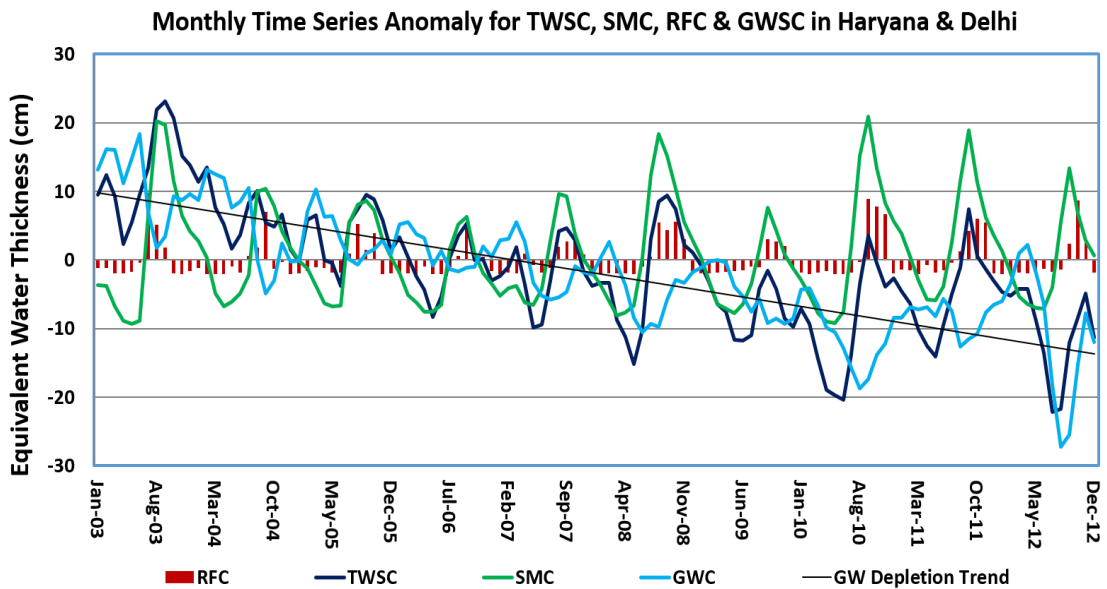


**Figure 5.13.** Time series analysis for four hydrological parameters (Terrestrial water storage change (TWSC), Ground water change (GWC), Rainfall change (RFC) and Soil Moisture change (SMC)) in Haryana & Delhi from Jan 2003- Dec 2012.

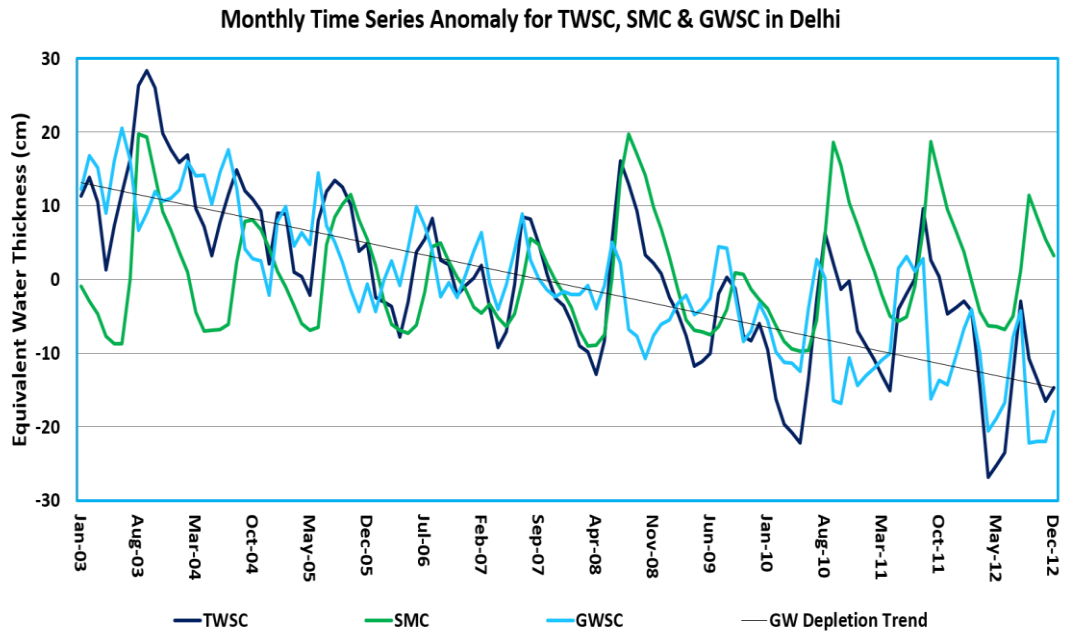


**Figure 5.14.** Time series analysis for four hydrological parameters (Terrestrial water storage change (TWSC), Ground water change (GWC), Rainfall change (RFC) and Soil Moisture change (SMC)) in Delhi pixel from Jan 2003- Dec 2012.

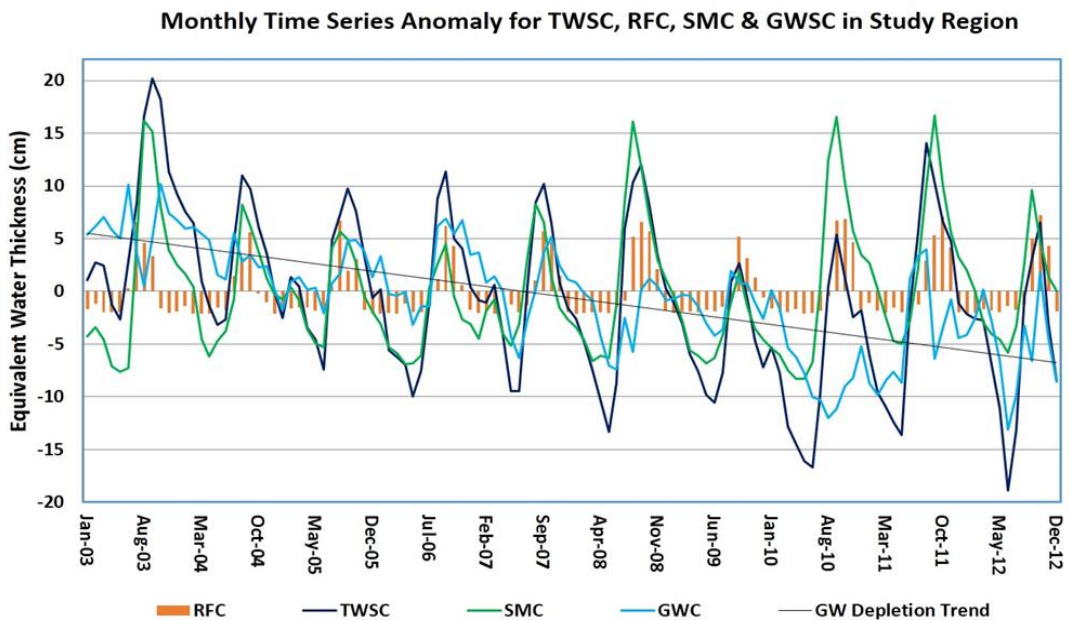


**Figure 5.15.** Time series analysis for four hydrological parameters (Terrestrial water storage change (TWSC), Ground water change (GWC), Rainfall change (RFC) and Soil Moisture change (SMC)) in study region from Jan 2003- Dec 2012.

The ground water fluctuation obtained from GRACE was hence validated from the ground water fluctuation estimated from the depth to water level data collected from Central Ground Water Board, Delhi, for Delhi pixel for both pre-monsoon and post monsoon. A satisfactory correlation was obtained. The correlation results are given below in fig (5.16) and (5.17).

**Correlation of Pre-Monsoon GWL Fluctuation from GRACE derived results and Water Level Data for Delhi (2003-12)**

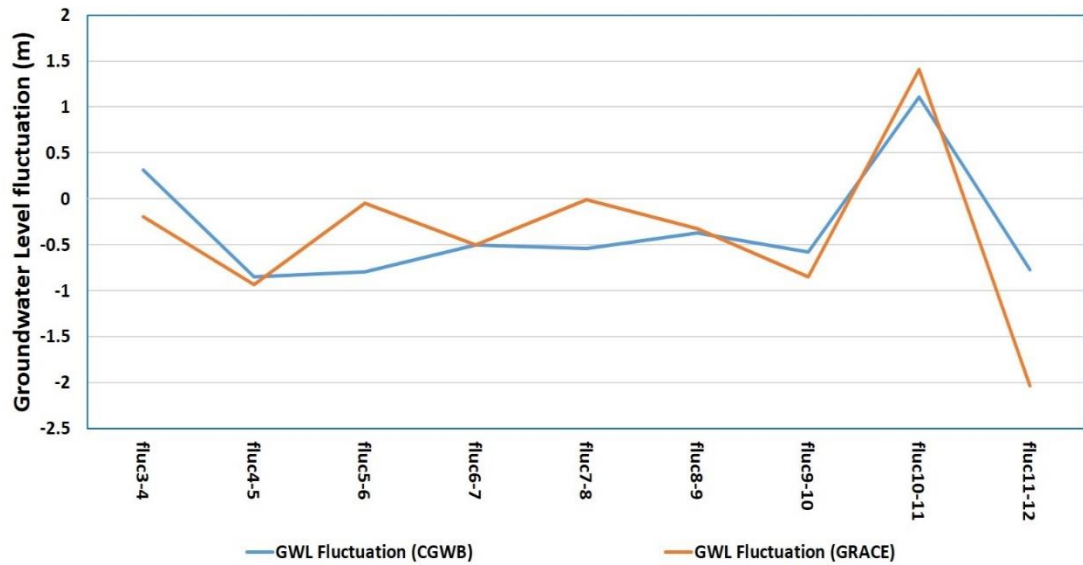


**Figure 5.16.** Correlation of Pre-Monsoon groundwater fluctuation derived from GRACE results and Groundwater level data for Delhi pixel for 2003-12.

**Correlation of Post-Monsoon GWL Fluctuation from GRACE derived results and Water Level Data for Delhi (2003-12)**

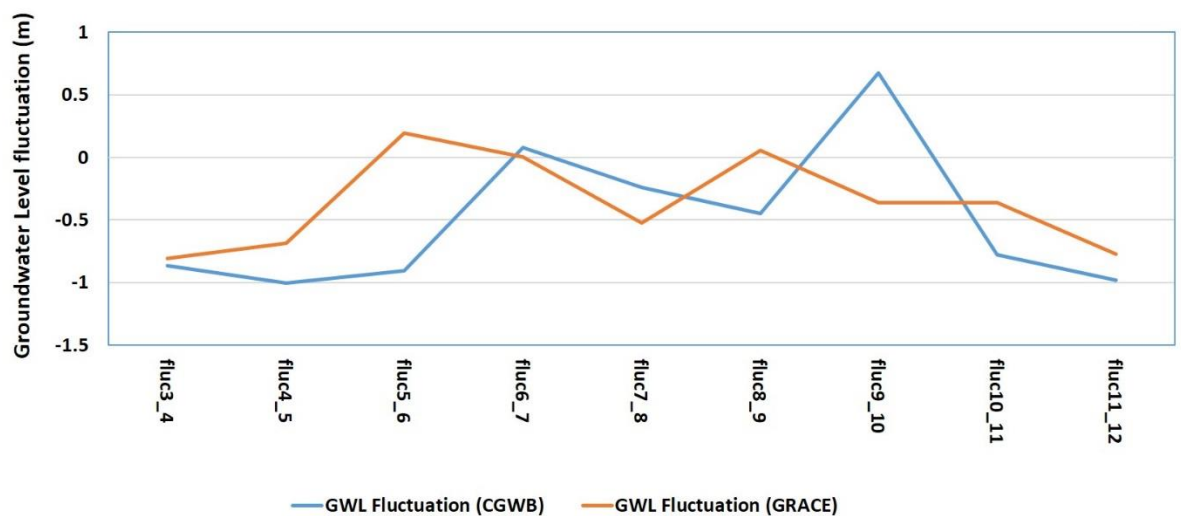


**Figure 5.17.** Correlation of Post-Monsoon groundwater fluctuation derived from GRACE results and Groundwater level data for Delhi pixel for 2003-12.

In pre-monsoon both GRACE ground water level fluctuation and DWL (depth to water level) fluctuation show a rise in 2010-11 and sharp fall for 2011-12. For post-monsoon, the correlation quite satisfactory.

The decadal volumetric ground water loss was calculated using the surface area covered by the states of NW India and the average yearly ground water depletion rate. The results are tabulated below in table (5.1).

**Table 5.1.** Volumetric Ground Water Loss in NW India for 2003-12.

S.N.	State	Area km <sup>2</sup>	Water loss rate in cm/year	Volumetric Water loss rate in km <sup>3</sup> /year	Net water loss in 10 years (km <sup>3</sup> )
1	Uttar Pradesh	295582.41	1.641±0.77	4.8505±2.27	48.51±4.88
2	Rajasthan	342610.88	1.11±0.42	3.8030±1.43	38.03±5.20
3	Haryana & Delhi	45415.97	2.29±0.72	1.0400±0.32	10.40±0.73
4	Punjab	51037.72	1.51±0.65	0.7707±0.33	7.71±0.83
	Total	734646.98			<b>104.65±11.64</b>

**GRACE Derived Net Ground Water Loss (Km<sup>3</sup>)  
In 10 Years for Study Area (2003-12)**

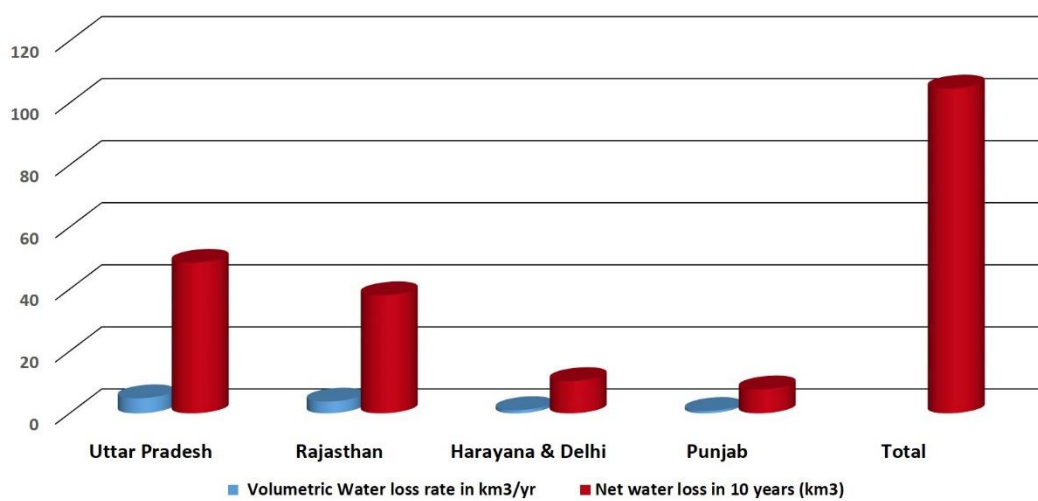


**Figure 5.18.** GRACE derived volumetric water loss rate and net water loss in 10 years expressed in Km<sup>3</sup>/year and Km<sup>3</sup> respectively.

The maximum ground water loss rate was observed in Haryana & Delhi i.e.,  $2.29 \pm 0.72$  cm/year followed by Uttar Pradesh having depletion rate of  $1.641 \pm 0.77$  cm/year. This is because of larger surface area covered by UP. This calls for extensive study in the most vulnerable area of Uttar Pradesh, Haryana and the National Capital Territory of Delhi.

## 5.2. LAND SUBSIDENCE STUDY IN DELHI NCT USING DIFFERENTIAL INTERFEROMETRIC SAR TECHNIQUE:

Land subsidence was studied in Delhi using DInSAR technique. As discussed earlier, the data used were procured by ALOS PALSAR (L-band) and RADARSAT-3. The results from both the datasets showed same area going through land subsidence. The area in which fringes were observed was in highly developing locality of Dwarka (South-West Delhi) and the other one was found in Udyog Vihar locality of Gurgaon-Delhi border.

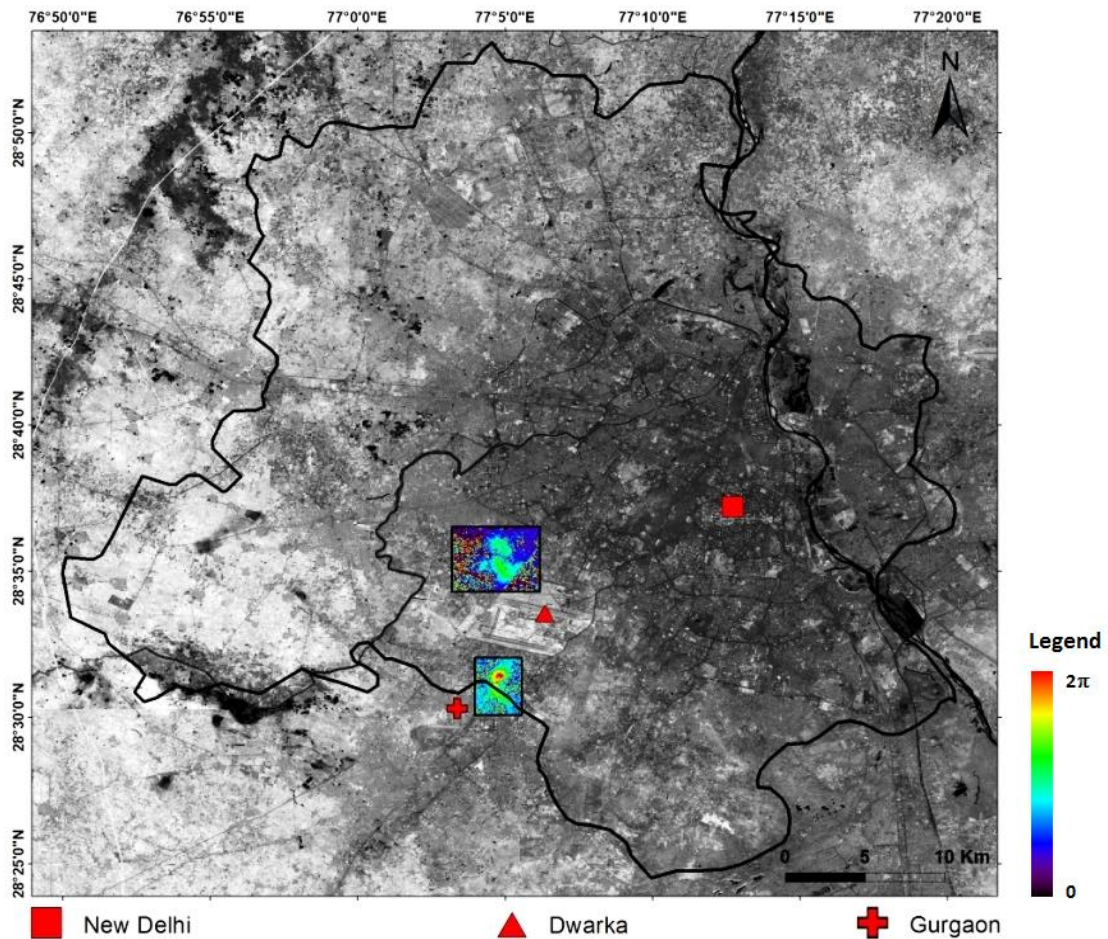


**Figure 5.19.** Interferogram showing land subsidence in Dwarka and Gurgaon area.

The interferograms so obtained for L-band ALOS PALSAR data sets are shown below. The temporal baseline varies from 92 days to 414 days.

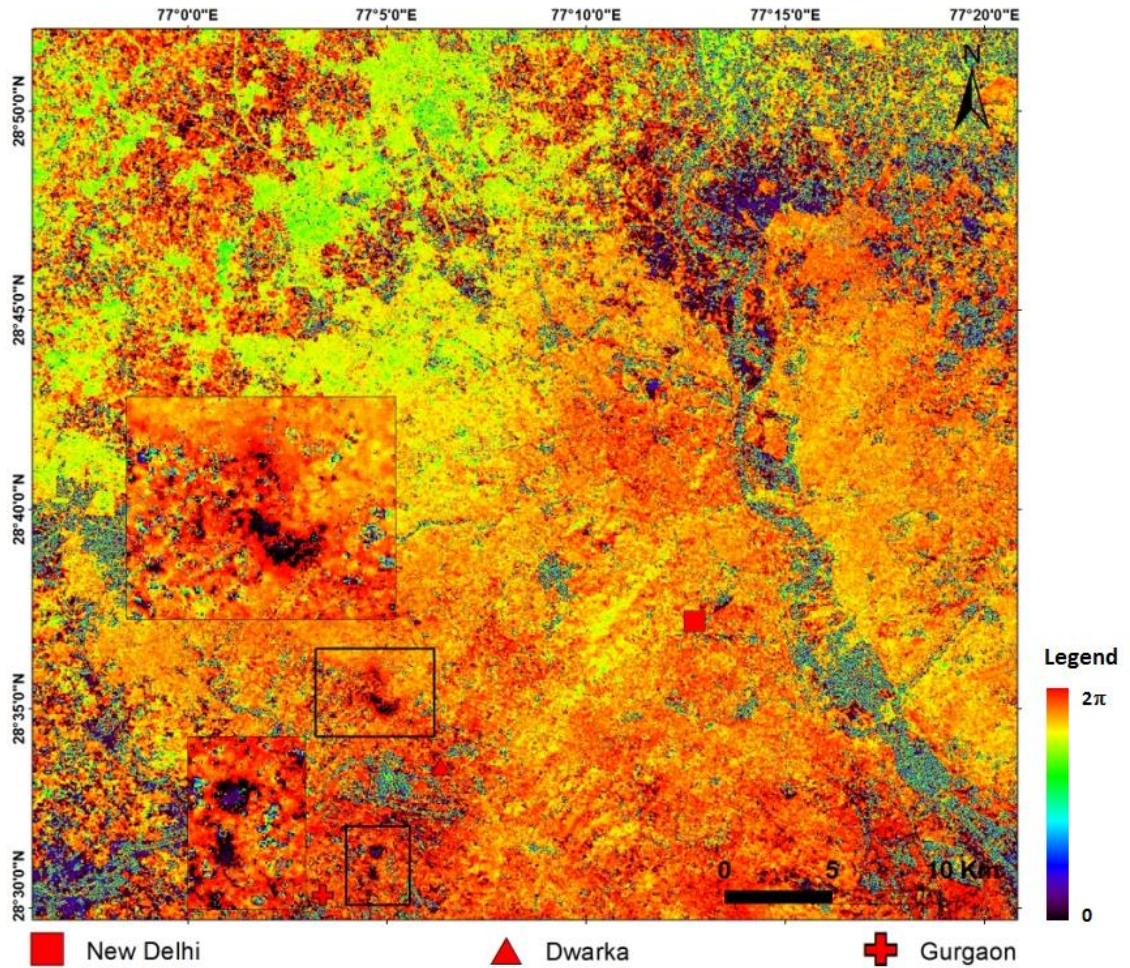


**Figure 5.20.** Interferogram showing land subsidence in Dwarka and Gurgaon area. Temporal baseline 92 days (2/12/2009 – 03/04/2010) and having average coherence of 0.32.

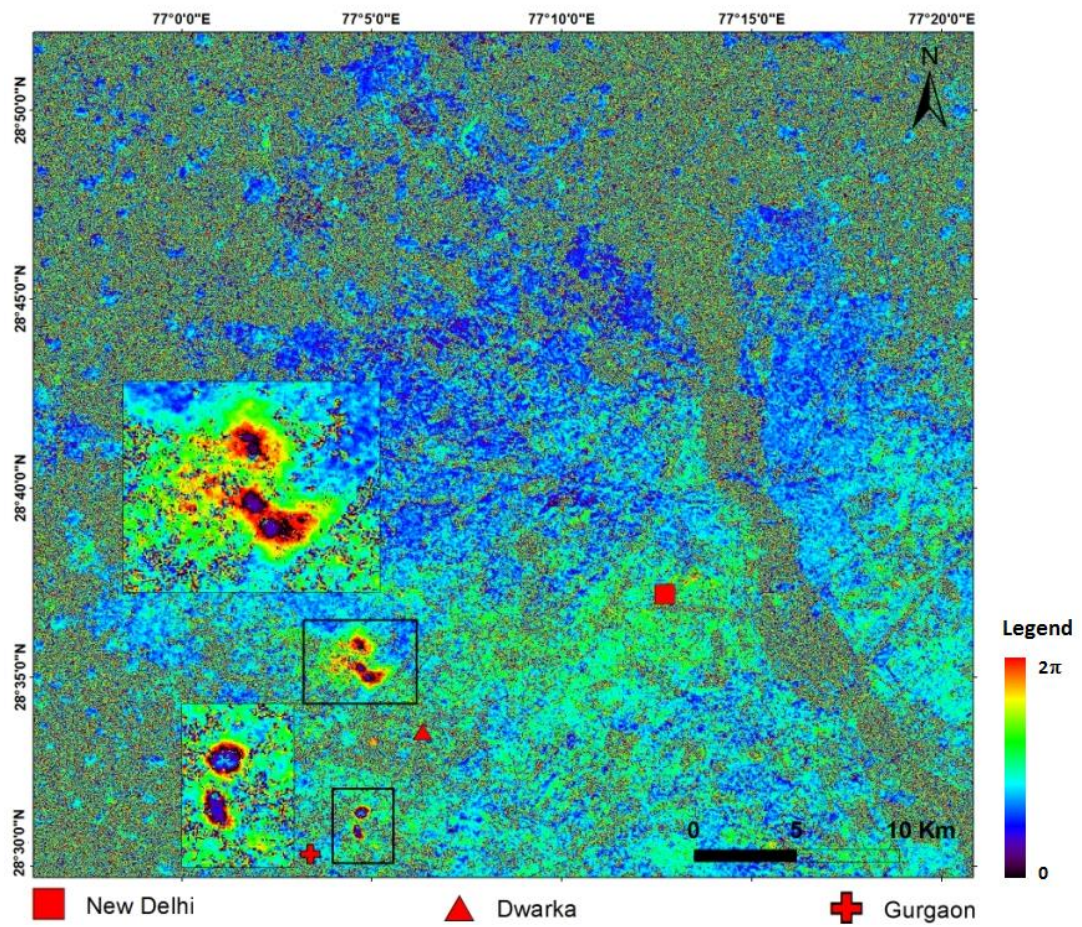


**Figure 5.21.** Interferogram showing land subsidence in Dwarka and Gurgaon area. Temporal baseline 414 days (2/12/2009 - 20-01-2011) and having average coherence of 0.22; coherence of 0.35 and 0.36 for fringe areas.

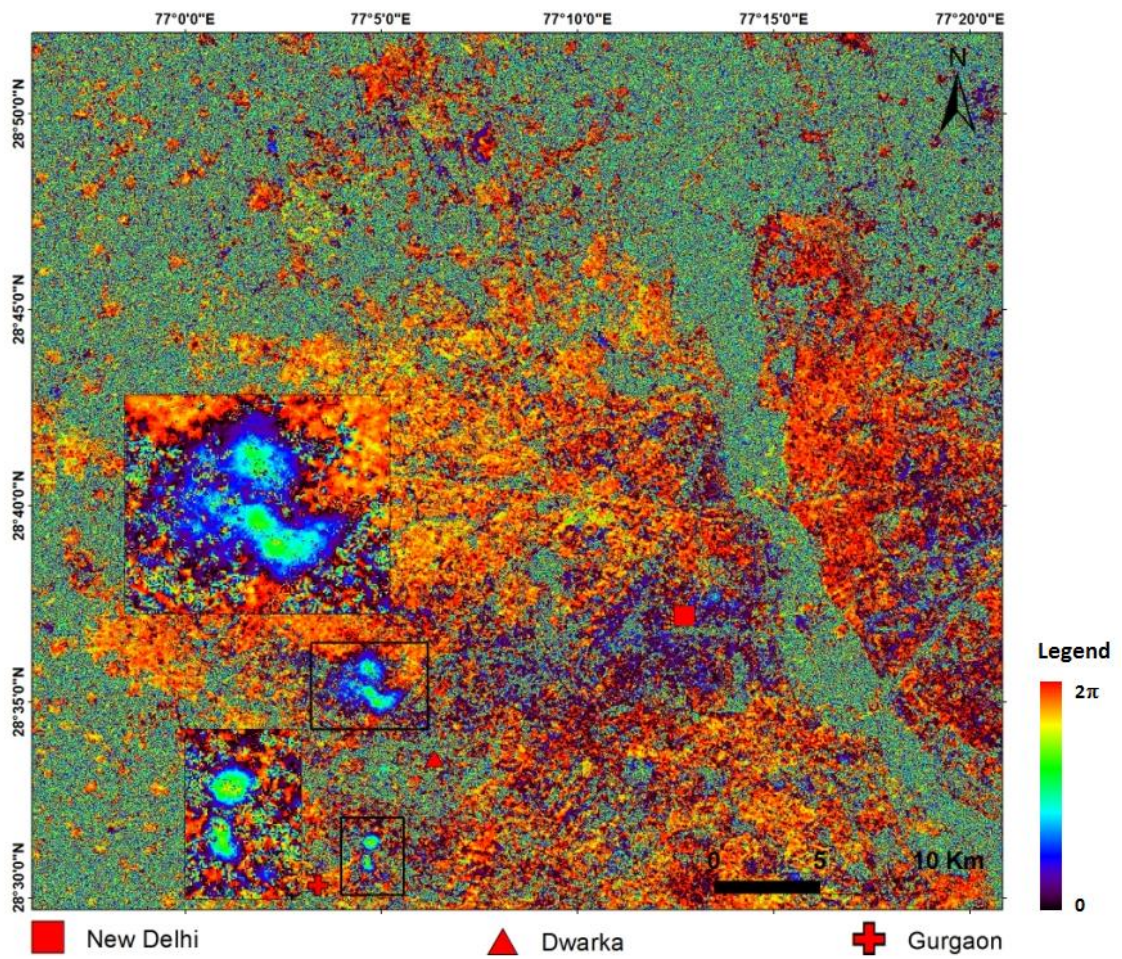


**Figure 5.22.** Interferogram showing land subsidence in Dwarka and Gurgaon area. Temporal baseline 368 days (17-01-2010 - 20-01-2011) and having average coherence of 0.66.

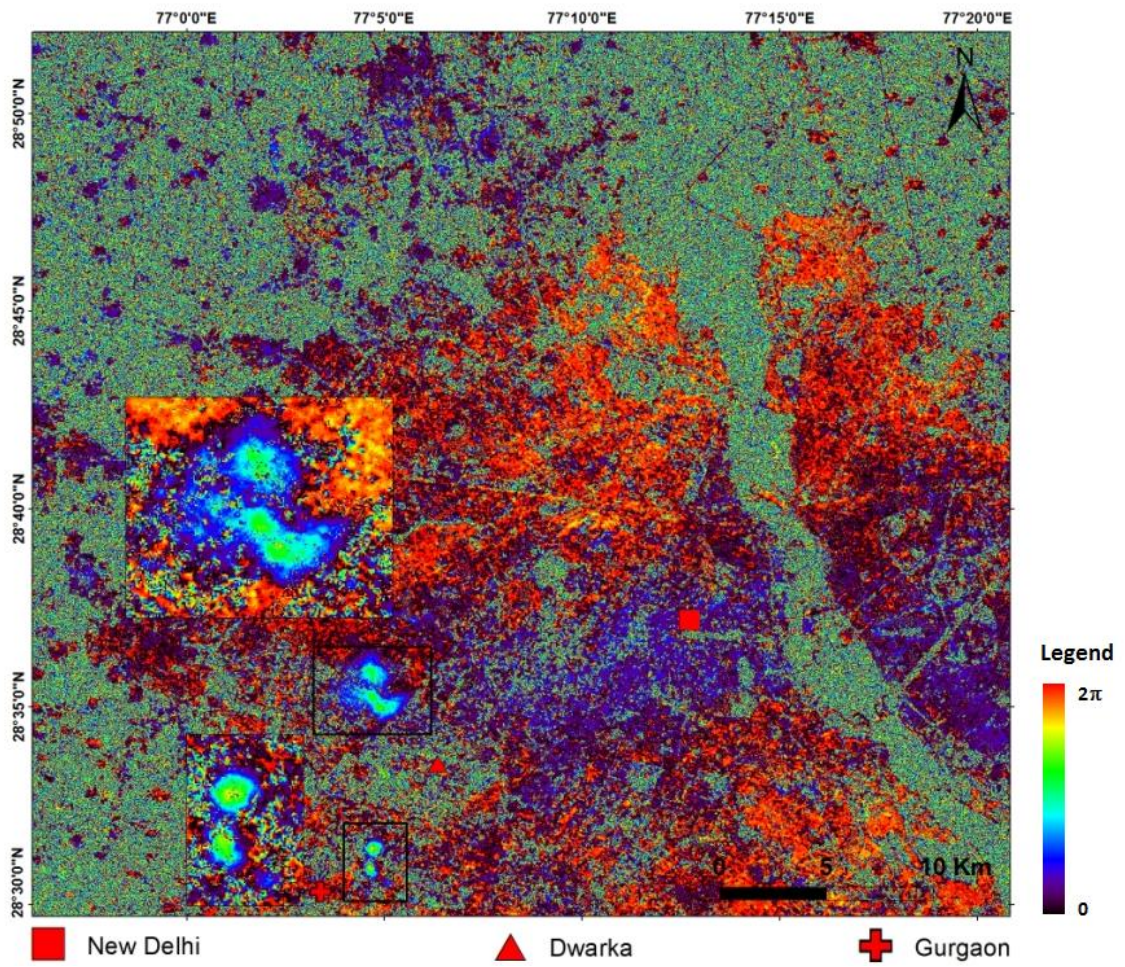


**Figure 5.23.** Interferogram showing land subsidence in Dwarka and Gurgaon area. Temporal baseline 322 days (4/3/2010 - 20-01-2011) and having average coherence of 0.23; coherence of 0.40 and 0.34 for fringe areas.

The interferograms obtained from C-band RASARSAT-2 data pairs are shown below. The temporal baseline varies from 48 days to 96 days.

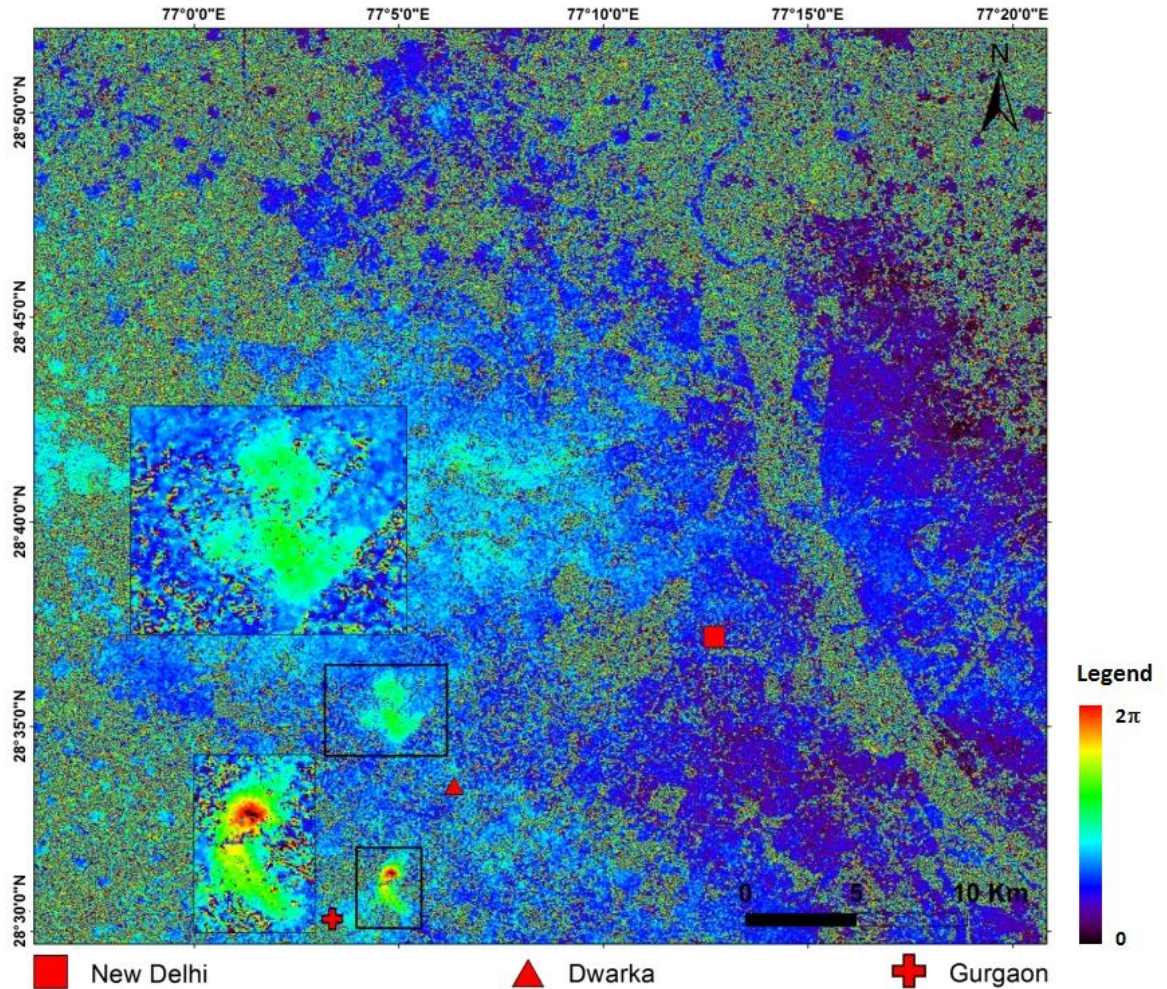


**Figure 5.24.** Interferogram showing land subsidence in Dwarka and Gurgaon area. Temporal baseline 48 days (03-12-2013 - 20-01-2014) and having average coherence of 0.26; coherence of 0.49 and 0.36 for fringe areas.

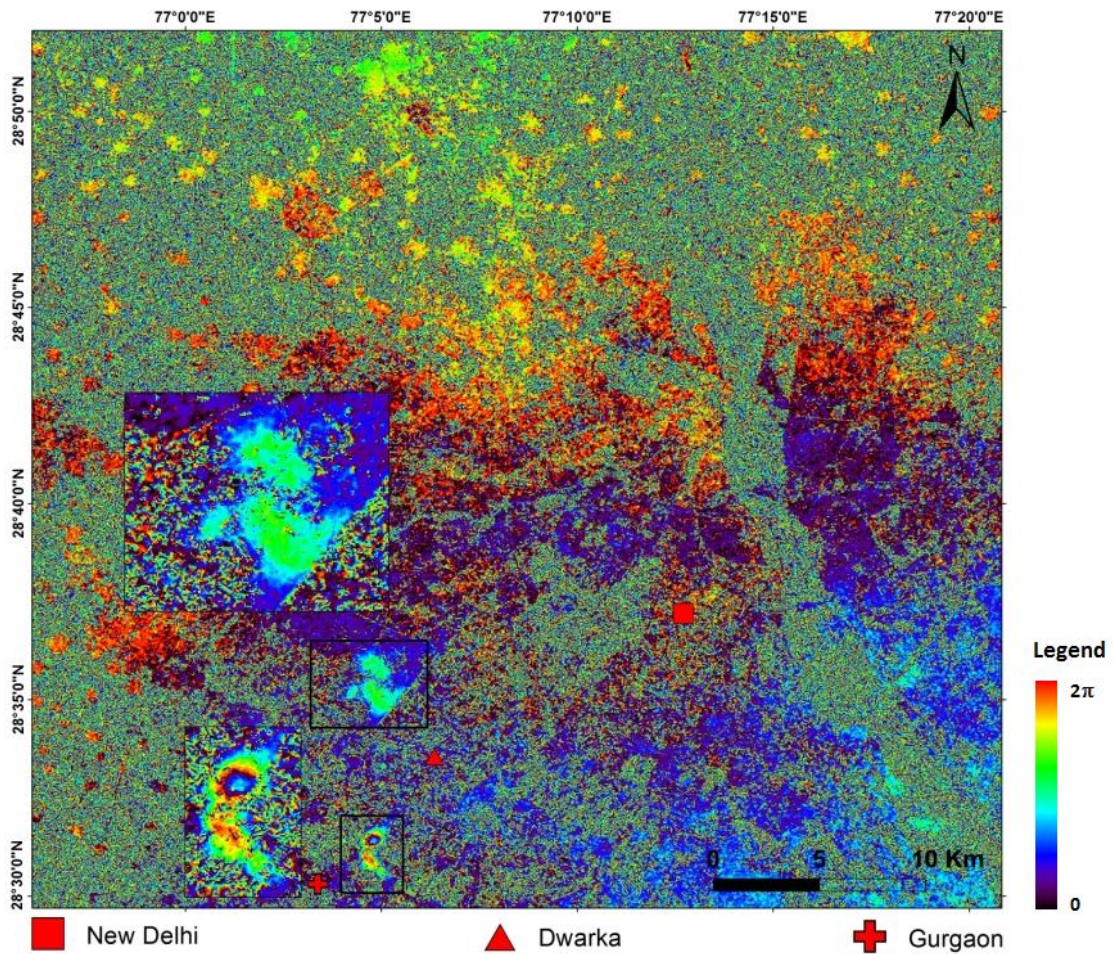


**Figure 5.25.** Interferogram showing land subsidence in Dwarka and Gurgaon area. Temporal baseline 96 days (03-12-2013 - 09-03-2014) and having average coherence of 0.25; coherence of 0.34 and 0.32 for fringe areas.

The subsidence rate in Delhi estimated as per the colour cycles (depicting a phase cycle) is listed below in table (5.2) for ALOS PALSAR data sets. F-1 and F-2 represents Dwarka area and F-3 and F-4 represents Gurgaon area.

**Table 5.2.** LOS Deformation rate for ALOS PALSAR data sets for Delhi from December, 2009 to January, 2011.

Fringe ID	Fringe Sub ID	Fringe centre co-ordinates (dd)	INSAR pair	Temporal baseline (days)	Colour sequence	Phase difference	LOS deformation (cm)	LOS deformation rate (cm/yr)
F1	F1a	77.078; 28.598	20548- 26587	414	C-G-Y-O- R-I-V	7	10.33	9.11
	F1b	77.078; 28.598	21219- 26587	368	R-I-V-B-C- G	6	8.86	8.79
	F1c	77.078; 28.598	21890- 26587	322	I-V-B-C-G	5	7.38	8.37
	F2a	77.081; 28.583	20548- 26587	414	C-G-Y-O- R-I-V-B	8	11.81	10.41

F2	F2b	77.081; 28.583	21219- 26587	368	R-I-V-B-C- G	6	8.86	8.79
	F2c	77.081; 28.583	21890- 26587	322	I-V-B-C-G	5	7.38	8.37
F3	F3a	77.079; 28.523	20548- 26587	414	C-G-Y-O- R-I-V-B	8	11.81	10.41
	F3b	77.079; 28.523	21219- 26587	368	I-V-B-C-G- Y	6	8.86	8.79
	F3c	77.079; 28.523	21890- 26587	322	I-V-B-C-G- Y	6	8.86	10.04
F4	F4a	77.077; 28.515	20548- 26587	414	C-G-Y-O- R-I-V-B	8	11.81	10.41
	F4b	77.077; 28.515	21219- 26587	368	I-V-B-C-G- Y	6	8.86	8.79
	F4c	77.077; 28.515	21890- 26587	322	I-V-B-C-G- Y	6	8.86	10.04

According to the above table, the LOS deformation rate varies from 8.37 to 10.41 cm/year. The maximum rate has been observed for the pairs having maximum temporal baseline (pair: 20548-26587).

The subsidence rate in Delhi estimated as per the colour cycles (depicting a phase cycle) is listed below in table (5.3) for RADARSAT-2 data sets. F-1 and F-2 represents Dwarka area and F-3 represents Gurgaon area.

**Table 5.3.** LOS Deformation rate for RADARSAT-2 data sets for Delhi December, 2013 to March, 2014.

Fringe ID	Fringe Sub ID	Fringe centre coordinates (dd)	INSAR pair	Temporal baseline (days)	Colour sequence	Phase difference	LOS deformation (cm)	LOS deformation rate (cm/year)
F1	F1a	77.078; 28.598	5326- 5323	48	B-C-G	3	0.98	7.50
	F1b	77.078; 28.598	5323- 5321	48	V-B	2	0.66	5.00
	F1c	77.078; 28.598	5326- 5321	96	V-B- C-G	3	0.99	3.75
F2	F2a	77.081; 28.583	5326- 5323	48	B-C-G	3	0.99	7.50
	F2b	77.081; 28.583	5323- 5321	48	V-B	2	0.66	5.00
	F2c	77.081; 28.583	5326- 5321	96	B-C-G	3	0.99	3.75
F3	F3a	77.08; 28.523	5326- 5323	48	B-C- G-Y	4	1.60	12.17
	F3b	77.08; 28.523	5323- 5321	48	V-B-C	3	1.20	7.50
	F3c	77.08; 28.523	5326- 5321	96	C-G- Y-O	4	1.60	11.24

According to the above table, the LOS deformation rate varies from 3.75 to 12.17 cm/year. Maximum subsidence has been observed in Gurgaon area.

#### **LOS Deformation Calculation from Phase difference:**

The LOS deformation calculated using the phase component by following the process of phase unwrapping lead to the following results. Results for ALOS PALSAR and RADARSAT-2 data sets for Delhi area, are tabulated in table (5.4) and (5.5) respectively. It includes the information on LOS deformation rate for fringe area as well as the background and the coherence weighted LOS deformation.

The time weighted and coherence weighted LOS displacement rates were calculated using the phase component.

The coherence weighted LOS displacement rates are provided in the tables itself. The time-weighted displacement rates are given below.

#### **Time weighted LOS displacement rate for ALOS PALSAR data sets:**

##### **Fringe 1 (Dwarka):**

Time weighted Displacement Rate (Max): 8.37 cm/year

Time weighted Displacement Rate (Avg): 3.95 cm/year

##### **Fringe 2 (Gurgaon):**

Time weighted Displacement Rate (Max): 8.37 cm/year

Time weighted Displacement Rate (Avg): 5.09 cm/year

#### **Time weighted LOS displacement rate for RADARSAT-2 data sets:**

##### **Fringe 1 (Dwarka):**

Time weighted Displacement Rate (Max): 9.25 cm/year

Time weighted Displacement Rate (Avg): 3.76 cm/year

##### **Fringe 2 (Gurgaon):**

Time weighted Displacement Rate (Max): 7.09 cm/year

Time weighted Displacement Rate (Avg): 3.44 cm/year

**Coherence weighted LOS displacement rate for ALOS PALSAR data sets:**

**Fringe 1 (Dwarka):**

Coherence weighted Displacement Rate (Max): 9.86 cm/year

Coherence weighted Displacement Rate (Avg): 3.91 cm/year

**Fringe 2 (Gurgaon):**

Coherence weighted Displacement Rate (Max): 8.61 cm/year

Coherence weighted Displacement Rate (Avg): 5.07 cm/year

**Coherence weighted LOS displacement rate for RADARSAT-2 data sets:**

**Fringe 1 (Dwarka):**

Coherence weighted Displacement Rate (Max): 10.30 cm/year

Coherence weighted Displacement Rate (Avg): 0.20 cm/year

**Fringe 2 (Gurgaon):**

Coherence weighted Displacement Rate (Max): 2.48 cm/year

Coherence weighted Displacement Rate (Avg): 7.70 cm/year

This is an alarming situation as the subsidence rate is on higher side and it is being continued from December, 2009 to March, 2014, as depicted in ALOS PALSAR as well as RADARSAT-2 datasets for different time frames over same area Viz., Dwarka and Udyog Vihar, Gurgaon.

**Table 5.4.** LOS Deformation rate using phase component for ALOS PALSAR data sets for Delhi from December, 2009 to January, 2011.

<b>Fringe ID</b>	<b>Fringe Sub ID</b>	<b>INSAR pair</b>	<b>Temporal baseline (days)</b>	<b>Coherence</b>	<b>Max. Phase (fringe)</b>	<b>Mean Phase (fringe)</b>	<b>Mean Phase (background)</b>	<b>Max - Mean (Fringe)</b>	<b>Mean (fringe) - Mean (background)</b>	<b>LOS Displacement (Max.)</b>	<b>LOS Displacement (Average)</b>	<b>LOS Displacement Rate (Max.)</b>	<b>LOS Displacement Rate (Average)</b>	<b>LOS Displacement Rate (Coherence Weighted) Max.</b>	<b>LOS Displacement Rate (Coherence Weighted) Avg.</b>
F1	F1a	20548-21890	92	0.45	3.48	2.58	2.21	0.90	0.37	1.70	0.69	6.75	4.64	8.02	4.46
	F1b	21219-26587	368	0.34	8.54	4.86	2.91	3.68	1.95	6.92	3.67	6.86	3.64	8.29	3.91
	F1c	21890-26587	322	0.35	2.81	-1.24	-3.01	4.05	1.78	7.62	3.34	8.64	3.79	9.21	3.98
	F1d	20548-26587	414	0.31	7.88	1.93	-0.61	5.95	2.54	11.19	4.78	9.87	4.21	9.87	4.21
F2	F2a	20548-21890	92	0.48	4.03	3.18	2.56	0.85	0.62	1.60	1.17	6.36	4.62	7.05	5.07
	F2b	21219-26587	368	0.33	4.27	-0.29	-2.78	4.57	2.49	8.59	4.68	8.52	4.65	8.35	5.19
	F2c	21890-26587	322	0.33	9.33	5.10	2.84	4.23	2.26	7.96	4.24	9.02	4.81	8.61	5.27
	F2d	20548-26587	414	0.3	19.62	14.70	11.20	4.92	3.50	9.26	6.58	8.16	5.80	8.16	5.79

**Table 5.5.** LOS Deformation rate using phase component for RADARSAT-2 data sets for Delhi from December, 2013 to March, 2014.

<b>Fringe ID</b>	<b>Fringe Sub ID</b>	<b>INS AR pair</b>	<b>Temporal baseline (days)</b>	<b>Coherence</b>	<b>Max Phase (fringe)</b>	<b>Mean Phase (fringe)</b>	<b>Mean Phase (background)</b>	<b>Max - Mean (Fringe)</b>	<b>Mean (fringe) - Mean (background)</b>	<b>LOS Displacement (Fringe)</b>	<b>LOS Displacement (background)</b>	<b>LOS Displacement Rate (Max.)</b>	<b>LOS Displacement Rate (Average)</b>	<b>LOS Displacement Rate (Coherence weighted) Max</b>	<b>LOS Displacement Rate (Coherence weighted) Avg</b>
F1	F1a	5326 - 5323	48	0.53	7.01	5.07	3.37	1.94	1.70	0.87	0.76	6.58	5.75	7.98	1.67
	F1b	5323 - 5321	48	0.38	1.87	-1.36	-2.62	3.23	1.25	1.44	0.56	10.94	4.25	10.31	0.20
	F1c	5326 - 5321	96	0.42	7.40	1.66	3.71	5.74	-2.05	2.56	-0.91	9.74	-3.48	9.74	-3.48
F2	F2a	5326 - 5323	48	0.47	3.68	1.64	0.21	2.04	1.43	0.91	0.64	6.92	4.83	7.28	3.76
	F2b	5326 - 5321	48	0.35	1.87	0.09	-1.09	1.78	1.17	0.79	0.52	6.03	3.98	6.91	3.18
	F2c	5326 - 5321	96	0.39	5.70	1.15	-0.31	4.55	1.46	2.03	0.65	7.71	2.48	7.71	2.48

## **6. CONCLUSION AND RECOMMENDATION**

### **6.1. CONCLUSIONS:**

#### **6.1.1. HOW FAR GROUNDWATER DEPLETION SCENARIO IS CORRELATED WITH SPACE-BORNE GRAVITY ANOMALIES?**

The decadal ground water storage change estimated from the GRACE terrestrial water storage data and GLDAS soil moisture for 2003-12 came out to be  $104.65 \pm 11.64 \text{ Km}^3$ . It was a very tedious and time consuming task to verify the results with ground data as the study region (NW India) is composed of various different types of aquifers and a large number of wells (including peizometric wells and dugwells). Therefore, I correlated the GRACE derived ground water storage fluctuation for Delhi pixel with the depth to water level fluctuation provided by Central Ground Water Board. The correlation was satisfactory and hence the results were validated.

The maximum depletion rate of  $2.29 \pm 0.72 \text{ cm/year}$  was observed in Haryana, whereas the maximum volumetric loss was observed in Uttara Pradesh where the depletion rate was observed as  $1.641 \pm 0.77 \text{ cm/year}$  but having larger surface area.

The minimum depletion rate was observed in the state of Rajasthan i.e.,  $1.11 \pm 0.42 \text{ cm/year}$ .

The TWSC (Terrestrial Water Storage Change) rate and ground water storage change rate shows maximum depletion along the eastern side of Uttar Pradesh (plate boundary) and northern UP, Delhi and parts of Punjab, Haryana and Rajasthan. This calls special attention on the characteristic volumetric water loss across the plate boundary,

#### **6.1.2. WHAT IS THE EXTENT OF IMPACT OF GROUNDWATER DEPLETION TO LAND SUBSIDENCE IN DELHI NCT?**

After processing the multi-temporal SAR data for L-band as well as C-band using Differential Interferometric SAR technique, two areas in Delhi showing characteristic fringes were observed. One was in highly developing Dwarka area and another one was in Udyog Vihar, Gurgaon. Both the areas showed a maximum subsidence rate of 7 to 9 cm/year over the time period of December, 2009 to January, 2011 and December, 2013 to March, 2014.

This is an alarming situation as the subsidence in both the areas is being continued from December, 2009 to March, 2014.

## **6.2. RECOMMENDATIONS:**

Combining the GRACE results with subsurface hydrogeological models may provide the information on ground water behavior over time with higher accuracy.

Framing of a model in which ground water fluctuation for large number of wells can be used to validate the GRACE derived ground water fluctuation for a large area.

More exhaustive field investigations of well sites in relation to location, topography and structures as well as subsurface information such as pumping test and lithological log data may be made to improve the understanding of the hydrogeological conditions in the area.

Continuous and extensive levelling surveys and GPS measurements to be carried out in the critical areas where land subsidence is reported.

Use of Boxcar filtering for the pairs with high coherence and Adaptive filtering for the pairs with lower coherence.

Due to the lack of lithologs for the subsidence affected areas for Delhi, the predictive modelling for aquifer layer compression could not be accomplished in time. But if it could have been included in the project, more accuracy would have been added to the results.

## REFERENCES:

- Abidin, Hasanuddin Z., H. Andreas, I. Gumilar, S. Wangsaatmaja, Y. Fukuda, and T. Deguchi. 2009. "Land Subsidence and Groundwater Extraction in Bandung Basin, Indonesia." *IAHS Publication* 20: 145.
- Amelung, F., Devin L. Galloway, John W. Bell, Howard A. Zebkar, and Randell J. Lacznik. 1999. "Sensing Ups and Downs of Las Vegas: InSAR Reveals Structural Control of Land Subsidence and Aquifer-System Deformation." *Geology* 27 (June): 483–86.
- Bell, John W., and J. G. Price. 1991. "Subsidence in Las Vegas Valley". Nevada Bureau of Mines.
- Berardino, P., G. Fornaro, R. Lanari, and E. Sansosti. 2002. "A New Algorithm for Surface Deformation Monitoring Based on Small Baseline Differential SAR Interferograms." *IEEE Transactions on Geoscience and Remote Sensing* 40 (11): 2375–83. doi:10.1109/TGRS.2002.803792.
- Biot, M. A. 1941. "General Theory of Three-Dimensional Consolidation." *Journal of Applied Physics* 12 (February): 155–64.
- Biot, M. A. 1955. "Theory of Elasticity and Consolidation for a Porous Anisotropic Solid." *Journal of Applied Physics* 26 (2): 182–85.
- Blodgett, James C, and J. S. Williams. 1992. *Land Subsidence and Problems Affecting Land Use at Edwards Air Force Base and Vicinity, California, 1990*. U.S. Geological Survey, 1992.
- Carroll, M. M. 1979. "An Effective Stress Law for Anisotropic Elastic Deformation." *Journal of Geophysical Research* 84 (13): 7510–12.
- Census. 2011. *Census 2011*. Ministry of Home Affairs, Government of India.
- CGWB. 2009. *Dynamic Ground Water Resources of India*. Central Ground Water Board, Ministry of Water Resources, Government of India.
- Aquifer Systems of India*. Central Ground Water Board, Ministry of Water Resources, 2012, Government of India.
- Ground Water Year Book 2012-13*. Central Ground Water Board, Ministry of Water Resources, Government of India.
- Ground Water Year Book, National Capital Territory, Delhi*. Central Ground Water Board, 2012-13, Ministry of Water Resources, Government of India.
- Chatterjee, R.S., Benedicte Fruneau, J.P. Rudant, P.S. Roy, Pierre-Louis Frison, R.C. Lakhera, V.K. Dadhwal, and Ranajit Saha. 2006. "Subsidence of Kolkata (Calcutta) City, India during the 1990s as Observed from Space by Differential Synthetic Aperture Radar Interferometry (D-InSAR) Technique." *Remote Sensing of Environment* 102 (1-2): 176–85. doi:10.1016/j.rse.2006.02.006.
- Chatterjee, Rana, B.K. Gupta, S.K. Mohiddin, P.N. Singh, Shashank Shekhar, and Rajaram Purohit. 2009. "Dynamic Groundwater Resources of National Capital Territory, Delhi: Assessment, Development and Management Options." *Environmental Earth Sciences* 59 (3): 669–86. doi:10.1007/s12665-009-0064-y.
- Chopra, S. 1990. "A Geological Cum Geomorphological Framework of Haryana and Adjoining Areas for Landuse Appraisal Using Landsat Imagery." *Journal of the Indian Society of Remote Sensing* 18 (1-2): 15–22. doi:10.1007/BF03017813.
- Costantini, M. 1998. "A Novel Phase Unwrapping Method Based on Network Programming." *IEEE Transactions on Geoscience and Remote Sensing* 36 (3): 813–21.
- Ding, X. L., G. X. Liu, Z. W. Li, Z. L. Li, and Y. Q. Chen. 2004. "Ground Subsidence Monitoring in Hong Kong with Satellite SAR Interferometry." *Photogrammetric Engineering and Remote Sensing* 70 (10): 1151–56.
- "Directorate of Geology & Mining, Uttar Pradesh." 2014. Accessed June 13. [http://mineral.up.nic.in/geological\\_map.htm](http://mineral.up.nic.in/geological_map.htm).

- Faunt, R.T. Hanson, K. Belitz, W Schmid, S.P. Predmore, D.L. Rewis, and K McPhearson. 2009. "Groundwater Availability of the Central Valley Aquifer, California." *US Geological Survey*, pp. 246.
- Ferretti, A., C. Prati, and F. Rocca. 2000. "Nonlinear Subsidence Rate Estimation Using Permanent Scatterers in Differential SAR Interferometry." *IEEE Transactions on Geoscience and Remote Sensing* 38 (5): 2202–12.
- Gabriel, A, R Goldstein, and H Zebkar. 1989. "Mapping Small Elevation Changes over Large Areas: Differential Radar Interferometry." *Journal of Geophysical Research* 94: 9183–91.
- Galloway, Devin L., K. W. Hudnut, S. E. Ingebritsen, S. P. Phillips, G. Peltzer, F. Rogez, and P. A. Rosen. 1998. "Detection of Aquifer System Compaction and Land Subsidence Using Interferometric Synthetic Aperture Radar, Antelope Valley, Mojave Desert, California." *Water Resources Research* 34 (10): 2573–85.
- Gehlot, Swati, and Ramon F. Hanssen. 2008. "Monitoring and Interpretation of Urban Land Subsidence Using Radar Interferometric Time Series and Multi-Source GIS Database." In *Remote Sensing and GIS Technologies for Monitoring and Prediction of Disasters*, 137–48. Springer. [http://link.springer.com/chapter/10.1007/978-3-540-79259-8\\_8](http://link.springer.com/chapter/10.1007/978-3-540-79259-8_8).
- "Giovanni - Global Land Data Assimilation System (GLDAS)." 2013. Accessed September 12. [http://gdata1.sci.gsfc.nasa.gov/daac-bin/G3/gui.cgi?instance\\_id=GLDAS10\\_M](http://gdata1.sci.gsfc.nasa.gov/daac-bin/G3/gui.cgi?instance_id=GLDAS10_M).
- "Grace - Earth Missions - NASA Jet Propulsion Laboratory - NASA Jet Propulsion Laboratory." 2013. Accessed October 4. <http://www.jpl.nasa.gov/missions/details.php?id=5882>.
- "GRACE - Gravity Recovery and Climate Experiment." 2013. Accessed September 6. [http://www.csr.utexas.edu/grace/gallery/gravity/03\\_07\\_GRACE.html](http://www.csr.utexas.edu/grace/gallery/gravity/03_07_GRACE.html).
- "GRACE Tellus: GRACE MONTHLY MASS GRIDS - LAND." 2013. Accessed September 11. <http://grace.jpl.nasa.gov/data/gracemonthlymassgridsland/>.
- "Ground Water Resources -." 2014. Accessed June 13. [http://india-wris.nrsc.gov.in/wrpinfo/index.php?title=Ground\\_water\\_resources](http://india-wris.nrsc.gov.in/wrpinfo/index.php?title=Ground_water_resources).
- Hanssen, Ramon F. 2001. *Radar Interferometry – Data Interpretation and Error Analysis*. Kluwer Academic Publishers.
- Helm, D. C. 1994. "Horizontal Aquifer Movement in a Theis-Thiem Confined System." *Water Resources Research* 30 (4): 953–64.
- Hernquist, L, and M. D. Weinberg. 1989. "Simulations of Satellite Orbital Decay." *Monthly Notices of the Royal Astronomical Society* 238: 407–16.
- Hoffmann, J. 2003. "The Application of Satellite Radar Interferometry to the Study of Land Subsidence over Developed Aquifer Systems". Stanford University.
- Holzer, ThomasL., and A.Ivan Johnson. 1985. "Land Subsidence Caused by Ground Water Withdrawal in Urban Areas." *GeoJournal* 11 (3). doi:10.1007/BF00186338.
- Ikehara, M. E., and S. P. Phillips. 1994. *Determination of Land Subsidence Related to Ground-Water-Level Declines Using Global Positioning System and Leveling Surveys in Antelope Valley, Los Angeles and Kern Counties, California, 1992*. 94-4184. Water-Resources Investigations Report. U.S. Geological Survey.
- IMD. 2013. *Monsoon Report*. Indian Meteorological Department, Ministry of Earth Sciences, Government of India.
- Jonsson, S. 2002. "Modeling Volcano and Earthquake Deformation from Satellite Radar Interferometric Observations". Stanford University.
- Jorgensen, D. G. 1980. *Relationships between Basic Soils - Engineering Equations and Basic Ground-Water Flow Equations*. U.S. Geological Survey.
- Kaya, Ş., P. J. Curran, and G. Llewellyn. 2005. "Post-earthquake Building Collapse: A Comparison of Government Statistics and Estimates Derived from SPOT HRVIR Data." *International Journal of Remote Sensing* 26 (13): 2731–40. doi:10.1080/01431160500099428.

- Landerer, F. W., and S. C. Swenson. 2012. "Accuracy of Scaled GRACE Terrestrial Water Storage Estimates." *Water Resources Research* 48 (4).
- Massonnet, D, M Rossi, and C Carmona. 1993. "The Displacement Field of the Landers Earthquake Mapped by Interferometry." *Nature*, 138–42.
- NRSA. 2008. *Ground Water Prospects Mapping for Rajiv Gandhi National Drinking Water, Manual*.
- Nur, A., and J.D. Byerlee. 1971. "An Exact Effective Stress Law for Elastic Deformation of Rock with Fluids." *Journal of Geophysical Research* 76(26) (September): 6414–19.
- Poland, J. F., B. E. Lofgren, and R. L. Ireland. 1975. *Land Subsidence in the San Joaquin Valley, California, as of 1972*. U.S. Geological Survey.
- "Rajasthan - Geology." 2013. Accessed September 10. <http://waterresources.rajasthan.gov.in/1geology.htm>.
- Ramillien, G, James S. Famiglietti, and J Wahr. 2008. "Detection of Continental Hydrology and Glaciology Signals from Grace: A Review." *Surv Geophys* 29: 361–74.
- Rao, A. D., P Saxena, R Purohit, M Kanwar, and S.K. Naik. 2011. *Ground Water Scenario in Major Cities of India*. Central Ground Water Board, Ministry of Water Resources, Government of India.
- Riley, F. S. 1969. "Analysis of Borehole Extensometer Data from Central California in Land Subsidence." *International Association of Scientific Hydrology* 89 (September): 423–31.
- Rodell, Matthew, Isabella Velicogna, and James S. Famiglietti. 2009. "Satellite-Based Estimates of Groundwater Depletion in India." *Nature* 460 (7258): 999–1002. doi:10.1038/nature08238.
- Schmidt, R, F Flechtner, U Meyer, KH Neumayer, Ch Dahle, R Konig, and J Kusche. 2008. "Hydrological Signals Observed by the Grace Satellites." *Surveys in Geophysics* 29(4-5): 319–34.
- Schmidt, R, F Fletchner, U Meyer, K.H. Neumayer, C Dahle, R Konig, and J Kusche. 2008. "Hydrological Signals Observed by the Grace Satellites." *Surv Geophys* 29: 319–34.
- Schmidt, R, P Schwintzer, F Fletchner, C Reigber, A Guntner, P Doll, G Ramillien, et al. 2006. "Grace Observations of Changes in Continental Water Storage." *Global and Planetary Change* 50: 112–26.
- Shekhar, Shashank, Raja Ram Purohit, and Y. B. Kaushik. 2009. "Groundwater Management in NCT Delhi." In *Technical Paper Included in the Special Session on Groundwater in the 5th Asian Regional Conference of INCID*. <http://www.indiaenvironmentportal.org.in/files/Kaushik.pdf>.
- Sun, H., D. Grandstaff, and R. Shagam. 1999. "Land Subsidence due to Groundwater Withdrawal: Potential Damage of Subsidence and Sea Level Rise in Southern New Jersey, USA." *Environmental Geology* 37 (4): 290–96.
- Syed, T.H., James S. Famiglietti, Matthew Rodell, J Chen, and C.R. Wilson. 2008. "Analysis of Terrestrial Water Storage Changes from Grace and Gldas." *Water Resources Research* 44.
- Tapley, B.D., S Bettapur, J.C. Ries, P.F. Thomson, and M Watkins. 2004. "Grace Measurements of Mass Variability in the Earth System." *Science* 305: 503–5.
- Tiwari, V. M., J. Wahr, and S. Swenson. 2009. "Dwindling Groundwater Resources in Northern India, from Satellite Gravity Observations." *Geophysical Research Letters* 36 (18). doi:10.1029/2009GL039401.
- Todd, D. K. 1980. *Groundwater Hydrology*. 2nd ed. New York: John Wiley & Sons.
- Tomás, Roberto, Yolanda Márquez, Juan M. Lopez-Sanchez, José Delgado, Pablo Blanco, Jordi J. Mallorquí, Mónica Martínez, Gerardo Herrera, and Joaquín Mulas. 2005. "Mapping Ground Subsidence Induced by Aquifer Overexploitation Using Advanced Differential SAR Interferometry: Vega Media of the Segura River (SE Spain) Case Study." *Remote Sensing of Environment* 98 (2-3): 269–83. doi:10.1016/j.rse.2005.08.003.

- Wiese, D. N., WM Folkner, and RS Nerem. 2009. "Alternative Mission Architectures for a Gravity Recovery Satellite Mission." *Journal of Geodesy* 83(6): 569–81.
- Wolff, M. 1969. "Direct Measurements of the Earth's Gravitational Potential Using a Satellite Pair." *Journal of Geophysical Research* 74: 5295–5300.
- Zebker, Howard A., Charles L Werner, P. A. Rosen, and H. Scott. 1994. "Accuracy of Topographic Maps Derived from ERS-1 Interferometric Radar." *IEEE Transactions on Geoscience and Remote Sensing* 32 (5): 823–36.